Titre: Title:	Fatigue Behavior of Welded Joints with Partial Penetration
Auteur: Author:	Reza Ghafoori Ahangar
Date:	2018
Type:	Mémoire ou thèse / Dissertation or Thesis
Référence: Citation:	Ghafoori Ahangar, R. (2018). Fatigue Behavior of Welded Joints with Partial Penetration [Thèse de doctorat, École Polytechnique de Montréal]. PolyPublie. https://publications.polymtl.ca/3759/

URL de PolyPublie: PolyPublie URL:	https://publications.polymtl.ca/3759/
Directeurs de recherche: Advisors:	Ricardo Camarero, Sylvain Turenne, & François Guibault
Programme: Program:	Génie Mécanique

UNIVERSITÉ DE MONTRÉAL

FATIGUE BEHAVIOR OF WELDED JOINTS WITH PARTIAL PENETRATION

REZA GHAFOORI AHANGAR

DÉPARTEMENT DE GÉNIE MÉCANIQUE

ÉCOLE POLYTECHNIQUE DE MONTRÉAL

THÈSE PRÉSENTÉE EN VUE DE L'OBTENTION

DU DIPLÔME DE PHILOSOPHIAE DOCTOR

(GÉNIE MÉCANIQUE)

DÉCEMBRE 2018

UNIVERSITÉ DE MONTRÉAL

ÉCOLE POLYTECHNIQUE DE MONTRÉAL

Cette thèse intitulée :

FATIGUE BEHAVIOR OF WELDED JOINTS WITH PARTIAL PENETRATION

présentée par : GHAFOORI AHANGAR Reza

en vue de l'obtention du diplôme de : Philosophiae Doctor

a été dûment acceptée par le jury d'examen constitué de :

M. LÉVESQUE Martin, Ph. D., président

M. CAMARERO Ricardo, Ph. D., membre et directeur de recherche

M. TURENNE Sylvain, Ph. D., membre et codirecteur de recherche

M. GUIBAULT François, Ph. D., membre et codirecteur de recherche

M. BALAZINSKI Marek, Docteur ès sciences, membre

M. LANTEIGNE Jacques, Ph. D., membre externe

DEDICATION

To my dearest parents, brother, and sister; for your support, encouragement, patience, and love!

ACKNOWLEDGMENTS

This research, performed within the Consortium de Recherche en Fabrication et Réparation des Roues d'Eau (CReFaRRE) and the Mathematics of Information Technology and Complex Systems (MITACS), was supported by the Natural Sciences and Engineering Research Council of Canada (NSERC), the General Electric (GE) Renewable Energy, and the Institut de Recherche en Électricité du Québec (IREQ, Hydro-Québec).

The technical help by Michel Sabourin, Éric Moisan, Alexandre Trudel, Benoît Papillon, Louis Mathieu, Étienne Dallaire, Josée Laviolette, Martin Cardonne, and Isabelle Nowlan is gratefully acknowledged.

I would like to express my profound gratitude to Professor Yves Verreman for his endless patience, invaluable guidance, technical support, and helpful discussions during the course of this research. He taught me how to conduct the research and he guided me to pursue and develop the ideas of this research. It is my pleasure to work in his research group and I am so grateful for his great technical insights.

In addition, I would like to express my sincere appreciation and profound gratitude to my supervisor and co-supervisors, Professors Ricardo Camarero, Sylvain Turenne, and François Guibault, for their invaluable trust, constant encouragement, and wise straightforward advice and comments that helped me to find my way and complete this research successfully.

I greatly acknowledge Professors Martin Lévesque, Marek Balazinski, and Jacques Lanteigne for their acceptance to participate in the jury and for the time devoted to evaluate my thesis.

I owe special gratitude to my office-mates at A-454, colleagues, and friends. I appreciate their company and the time we spent together. In particular, I would like to thank Mehdi, Cécile, Simon, and Michael.

Finally, last but not least, this undertaking would never have been completed without the patience, support, encouragement, and suggestions of my dear friend Hassan Rezaee and my dear family. Thank you so much!

RÉSUMÉ

L'objectif de ce travail est d'aborder les aspects les moins connus des joints soudés à pénétration partielle (PPJ) dans le domaine de la fatigue oligocyclique et mégacyclique en flexion à amplitude constante. Les joints soudés reliant les aubes à la couronne de la roue de turbine Francis (ou du moyeu de la roue d'hélice) peuvent être assimilés à des soudures d'angles structurelles cruciformes en admettant certaines conditions. Dans le cadre de ce projet, ils ont été réalisés suivant les capacités du banc d'essai de fatigue et du montage en flexion. Leur géométrie a été choisie dans l'optique de la caractérisation de la vie en fatigue de la racine et du bord de la soudure. L'influence de la profondeur de pénétration de la soudure, ainsi que l'influence du métal d'apport ont également été étudiées. Afin de répondre aux besoins du projet, quatre types d'essais ont été conçus. Les matériaux utilisés sont l'acier inoxydable martensitique AISI 415 en tant que métal de base, et les aciers martensitiques E410NiMo et austénitiques E316L comme métaux d'apport. Des précautions ont été prises pour la réalisation de la soudure PPJ. En effet, il était important qu'elle soit réalisée dans des conditions réelles, telle que réalisée sur les roues des turbines. Des résultats expérimentaux uniques d'essais de flexion trois points ont été obtenus pour la géométrie choisie (soudures d'angles avec cordons concaves). Ils ont montré que l'aspect de surface de la soudure avait un effet favorable sur l'amorce de la fissure et donc sur sa vie en fatigue. Aussi, le vide résultant à l'issue du soudage par manque de pénétration à la racine de la fissure est suffisamment important pour être considéré comme une fissure.

Jusqu'à présent, ce genre de géométrie sollicitée en flexion trois points ne présente pas de solution pout le facteur d'intensité de contraintes. Par conséquent, des méthodes de calculs numériques ont été employées pour le déterminer à la racine de la soudure. La validation des résultats a été réalisée par une étude numérique. Cette étude porte sur les paramètres influençant la précision du mode I des valeurs du facteur d'intensité de contraintes pour une fissure centrale à travers l'épaisseur de la pièce. Les paramètres ont été optimisés par la méthode d'extrapolation du déplacement afin de minimiser les erreurs. La méthode d'interaction intégrale basée sur les énergies a également été utilisée, et a permis d'obtenir des erreurs négligeables pour un intervalle de longueurs de fissures. L'évaluation du facteur d'intensité de contraintes des modes I et II s'est faite en fonction des recommandations faites pour le mode I dans les mêmes conditions. Les résultats obtenus ont montré que la précision du facteur d'intensité de contraintes en mode I calculée par la méthode d'extrapolation du déplacement est indépendante de la longueur de la fissure, alors que celle du

mode II y est fortement influencée. La méthode d'interaction intégrale apporte des valeurs cohérentes du facteur d'intensité de contraintes pour les deux modes, indépendamment de la longueur de la fissure. Les valeurs les plus précises sont obtenues avec l'approche des intégrales basées sur l'énergie, et calculées pour une longueur de fissure initiale ainsi que pour deux cas de propagation de fissure : symétrique et dissymétrique à la racine du joint soudé cruciforme. Aussi, la méthode numérique a été utilisée pour calculer la contrainte de traction non singulière à ce même endroit, ainsi que le facteur de concentration de contrainte au bord de la soudure.

L'approche de contrainte nominale est utilisée pour étudier la transition du mode de rupture en fatigue entre le bord et la racine de la soudure, tandis que l'approche par facteur d'intensité de contrainte de l'entaille est quant à elle utilisée pour consolider la résistance en fatigue de la racine de la soudure à différentes profondeurs de pénétration. Les résultats démontrent que l'origine de la rupture en fatigue ne peut pas être uniquement caractérisée par le paramètre géométrique parce que celle-ci change avec l'intensité de la contrainte de flexion nominale. La dispersion des résultats de rupture en fatigue débutant à la racine de la soudure est significative sur la courbe *S–N* obtenue. Cependant, cette dispersion est réduite significativement lors de l'introduction d'un facteur d'intensité de contrainte approprié dans l'approche par facteur d'intensité de contrainte de l'entaille. De plus, les résultats obtenus à partir des approches testées montrent que l'utilisation de l'acier martensitique E410NiMo pour la soudure mène à une résistance en fatigue supérieure à celle de l'acier austénitique E316L.

L'essai de fissuration en fatigue est traditionnellement réalisé sur des éprouvettes de tension compactes (TC) standardisées. La particularité de ces éprouvettes, est de contraindre le fond de fissure de manière extrême, et ce, en déformations planes. En pratique, la géométrie d'éprouvette utilisée (soudure d'angle structurelle cruciforme) dans le cadre de cette étude, ne permet pas d'obtenir un niveau de contrainte similaire en racine de soudure. Le comportement de la croissance de la fissure en fatigue pour les essais de flexion trois points a été étudié suivant deux profondeurs de pénétration de soudure. La propagation de la fissure en fatigue à la racine de la soudure a été observée sur le front de fissure en utilisant la technique de marquage des lignes d'arrêt puis, sur la surface latérale grâce à des microscopes mobiles. Un demi temps de vie en fatigue est nécessaire pour obtenir une longueur de propagation de la fissure de 2 mm environ. Le comportement de croissance de la fissure en fatigue des joints cruciformes est comparé aux éprouvettes de tension compact pour des ratios de charge compris entre 0.1 et 0.7. La vitesse de croissance des fissures en

fatigue à faible facteur d'intensité de contrainte $(R = 0.1)$ est plus faible que celle des éprouvettes TC, à cause de la différence de l'état de contrainte induite par la contrainte T (T-stress) négative, la contrainte résiduelle en compression après soudage à la racine du joint soudé cruciforme ainsi que l'intensité de fermeture de la fissure. L'approche de propagation de fissure est employée pour prédire la vie en fatigue de ce dernier. Lorsque le comportement de la croissance de fissure en fatigue des éprouvettes TC est considéré, le nombre de cycles de facteur d'intensité de contraintes est très proche de celui obtenu expérimentalement. L'utilisation de la courbe de croissance de fissure en fatigue quant à elle, permet une approche conservatrice de la prédiction de la vie en fatigue d'une turbine hydraulique.

ABSTRACT

The goal of the present work is to address some of the less understood aspects of the partial joint penetration (PJP) weld in the area of low cycle and high cycle bending fatigue of turbine runner steel subjected to constant amplitude loading. Welded joints of thick blades and the band/crown in the Francis turbine runners (or the hub in the propeller runners) can be deemed representative of the joints of load-carrying cruciform fillet welds with certain simplified considerations. The design of the cruciform joint studied in this thesis was performed considering the capacities of the available fatigue testing machine and flexure fixture. The geometry was selected such that the test results would allow the characterization of the weld toe and root fatigue lives; this feature therefore makes it an ideal specimen for studying the influence of weld penetration depth as well as the weld metal on fatigue behavior. To this aim, four different test types were devised. A wrought martensitic stainless steel AISI 415 was used as base metal, and as weld metals, martensitic E410NiMo and austenitic E316L stainless steels were employed. The particular PJP weld was fabricated under realistic conditions as used for turbine runners. Unique experimental fatigue data in three-point bending tests were produced for load-carrying cruciform fillet welded joints with concave fillet weld (round weld toes). The crack initiation life showed that the weld toe surface finish has a favorable effect on the fatigue strength, and the gap-tip at the weld root is significant enough to be considered as a crack-like defect.

Until now, for complex crack geometry of load-carrying cruciform joint with concave fillet weld under three-point bending load, the stress intensity factor (SIF) solution has not been established. Therefore, numerical methods are used to calculate the SIF at the weld root crack tip. To validate the results, a numerical study of the parameters influencing the accuracy of the computed mode I SIF values is presented for a through-thickness center crack. Optimized influencing parameters can minimize the errors obtained with the displacement extrapolation method (DEM), whereas the errors obtained with the energy-based interaction integral method (IIM) are negligible for a variety of crack lengths. Based on the recommendations made for the mode I SIF calculation, assessment of the mode I and mode II SIFs is performed at the weld root crack tip of a load-carrying cruciform fillet welded joint loaded under a three-point bending condition. The accuracy of the mode I SIF calculated with DEM is independent of the crack length, whereas that of mode II is highly dependent. The IIM provides accurate SIFs for both modes for various crack lengths. The accurate SIFs obtained with the energy-based integral approach are then calculated for initial crack length,

and for two cases of symmetrical and dissymmetrical crack propagations at the weld root crack tip in the studied cruciform joint. Moreover, the numerical method is employed to calculate the non-singular *T*-stress at the weld root crack tip and the stress concentration factor at the weld toe notch.

The nominal stress approach is used to investigate the fatigue failure mode transition between weld toe and weld root, while the notch stress intensity factor (N-SIF) approach is employed to consolidate the weld root fatigue strength of different weld penetration depths. The results demonstrate that the origin of fatigue failure cannot be characterized merely by geometric parameter, because it changes with the magnitude of the nominal bending stress range. The pronounced large scatter band of the fatigue failures at the weld roots in the *S*–*N* curve is meaningfully reduced by introducing an appropriate stress intensity factor in the N-SIF approach. In addition, the results acquired from the tested approaches show that using martensitic weld metal E410NiMo yields higher fatigue strength in comparison to austenitic weld metal E316L.

Fatigue cracking tests are traditionally carried out on a standard geometry of compact tension (CT) test specimens. CT specimens are highly constrained crack tips; however, in practice the weld root crack tip constraint of load-carrying cruciform fillet welded joints is not similar. Weld root fatigue crack growth (FCG) behavior in three-point bending is analyzed with two different weld penetration depths. Fatigue crack propagating at the weld root was visualized at the crack front by using the so-called beach marking technique, and it was monitored at lateral surface by using travelling microscopes. Half fatigue life is spent to have roughly 2 mm of weld root crack propagation length. FCG behavior of cruciform joints is compared with standard CT specimens at load ratios of 0.1 and 0.7. Fatigue crack growth rates at low stress intensity factor range of $R = 0.1$ are lower than CT specimen due to the difference in the fatigue stress state induced by the negative *T*-stress and the compressive welding residual stress at the weld root, and the crack closure intensity. The crack propagation approach is employed to predict fatigue life at the weld root of the cruciform joints. By considering the FCG behavior of CT specimen, the predicted number of cycles at high SIF range is very close to that obtained experimentally, while the use of the design curve reference of FCG behavior provides a conservative approach for predicting fatigue life in a turbine runner.

TABLE OF CONTENTS

LIST OF TABLES

LIST OF FIGURES

LIST OF SYMBOLS AND ABBREVIATIONS

Latin symbols

a	Crack length; crack depth
a_f	Final leading crack length
a_i	Initial crack length
a_l, a_s	Leading and secondary cracks
a_n, a_{n+1}	Start and end leading crack lengths
A	Material parameter related to σ_f; area inside the contour
b	Fatigue strength exponent; half specimen width
B	Stress biaxiality ratio
c	Crack width
C, m	Material constants of fatigue crack propagation
$\mathrm{d}a/\mathrm{d}N$	Fatigue crack growth rate (FCGR)
e_K	Percent difference
E	Elastic modulus
E'	Effective elastic modulus
F	(Three-point) bending load
G	Shear modulus
h	Weld leg length; half specimen height
I	Interaction integral
J	J-integral
k	Negative inverse slope
K	Stress intensity factor (SIF)
K_1, K_2, K_3	Loading modes for pointed V-notch
$K_{1\rho}$, $K_{2\rho}$, $K_{3\rho}$	Loading modes for rounded notch
K_C	Critical stress intensity factor
K_{eq}	Equivalent stress intensity factor
K_f	Fatigue notch factor

K_I, K_{II}, K_{III}	Mode I, mode II, and mode III stress intensity factors
$K_{\max}, K_{\min}$	Maximum and minimum stress intensity factors
K_{op}	Crack opening stress intensity factor
K_{res}	Stress intensity factor due to residual stress
K_t	Stress concentration factor (SCF)
L	Element size
L_B	Element size in the body
L_l	Loading location on the attachment plate
L_T	Element size around the crack tip
L_B / L_T	Mesh size ratio
n	Angular discretization around the crack tip; block of beach mark
N	Number of cycles
N / N_f	Fatigue life ratio
N_i	Crack initiation life
N_i / N_f	Fatigue life ratio of crack initiation
N_f	Number of cycles to failure
N_p	Crack propagation life
N_P	Predicted number of cycles
$O(r^{1/2}),\ T$	Non-singular stress terms
p	Weld penetration depth
q	Weight function in the domain integral
r	Weld toe radius
R	Load ratio
R_a	Roughness average
t	Plate thickness
t_{th}	Theoretical throat
U	Crack closure ratio

w	Width of the cruciform joint
W	Width of the CT specimen; strain energy density
Y	Geometry factor
$z_{\max}$	Maximum specimen deflection
(r, θ)	Polar coordinates with the origin at the crack tip
(u, v)	Displacements parallel and perpendicular to the crack growth direction
(x, y)	Cartesian coordinates with the origin at the crack tip

Greek symbols

2α	Notch opening angle
α	Crack length dimensionless parameter
Δ	Range
ΔK_{eff}	Effective stress intensity factor range
ΔK_{th}	Threshold stress intensity factor range
ε_{xx}, u_x	Strain and displacement parallel to the crack face
κ	Elastic parameter
ν	Poisson's ratio
ρ	Notch acuity
σ	Stress
σ_a	Stress amplitude
σ_f	Fatigue strength coefficient
$\sigma_{\max}, \sigma_{\min}$	Maximum and minimum (nominal bending) stresses
σ_n	Nominal (bending) stress
σ_{notch}	Fatigue strength of notch member
σ_{smooth}	Fatigue strength of smooth member
σ_y	Yield strength

Abbreviations

AWS	American Welding Society

CJP	Complete joint penetration
CT	Compact tension
DEM	Displacement extrapolation method
FCAW	Flux-cored arc welding
FCG	Fatigue crack growth
FCGR	Fatigue crack growth rate
FEM	Finite element method
HAZ	Heat-affected zone
HCF	High cycle fatigue
HSE	Health, safety, and environment
IIM	Interaction integral method
IIW	International Institute of Welding
LCF	Low cycle fatigue
LEFM	Linear elastic fracture mechanics
N-SIF	Notch stress intensity factor
PJP	Partial joint penetration
PWHT	Post-weld heat treatment
SCF	Stress concentration factor
SIF	Stress intensity factor

LIST OF APPENDICES

CHAPTER 1 INTRODUCTION

1.1 Background and description

Welding joints of a turbine runner structure e.g., between thick blades and the band/crown in a Francis turbine runner or the hub in a propeller runner (Figure 1.1), are often performed with a partial joint penetration (PJP) weld. This technique requires less blade edge preparation and also lower welding process time compared to a complete joint penetration (CJP) weld. The unwelded section resembles a crack-like defect, which is tolerable as long as no high cyclic loads are acting at the unwelded plane, as these could create fatigue cracks initiating and propagating from the sharp tip of the root gap. A schematic view of the PJP weld and the macrograph of the weldment analogous to a turbine runner joint are shown in Figure 1.2. The best-known benefits of PJP are mostly HSE (health, safety, and environment), dimensional, and economical considerations.

(a) (b)

Figure 1.1: Different hydro-turbine runners at the manufacturing facility of General Electric (GE): (a) a Francis runner composed of blades extending between the crown and band and (b) a propeller runner fabricated from welding blades to a hub

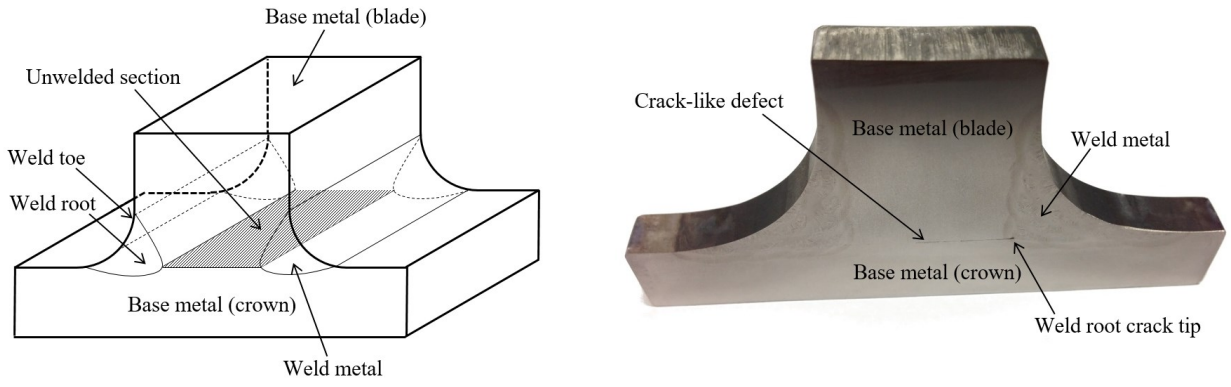

(a) (b)

Figure 1.2: Partially penetrated welded joint analogous to the joints of thick blades and band/crown in a Francis turbine runner or hub in a propeller runner: (a) schematic view of the PJP weld and (b) macrograph of weldment for the PJP

Regarding HSE, welders are at higher risk of exposure to hazardous fumes during CJP welding. When a welder strikes an arc, the arc heat vaporizes quantities of metal and releases solid particles, welding fumes, and subsequent gases into the working environment, which can adversely affect the health of those in the immediate area. Prolonged exposure to welding fumes in the workplace is a serious occupational risk for health. Furthermore, welding is carried out at a preheat temperature of 100 °C which is physically demanding for welders. It is worth mentioning that CJP welding requires back gouging which is another source of risk for welders. The dimensional aspect of the PJP weld relates to distortion and warpage of the turbine runner blades. Precise blade geometry is necessary to get maximum turbine efficiency. The PJP is used to minimize the runner deformation during welding and post-weld heat treatment (PWHT) [1]. Thermal expansion can have a profound effect on the blade geometry and inclination angle. Finally yet importantly, the number of weld passes and the time required to partially weld a joint are less than those needed to achieve a CJP, leading to lower processing costs. The joint preparation needed to achieve a CJP is time consuming as it consists of chamfering the blade edges and gouging the slags which are the solidified remaining flux (solid shielding material used in the welding process) following cooling of the weld area.

The major shortcoming of PJP weld is the existence of an unwelded section (Figure 1.2a) that acts as an initial embedded crack (crack-like defect). The micrographs of the weld roots at the end of penetrations are shown in Figure 1.3. The large plate gap between two base metals in Figure 1.3b is due to the fit up of the plates. Both figures indicate a sharp crack immediately adjacent to the weld metal. From these crack-like defects, fatigue cracks can propagate during the first loading cycles (no nucleation stage) [2, 3]. Owing to the decreasing weld joint penetration depth, there is a strong possibility of root failure before toe failure and thus loss of fatigue strength.

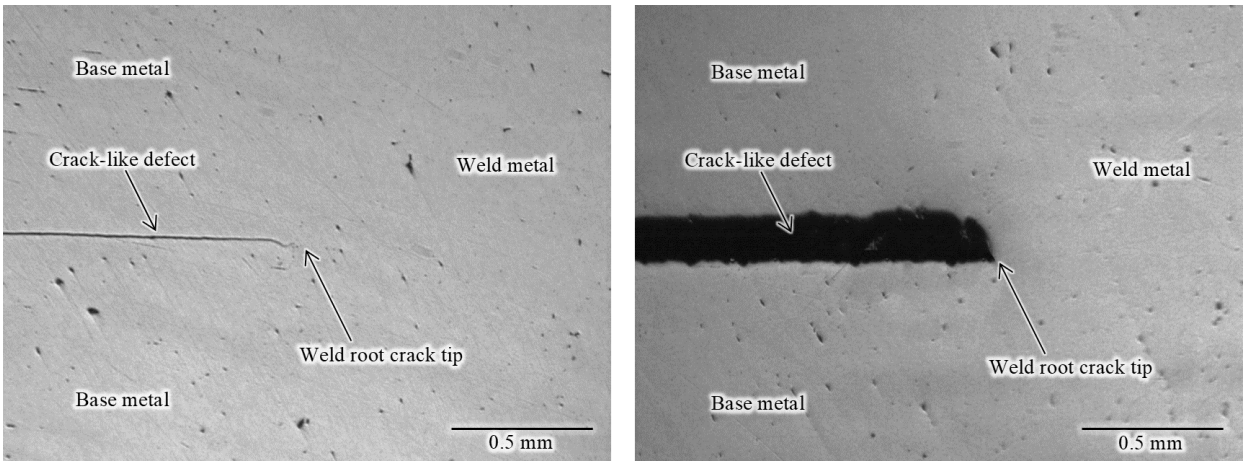

(a) (b)

Figure 1.3: Micrographs of weld root crack tips untested at the end of PJP welds: (a) a specimen with a small plate gap and (b) specimen with a large plate gap

Avoiding component failure in order to meet the life prediction is essential for hydropower generation projects. Fatigue cracks in this case tend to nucleate early or even after some years of operation. The failure mechanism in turbine runners is considered to be a combination of low cycle fatigue (LCF) from infrequent runaway cycles and operational start/stop, and high cycle fatigue (HCF) due to power output variation and small cycles of hydraulic load fluctuations [4, 5]. The fatigue life prediction method of industrial partner is based on the fracture mechanics theory with a conservative fatigue crack growth (FCG) design curve [6]. Linear summation of crack growth is used to account for variable amplitude loading [7, 8].

1.2 Problem statement and research motivation

The actual prediction method of industrial partner, used to estimate FCG lifespan for the partial penetration at the weld root, is an in-house conservative fracture mechanics method. Hence, there is no unique experimental fatigue data on root cracking of turbine runners under bending fatigue to validate the actual prediction method. In the continuous struggle to consider HSE, maintain efficiency, and reduce fabrication costs, designers want to approach the structural integrity limits of hydropower turbines by decreasing the penetration of welds. Major challenges motivate this research, which are summarized in the following questions related to the fatigue life of weld root cracking and of weld toe failure:

- What is the crack behavior at the weld root in the PJP weld?
  - Is there a fatigue crack initiation life at the root of the defect?
  - Is there a fatigue endurance limit at the weld root?
  - Is there a more simple design approach than the one currently used by the industrial partner?
  - Is there crack bifurcation during propagation at the weld root?
  - Is the standardized ASTM E647 [9] crack growth test representative of the crack growth behavior in the studied joints?
- Does PJP weld in comparison to CJP weld result in shorter fatigue life under bending?
  - What is the fatigue life characterizing the failure at the weld toe?
  - What is the fatigue life for different geometries of welds triggering failure at the weld root?
  - What is the minimum weld joint penetration depth to trigger failure at the weld toe (in PJP welds)?

1.3 Research objectives

To follow the aspects of structural integrity of turbine runner weldment, the principal objectives are classified as general and specific considerations.

1.3.1 General objectives

The goal of the current research is to pursue some of the less understood aspects of the PJP bases pointed out above in the area of low cycle and high cycle bending fatigue of turbine runner steel subjected to constant amplitude loading. We aim at generating unique experimental fatigue data that would eventually lead to a better understanding of the damage accumulation from root cracking and the fatigue strength of weld toe. The obtained results are expected to enhance the accuracy of fatigue life predictions in the design integrity.

1.3.2 Specific objectives

- Investigate the influence of weld joint penetration depth and weld metal on bending fatigue strength;
- Obtain a clear insight into the fatigue failure mode transition between weld root and toe cracking;
- Evaluate stress intensity factors (SIFs) of weld root cracks and stress concentration factors (SCFs) of weld toe notch;
- Propose a life prediction approach to the industrial partner from unique experimental fatigue data on root cracking;
- Assess the fatigue crack growth (FCG) behavior of the welded specimen and compare with the FCG behavior of literature data;
- Acquire a better understanding of the crack propagation approach to predict fatigue life at the weld root crack.

1.4 Originality of the research

Results are expected to contribute to a deeper understanding of the damage accumulation from root cracking and to answer some of the questions regarding different fracture mechanisms at cruciform joints (e.g., weld root cracking and weld toe failure). The originality and the anticipated impact of the current research work include:

- Acquisition of unique experimental data on root cracking in welded joints under bending fatigue;
- Understanding of the effects of weld joint penetration depth and first weld pass on fatigue strength;
- Determination of some conditions for failure mode transition between weld root cracking to weld toe cracking;
- Characterization of fatigue strength behavior at the weld root in HCF range;
- Proposition of a fatigue life prediction method for turbine runners.

1.5 Thesis outline

This dissertation is organized as follows:

Chapter 2 gives an overview of critical literature review related to the main themes of the research work. To present and analyze fatigue data, a general literature review of fatigue assessments is outlined. Influencing parameters on fatigue behavior, materials used in fabrication of turbine runners, and numerical methods for SIF calculation are then reviewed. Finally, different elements of fatigue life of the analogous cruciform fillet welded joint to the partially penetrated welded joint in the turbine runner are critically discussed.

Chapter 3 presents the experimental and numerical methodologies of this study. The design and the fabrication of the load-carrying cruciform fillet welded joint, developed to characterize the weld root cracking as well as weld toe cracking under three-point bending load, are explained in detail. The experimental procedure including the preparation of bending setup, monotonous bending tests, and fatigue testing condition are described. For center crack and load-carrying cruciform joint geometries, the numerical methodology for SIF calculation is then explained.

Chapter 4 gives the fatigue life results including crack initiation life and propagation in load-carrying cruciform fillet welded joints under three-point bending load.

Chapter 5 focuses on the numerical computations. The assessment of mode I and mode II SIFs are presented. Afterwards, the SIFs and the non-singular *T*-stress at the weld root crack tip, and stress concentration factors (SCFs) at the weld toe notch for the studied geometries are calculated.

Chapter 6 contains elements of general discussion including the main contributions of this dissertation at different stages. Failure mode transition between weld root cracking and weld toe failure, consolidation of the weld root fatigue strength of different weld penetration depths, and weld root FCG behavior in three-point bending are analyzed. The crack propagation approach is employed to predict fatigue life at the weld root of cruciform joint.

Chapter 7 provides conclusions, remarks, and suggestions for future studies, and describes how this dissertation has fulfilled its defined objectives based on the results presented in Chapters 4 and 5, and the discussion made in Chapter 6.

CHAPTER 2 LITERATURE REVIEW

2.1 Theoretical background of fatigue assessment

Fatigue is a mechanism in which the accumulation of substantial damages through successive individual cyclic loading results in the failure of a structure. During the service period, components of structure, such as hydro-turbine runners, are generally subjected to external fluctuating loads. These cyclic loads can contribute to crack nucleation and propagation, which lead to fatigue failure if their range is above a certain threshold. The cracks either pre-exist as pores or defects at the time of fabrication or are created by service circumstances. The crack growth ought to be foreseen to provide directives for inspection intervals, which ensure that cracks will halt propagating and failing prior to detection. In the case of fatigue, critical component models and/or experimental results are useful in predicting the lifetime of a component.

Fatigue assessment of components subject to fluctuating loads is necessary for design integrity. Different approaches exist for the fatigue assessment procedure including the rather conventional stress-based, notch stress intensity factor, and crack propagation approaches.

2.1.1 Stress-based approach

Wöhler (1860) [10] introduced the stress to number of cycles to failure (*S*–*N*) curve which is generally obtained from several numbers of fatigue cyclic tests at different stress levels lower than the yield strength. The stress is usually plotted as stress range ($\Delta\sigma$), stress amplitude (σ_a), or maximum stress ($\sigma_{\max}$). A logarithmic plot of the stress range (fatigue strength) versus the number of cycle (fatigue life) gives the Basquin relation (1910) [11] of the form:

$$\Delta\sigma_n = AN_f^b \tag{2.1}$$

where $\Delta\sigma_n$ is the nominal stress range; N_f is the number of cycles to failure; A is the material parameter related to the fatigue strength coefficient σ_f; and b is the fatigue strength exponent

(with negative sign). This stress-based fatigue is appropriate for applications in the high cycle fatigue (HCF) regime where the material behavior is predominantly elastic. The high stress is accompanied by plastic strain and leads to short fatigue life.

Fatigue resistance data of a component are commonly presented in terms of *S–N* curve owing to the simplicity of stress calculation. The nominal stress approach, however, disregards the local stress raisers such as structural discontinuity including a weld, and the stress is merely calculated by commonly agreed formula available for a simple geometry [12]. According to recommendations for fatigue design of welded joints and components presented by Hobbacher (2016) [13], the stress in a component can be resolved using general theories, e.g., beam theory. Variations within structural details induce an increase in the scatter of *S–N* data. Problems emerge when each structural detail requires its own fatigue data. Therefore, a good compromise needs to be defined in the various fields of application [14].

2.1.2 Notch stress intensity factor approach

Williams (1952) [15] used the theory of the elasticity and showed that the asymptotic stress state near a re-entrant corner is singular and its degree of stress singularity is a function of the notch opening angle 2α and acuity ρ (roundness). With zero notch angle and acuity, the stress level at the pointed crack or slit tip is described by the stress intensity factor (SIF) [16]. The linear elastic SIF, denoted K, is a function of applied nominal stress σ_n and crack length *a* by setting:

$$K = Y\sigma_n\sqrt{\pi a} \tag{2.2}$$

where *Y* is the geometry factor. For the notch stress intensity factor (N-SIF) approach, the stress in the *S–N* curve can be replaced by SIF. This approach can actually be given as a function of structural detail and related to the fatigue behavior of severe cases of stress concentration. In fact, the crack initiation and crack propagation are not controlled by the structural stress, and they can be described by the N-SIF concept [17]. The crack SIF is a particular case of N-SIF. Three independent modes, i.e., tensile opening (mode I), in-plane shear (mode II), and out-of-plane shear (mode III), commonly describe the local stress singularity. Figure 2.1 shows different crack loading

modes. When $2\alpha = 0$ and $\rho = 0,$ the loading modes related to the crack SIF are noted $K_I,$ $K_{II},$ and K_{III}.

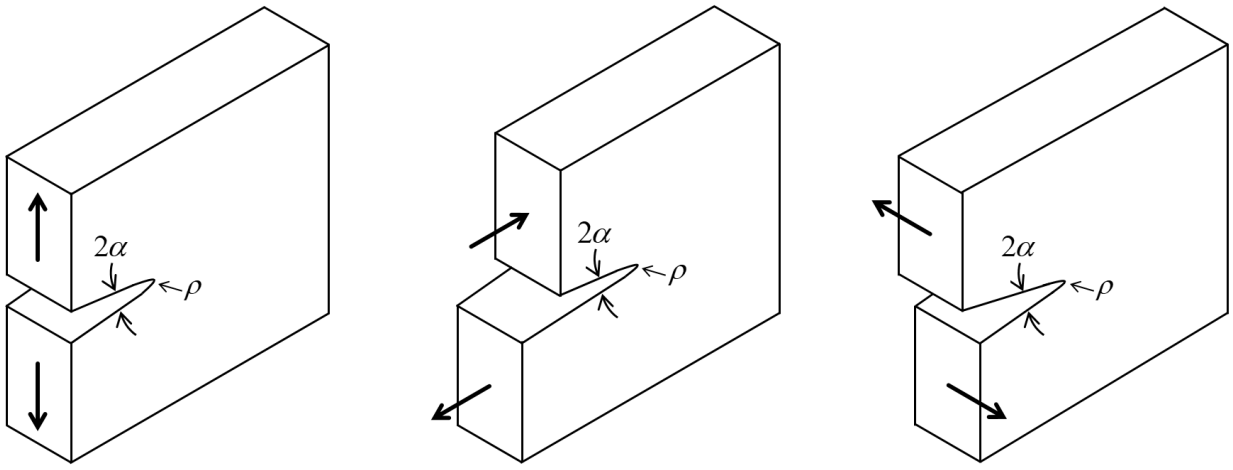

Mode I: Tensile opening Mode II: In-plane shear Mode III: Out-of-plane shear

Figure 2.1: Three loading modes

The N-SIF concept can advantageously describe crack initiation at sharp corner notches [18, 19]. The SIF concept has been extended for pointed V-notches and for rounded notches. The stress intensity of these extensions depends on the notch opening angle $(2\alpha \neq 0)$. Here, the loading modes related to the N-SIF are $K_1,$ $K_2,$ and $K_3.$ Rounded notches $(\rho \neq 0)$ can have a U- or V-shape in two variants of blunt notches and keyhole with finite notch stress. The generalized N-SIF of the loading modes are $K_{1\rho},$ $K_{2\rho},$ and $K_{3\rho}$.

In 1985, the practical application of this approach was demonstrated in the fatigue strength design of spot welded joints [20]. In the cruciform joints, the large scatter of the nominal stress approach in the *S–N* curve due to variation in the structural details was reduced to conventional ranges of geometrically uniform specimens by using the N-SIF approach [21, 22].

2.1.3 Crack propagation approach

The crack propagation approach, or fracture mechanics approach, considers the fatigue crack growth (FCG) behavior from initial to final crack length to predict the fatigue life. Paris' power law (1963) [23] describes the linear relationship between the fatigue crack growth rate (FCGR) $\mathrm{d}a/\mathrm{d}N$ and the SIF range ΔK in bi-logarithmic scale as:

$$\frac{\mathrm{d}a}{\mathrm{d}N} = C\Delta K^m \tag{2.3}$$

where C and m are material constants of fatigue crack propagation, and $\Delta K = K_{\max} - K_{\min}$ is the SIF range. Here, $K_{\max}$ and $K_{\min}$ represent the maximum and minimum values of elastic SIF, respectively. The Paris linear relationship is only valid between the threshold SIF range ΔK_{th} under which there is no crack propagation and rapid fracture with the critical SIF K_C. The variation of load ratio $R = K_{\min}/K_{\max}$ needs to be considered. The load ratio which is also called stress ratio is normally defined based on stress, $R = \sigma_{\min}/\sigma_{\max}$. Fatigue life of crack propagation can be calculated by solving Paris' power law for $\mathrm{d}N$ and integrating both sides ($\int \mathrm{d}N = \int \mathrm{d}a/(C\Delta K^m)$).

According to the International Institute of Welding (IIW) guideline for the assessment of weld root fatigue presented by Fricke (2013) [24], the crack propagation approach is appropriate for a long crack in linear elastic fracture mechanics (LEFM). In addition, the component fatigue assessment is applicable when crack initiation life is negligible. In practical application, the prediction of crack bifurcation and the SIF calculation for the corresponding crack path are two difficulties of this approach. These difficulties of practical application are in contrast with the simplicity and clearness of the theory [14].

2.2 Influencing parameters on FCG behavior

The SIF is regularly considered to be the sole parameter dictating the FCGR. The fatigue crack closure has an effect on shielding the crack. The singular stress level around the crack tip is described by the SIF, influenced by the crack-parallel non-singular *T*-stress and by residual stresses

induced by the welding process. In order to understand the FCG behavior of materials, it is very helpful to differentiate the various parameters affecting the FCGR.

2.2.1 Fatigue crack closure

Except for high load ratio, the FCGR can be affected by the crack closure induced by plasticity in the near threshold regime and more or less in the Paris regime. Elber (1970) [25] showed that under cyclic zero-to-tension loading $(R = 0)$, the crack was partially or completely closed at loading slightly higher than zero. In front of the growing fatigue crack tip, the large tensile plastic strains are not fully released during subsequent unloading. The induced plastic wake leads to the formation of a compressive residual stress behind the crack tip that results in crack face contact before complete unloading.

The premature crack face contact leads to a crack opening SIF K_{op} which may be larger than $K_{\min}$. This phenomenon, plasticity-induced crack closure, therefore has an influence on FCG behavior [26]. The load range where the crack tip is fully open, $\Delta K_{eff} = K_{\max} - K_{op}$, is noted to be the effective SIF range governing FCGR. The effective part of the SIF, is implemented to determine the FCGR according to Equation (2.3) [24]. The crack closure ratio U is defined as:

$$U = \frac{K_{\max} - K_{op}}{K_{\max} - K_{\min}} = \frac{\Delta K_{eff}}{\Delta K} \tag{2.4}$$

By increasing the load ratio R at a constant $K_{\max}$, $K_{\min}$ increases above K_{op} and that makes ΔK_{eff} equal to ΔK. The FCGR at different load ratios can be shown as a single curve using ΔK_{eff} [27].

In the near threshold regime, the FCG behavior can also be affected by asperity ridges owing to the roughness of the fracture surfaces [28], or corrosion debris (or oxidation) created along the crack surfaces [29]. The contact of macroscopic rough fracture surfaces caused by the misfit is called as roughness-induced crack closure. Either local mode II or III can take place at a macroscopic mode I due to material microstructural anisotropy and inhomogeneity. This leads to local displacement on the fracture surfaces. The existence of corrosion debris or oxide layer on the fracture surface leads to corrosion debris-induced crack closure (often denoted as oxide-induced

crack closure). These sliding crack surface interferences are more pronounced under mixed-mode loading and in the near threshold regime [30].

Experimental and numerical studies of crack closure by Blom and Holm (1985) [31] indicated that the closure effect in plane stress condition is more than that in plane strain condition. Davidson (1991) [32] showed that the level of closure is different for the center notch specimen compared to the single edge notch specimen. Despite numerous investigations supporting the crack closure importance, several lines of evidence doubt this phenomenon [33]. McEvily (1988) [34] concluded that the plasticity-induced crack closure has a minor effect on FCGR. Louat et al. (1993) [35] stated that plasticity at the crack tip does not induce crack closure, and the effect of roughness-induced crack closure and oxide-induced crack closure is small and insignificant unless the crack is completely packed with asperities. The majority of studies in the last two decades have considered the crack closure effect as a significant key to better understand the effect of load ratio on FCG behavior [36, 37]. The critical review of Pippan and Hohenwarter (2017) [30] concludes that the ΔK_{eff} describes $\mathrm{d}a/\mathrm{d}N$. Figure 2.2 schematically illustrates the different crack closure effects on FCG behavior in ductile materials where ΔK_{eff} controls the $\mathrm{d}a/\mathrm{d}N$. In practical situations, it is a major difficulty to separate the effective part of each crack closure effect.

2.2.2 Non-singular *T*-stress

Analytically, the stress state at the crack tip in the elastic case is given by the singular stress component of SIF and by the non-singular stress terms. Terms $O(r^{1/2})$ and T are non-singular stress terms in the Williams series expansion [38], where r is the distance from the crack tip in polar coordinate system. $O(r^{1/2})$ is a non-zero term only close to the outer boundaries of the specimen and $\lim_{r\to 0} O(r^{1/2})$ is equal to zero. The term T, a constant stress over a large distance in front of and behind the crack tip, is only due to a symmetric component of loading (mode I) and vanishes in antisymmetric field (pure mode II) [39]. It means that only the normal stress parallel to the crack plane, x-direction stress, is non-zero. Leevers and Radon (1982) [40] proposed a dimensionless parameter called the stress biaxiality ratio B, which can be regarded as a geometry-independent

counterpart of the crack tip stress field parameters. The *T*-stress is necessarily proportional to the reference stress and it is normalized as stress biaxiality ratio as:

$$B = \frac{T\sqrt{\pi a}}{K_I} \tag{2.5}$$

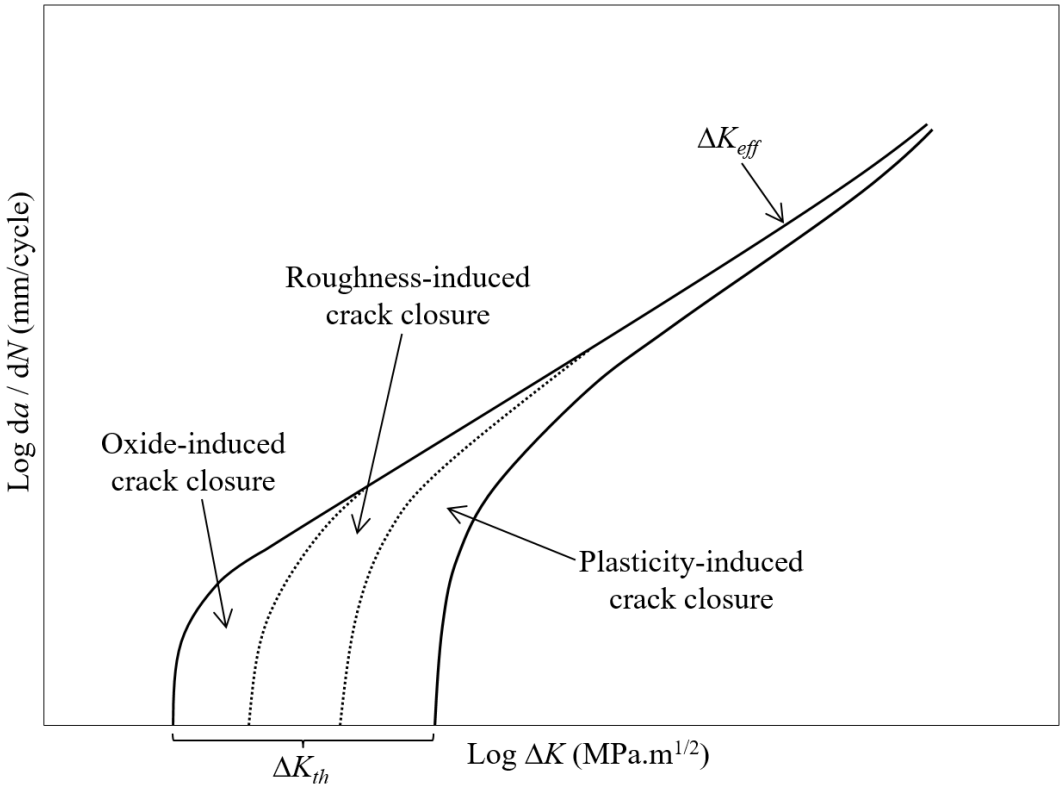

Figure 2.2: Schematic illustration of different crack closure effects on FCG behavior

By replacing K_I with equivalent SIF, $K_{eq} = \sqrt{K_I^2 + K_{II}^2}$, the equation can be extended to mixed-mode problems. The stress triaxiality at the crack tip is reduced by the negative (compression) *T*-stress and is strengthened by the positive (tension) *T*-stress [41]. Negative *T*-stress directs to loss of crack tip constraint while positive *T*-stress leads to high crack tip constraint. Tong (2002) [42] demonstrated that the crack closure often has an influence on FCGR near the threshold region and the difference in FCGR becomes apparent in the mid-range due to *T*-stress effect. Fleck

(1986) [43] examined theoretically the influence of T/σ_y on the crack closure response of a growing fatigue crack. He found that the amount of crack closure decreases with increasing T/σ_y at $R=0$. Despite prior evidence, Hutar et al. (2006) [44] showed that the crack closure is not significantly influenced by the *T*-stress values.

There are important differences in FCGR of various geometries made from the same material when the $\mathrm{d}a/\mathrm{d}N$ is correlated with ΔK. Tong (2002) [42] observed the discrepancies in FCGR of different specimens. The lowest FCGRs were obtained using single-edged tension and center cracked tension specimens with a negative *T*-stress while the highest FCGRs using compact tension (CT) specimen with a positive *T*-stress. For a given ΔK, negative *T*-stress promotes lower FCGR due to the loss of constraint while positive *T*-stress produces higher FCGR by restricting the development of local plastic flow. In contrast, Knesl and Hutar (2002) [45] and Varfolomeev et al. (2011) [46] reached an opposite conclusion suggesting that the FCGR for a given ΔK was lower for the CT specimen with a positive *T*-stress than for the center cracked tension specimen with a negative *T*-stress.

Several methods have been proposed to correlate the FCGR with two-parameter fracture mechanics. Larsson and Carlsson (1973) [39] found significant discrepancies in the results of fatigue crack propagation for different geometries. Only a two-parameter boundary layer formulation of *K* and *T* was able to unify the results. The shortcoming of their study is that they did not extend mode I case to the general mixed-mode case. Ayatollahi et al. (2018) [47] studied the effect of specimen geometry of CT and double cantilever beam with positive *T*-stress and of Brazilian disc with negative *T*-stress on FCGR. The proposed generalized strain energy density criterion, which took into account both *K* and *T*, improved the predictions for FCG.

2.2.3 Welding residual stresses

Welding residual stresses are often produced in the fusion welding processes due to the high-induced thermal loads and microstructure change of the welded materials. These residual stresses can cause deformations and distortions in the welded components, and in a majority of cases, they can reduce the strength, load bearing capacity, and the lifetime of welded structures [48]. To assess the component integrity, influence of the residual stress field on FCG behavior has to be properly

understood. The welding residual stress is a pre-existing load which is superimposed on the applied cyclic stress. Compressive residual stress introduces a favorable effect on fatigue strength by closing the crack faces, whereas tensile residual stress leads to a detrimental effect by opening. There exist two complementary approaches. One utilizes the principle of superposition and the other applies the crack closure model.

For the superposition approach, the cyclic maximum and minimum SIFs can be derived from the mutual effects of external and residual stresses on the crack tip stress field. The SIF of a crack tip can therefore be written as the superposition of the SIF from remote uniform stress and residual stress. As presented by Parker (1982) [49], the principle of superposition can be used to calculate the effective SIF range ΔK_{eff} in order to consider the residual stress field by:

$$\Delta K_{eff} = (K_{\max} + K_{res}) - (K_{\min} + K_{res}) \tag{2.6}$$

$$R_{eff} = \frac{K_{\min} + K_{res}}{K_{\max} + K_{res}} \tag{2.7}$$

where K_{res} is the SIF due to residual stress, and R_{eff} is the effective load ratio. The tensile residual stress does not influence the SIF range $(\Delta K_{eff} = \Delta K)$ while the effective load ratio can vary along the surface crack front. Ma et al. (2011) [50] stated that the effective SIF range is independent of residual stress, which adds to the mean stress and alters the effective load ratio. This approach disregards the effect of crack closure. Beghini and Bertini (1990) [51] observed lower FCGRs in the welded CT specimen due to the presence of compressive residual stress fields. Li et al. (1995) [52] noted that the compressive residual stress can markedly increase the effect of crack closure when $R_{eff} = 0.$ They assumed that the SIF due to residual stress is simply superimposed on $K_{\max}$, then:

$$\Delta K_{eff} = (K_{\max} + K_{res}) - K_{op} \tag{2.8}$$

In the crack closure approach, the effective SIF range, representing the opening portion of the SIF range, can be calculated from $U\Delta K$ as proposed by Newman (1984) [53]. In this approach, the $\mathrm{d}a/\mathrm{d}N$ versus ΔK measured at different load ratios can be replaced by a master curve of $\mathrm{d}a/\mathrm{d}N$

versus ΔK_{eff}. For the CT specimen with or without post-weld heat treatment (PWHT), Link (1990) [54] conducted FCGR experiments; a strong influence of welding residual stresses on the measured FCGRs due to the crack closure effects was observed. The effect of residual stress on crack closure is less well studied. It is widely accepted that compressive residual stress increases the magnitude of crack closure, whereas tensile residual stress has the opposite effect.

Li et al. (2018) [55] showed that the compressive residual stress field has a significant effect on the short crack growth; both decrease in FCGRs and increase of fatigue threshold are noticed in comparison with short crack free of residual stress. Chernyatin et al. (2018) [56] studied the effect of welding residual stress including crack tip constraint of non-singular *T*-stress on the surface fatigue crack propagation. Owing to the effect of welding residual stress and local non-singular *T*-stress along the crack front, the semicircular internal surface crack in welded joint of the pipeline turned to the semielliptical. The shortcoming of this study is that they did not consider the effect of local near-tip plasticity (crack closure).

A thorough search of the relevant literature revealed that the effect of a combination of fatigue crack closure mechanisms, non-singular *T*-stress, and residual stress distributions during the crack propagation on the FCGR has not been investigated.

2.3 Materials knowledge

A martensitic stainless steel is extensively used to manufacture the turbine runners due to its good weldability, mechanical and fatigue properties, and resistance to corrosion and cavitation. Cast martensitic alloy CA6NM (13Cr-4Ni) conforming to ASTM A743/A743M [57] is used more often as base metal, e.g., blades and hub (band/crown), in the hydraulic turbine runner fabrication. AISI 415 (UNS S41500) steel conforming to the ASTM A240/A240M [58] is the wrought version of CA6NM.

Matching filler material E410NiMo (NiMo 0.02%C) is used to join blades to the body. This wire of flux-cored arc welding (FCAW) based on AWS A5.22 is a martensitic weld metal [59]. The PWHT proposed by the American Welding Society (AWS) is to heat between 595 °C and 620 °C, hold for one hour (−0, +15 minutes) followed by air cooling to the ambient temperature. In addition,

austenitic filler material E316L can be used without the need of preheating and PWHT [59] unless if properly hammer-peened.

Different characteristics and properties such as tension tests, hardness measurements, impact strength, fracture toughness, and FCG behavior along with an evaluation of the microstructure and analysis of the chemical composition for these materials were measured [6, 8, 60, 61]. Lanteigne et al. (2008) [8] compared the different mechanical properties and also the fatigue crack propagation of CA6NM provided by two different foundries.

Chaix (2014) [62] studied the influence of tempering temperature and the amount of resulting reformed austenite on the fatigue crack propagation of CA6NM. It was observed that there is an increase in the threshold limit and a reduction in the FCGR when the tempering temperature leads the formation of reformed austenite. It is mainly due to the increase of the closure induced by internal compression stress. Akhiate (2015) [63] studied the effect of the carbon contents of 0.018, 0.033, and 0.067% on the fatigue crack propagation of CA6NM. For the tempering temperature of 550 °C, the carbon content has no significant effect on the FCGR while it has an effect on the threshold region.

Trudel (2013) [64] surveyed the fatigue crack propagation variations in the three weld zones of as-welded and heat-treated CT specimens, made of CA6NM welded joint using a matching filler metal E410NiMo. The as-welded situation is representative of in situ repairs by weld deposition that cannot easily be heat-treated. The test was performed at constant SIF ranges of $\Delta K = 8$ and 20 MPa.m$^{1/2}$ with $R = 0.1$. For heat-treated specimens, the higher FCGR was observed in the heat-affected zone (HAZ), and compared to the weld metal, the base metal showed more fatigue crack resistance. Owing to the tensile residual stress acting on the crack tip and therefore hindering crack closure, the higher FCGRs were always found in the three zones of as-welded specimens compared to heat-treated specimens. For as-welded specimens, higher FCGR was observed in the weld metal, and the base metal showed slightly more fatigue crack resistance compared to the HAZ. The weld metal with fine martensitic microstructure presented a linear crack path and a worst resistance to FCGR, whereas the tendency to follow martensite laths of coarse microstructure was the reason for the tortuosity extent of the crack path and for resistance to FCGR in the base metal specimens. The FCGR in the HAZ was between weld and base metals, and crack bifurcation was more frequent from the fusion line towards the base metal due to mismatch of weld and base metal

yield strengths. The FCGR in HAZ decreased after weld metal and then stabilized in the base metal at both SIF ranges of $\Delta K = 8$ and 20 MPa.m$^{1/2}$.

In addition, FCG behavior in the HAZ was presented for as-welded and heat-treated specimens at $R = 0.1$ and 0.7 [64]. For a fully open crack at $R = 0.7,$ the FCGRs of as-welded and heat-treated specimens were similar and comparable to that of base metal [6, 8]. Therefore, tensile residual stress did not have a profound effect at this load ratio. FCGRs in the mid-range of as-welded and heat-treated specimens were similar to that of base metal at $R = 0.1.$ Owing to the effect of tensile residual stress in the near threshold, as-welded specimen showed similar FCGR to the base metal at $R = 0.7.$ By relieving tensile residual stress, the useful effect of PWHT was obvious in the near threshold at $R = 0.1$ while it did not have a noticeable effect at $R = 0.7.$ When corrected for crack closure by plotting $\mathrm{d}a/\mathrm{d}N$ versus $\Delta K_{eff},$ the FCGRs of the as-welded and heat-treated at both load ratios unified into a single curve.

Deschênes (2016) [65] studied the fatigue crack propagation in the CT specimen made of AISI 415 at $R = 0.1$ and 0.7. By excluding the crack closure effect in the CT specimen at $R = 0.1,$ FCGR became close to that at $R = 0.7.$ Figure 2.3 shows that the fatigue crack closure at $R = 0.1$ is important for applied SIF range lower than 21 MPa.m$^{1/2}$.

Besides, he [65] surveyed the effect of geometry (*T*-stress) on the FCGR in AISI 415. A new geometry similar to the CT specimen was fabricated from the same material. This geometry has a negative stress biaxiality ratio of 0.1 to 0.4 in the range of $a/W = 0.45$ to 0.8 while the CT specimen has a positive stress biaxiality ratio of 0.528 to 0.599 in the range of $a/W = 0.4$ to 0.7 (W is the width of the CT specimen) [40]. The non-singular *T*-stress had an effect on the fatigue crack closure as the negative *T*-stress increases the crack closure effect which can also decrease FCGR mainly near threshold [43, 66, 67]. The CT specimen with positive *B* value had a FCGR nearly 500% larger than the new geometry with negative *B* value at $R = 0.1.$ The difference was merely 20% at $R = 0.7.$ By excluding the crack closure effect in the new geometry at $R = 0.1,$ the FCG behavior did not superimpose perfectly on the crack propagation at $R = 0.7;$ indeed, FCGRs were noted to be 66% less at $R = 0.1.$ The inconsistency between the results was explained by the crack tip shielding which is the mechanism of promoting the reduction of elasto-plastic deformation at the crack tip. Additionally, Deschênes [65] investigated the effect of residual stress

on the FCGR. The welding residual stress induced in the new geometry showed that the crack tip tensile residual stress opened the crack faces, and it therefore eliminated the crack closure. Thus, FCGR measured in the new geometry with tensile residual stress at $R = 0.1$ was very similar to that of the new geometry without residual stress at $R = 0.7$. The similar conclusion was obtained from the work of Trudel [64] for as-welded specimen which showed similar FCGR near threshold at $R = 0.1$ in comparison with as-welded or heat-treated specimen at $R = 0.7$.

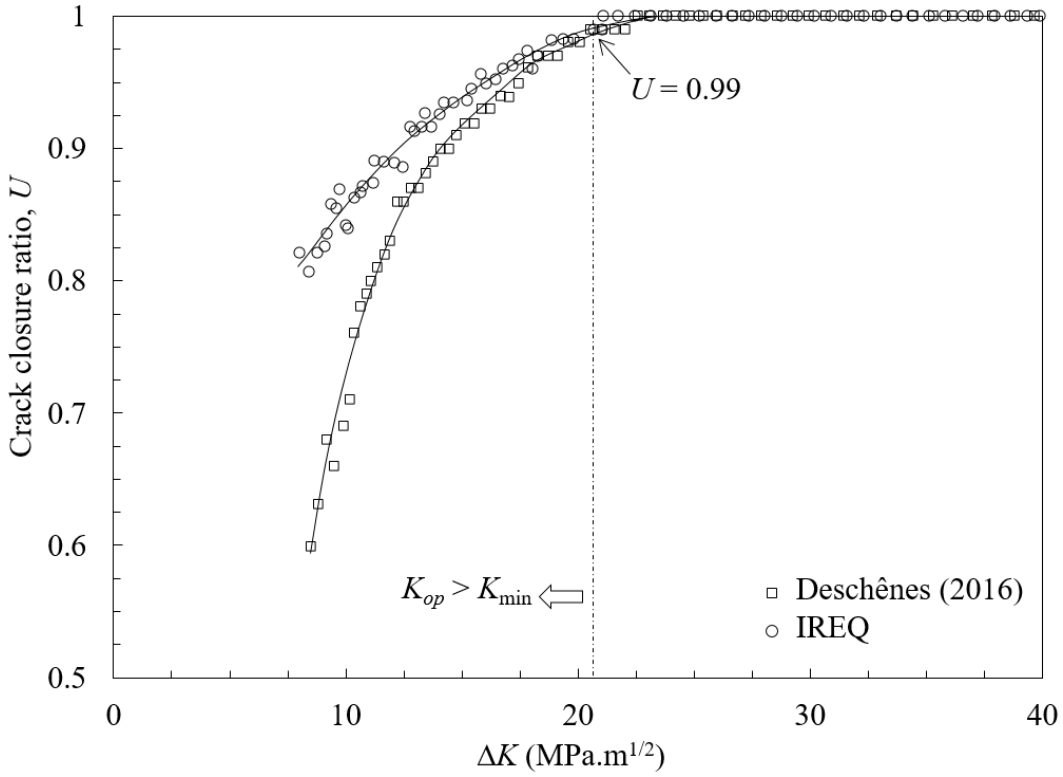

Figure 2.3: Crack closure ratio versus SIF range at $R = 0.1$ in the CT specimens made of AISI 415 (reproduced and adapted from Deschênes (2016) [65])

Al-Haidary et al. (2006) [68] surveyed the fatigue crack propagation in austenitic stainless steel 316L and its weldments E316L. Submerged arc welding and manual arc welding were used. The FCG behaviors were at either across the weld metal or through the weld metal, and the HAZ. Because of the microstructural changes, and also direction and distribution of the residual stresses, higher FCGRs were observed along through the HAZ and the weld metal compared to the base

metal or even across the weld metal direction (perpendicular to the weld zone). These changes in fatigue crack propagations were due to the directions of tensile and compression residual stresses resulting from solidification of the weld metal. Besides, the fatigue life in the manual arc welding was lower than the automated corresponding one in the submerged arc welding.

Figure 2.4 shows FCGR versus SIF range for martensitic (AISI 415, E410NiMo, CA6NM) [64, 65] and austenitic (316L and E316L) [68] stainless steels of base metal, weld metal, and HAZ at $R = 0.1$ and 0.7. The figure demonstrates clearly that the FCGRs of martensitic stainless steels are relatively lower than austenitic stainless steels. Turbine runners design methods use a conservative design curve (Figure 2.4) [6]. The design curve has significantly higher FCGR than the ones observed in the CT specimens made from martensitic stainless steel commonly used in the fabrication of turbine runners.

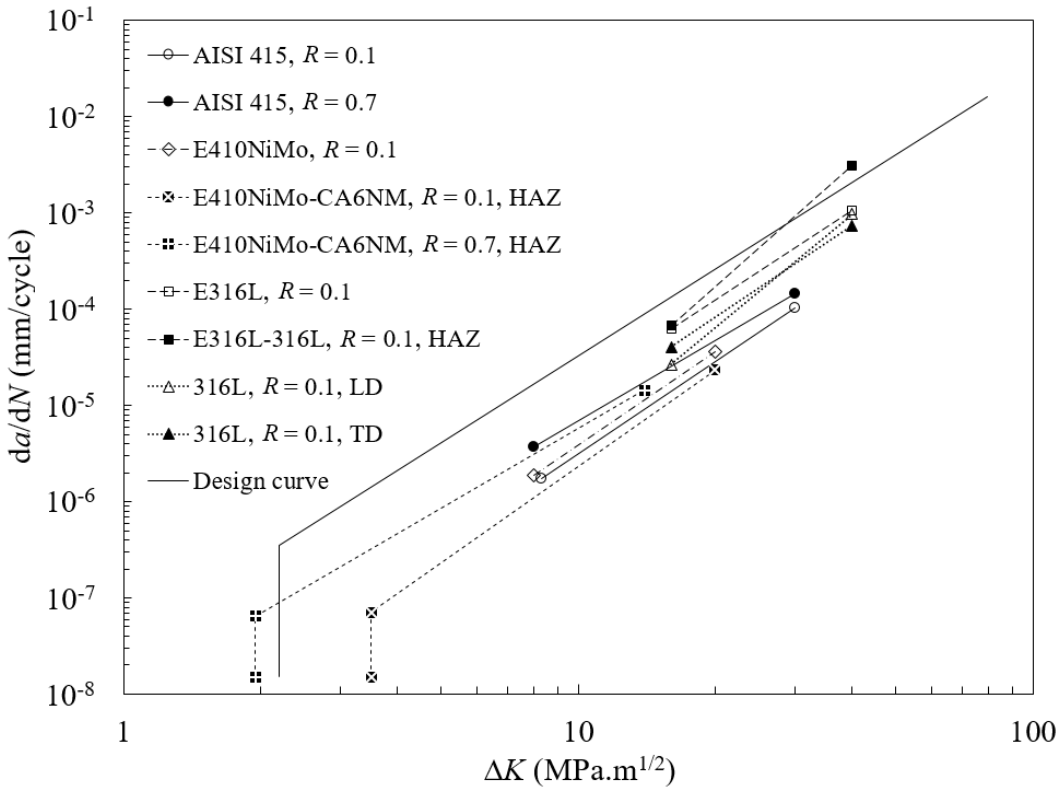

Figure 2.4: FCGR vs SIF range for martensitic [64, 65] and austenitic [68] stainless steels, and design curve [6]. LD and TD correspond to longitudinal and transverse of rolling direction, respectively

2.4 Numerical methods for SIF calculation

The FCGR can be calculated using the Paris' power law [23] if the SIF range characterizing the crack and its loading conditions are known. Hence, having an accurate calculation of the crack tip SIF range of a component is necessary to reliably predict fatigue life and prevent fatigue failure. There are analytical SIF solutions for typical crack geometries and loading conditions [69-72]. However, for an arbitrary crack in complicated components or under complex loading conditions, numerical methods are usually used to calculate the SIF [73]. The Finite element method (FEM) has the capability of solving problems with complex geometries and loading conditions. In LEFM, two sets of approaches are used to numerically calculate SIF. They are based on the near-tip field variable and the energy release approaches. The former approach can be further divided into stress-based [74, 75] and displacement-based [74, 76, 77] methods. The numerical studies have explored parameters influencing the accuracy of computed SIFs [78, 79].

2.4.1 Numerical *K*-solution methods

The SIF is calculated from the direct relationship between the *K* value and the near-crack tip field variable. These methods, stress- and displacement-based, have been developed to enhance the accuracy of SIF calculations. The crack tip element type was modified in order to represent the singular stress and strain field variations of $1/\sqrt{r}$. Byskov (1970) [80] added one node to the element to represent the singular stress field at the crack tip and to increase the number of degrees of freedom; however, the shortcoming is the compatibility conditions. Owen (1983) [81] improved the compatibility condition by increasing the number of neighboring elements. Strain singularity of $1/\sqrt{r}$ was calculated by modified elements. Barsoum [76, 82] proposed shifting the mid-side nodes to quarter-positions of quadrilateral and triangular isoparametric elements and it can be concluded that the Jacobian matrix of these elements is singular at the node representing the crack tip. The compatibility conditions with minimal neighboring element at the crack tip are the major advantages of these modified isoparametric elements.

For linear elastic materials, Paris and Sih (1965) [83] presented the analytical expressions for the displacement (u, v) of nodes parallel and perpendicular to the crack growth direction (Figure 2.5). When $r \to 0,$ higher order terms can be neglected and the expression simplified along the free

crack faces ($\theta = \pi$). As presented by Chan et al. (1970) [74] in the displacement extrapolation method (DEM), the SIF at the crack tip is extrapolated from the numerically calculated displacements in the vicinity from the crack tip to $r = 0$. Further explanation of this method is presented in Appendix A. This method requires a good numerical representation of the crack tip field with fine meshes. The method mainly focuses on modeling and meshing the near-tip field fitting. To represent the singular strain field at the crack tip, the quarter-point isoparametric elements suggested by Barsoum [76, 82] can be used. DEM is widely used because the nodal displacements are a primary output of the finite element program, and the SIF can be easily computed without the need for further post-processing. Furthermore, the fine mesh does not have a significant effect on the computing time owing to the continuous upgrading of computer technology.

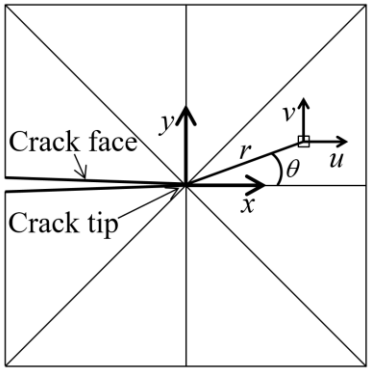

Figure 2.5: Coordinates for near crack tip field description

The SIF value can be derived from the energy release approach when the crack propagates in an elastic body [84]. Two parameters, the elastic strain energy and the SIF values, can be calculated from two conditions of crack increment. The methods to generate the crack increment include the energy release approach proposed by Watwood (1969) [85] to calculate the energy release difference between two averaged successive crack lengths. The virtual crack extension method was then proposed by Rice and presented in the works of Hellen (1975) [86] and Parks (1977) [87]. This method does not need the cumbersome simulation of two different crack lengths and the solution is for arbitrary crack tip motion.

In linear elastic materials, the path-independent *J*-integral for a cracked body presented by Rice (1968) [88] is equal to the energy release rate. To avoid a potential source of inaccuracy in the numerical calculation, the contour integral in the *J*-integral method is converted into an equivalent domain integral by Shih et al. (1986) [89]. Domain integral applies area and volume integrations for 2D and 3D problems, respectively. Area and volume integrals give much more accurate results than contour and surface integrals by using the *J*-integral method. The domain is set from the elements surrounding the crack tip for numerical assessment of the integral. To deal with a mixed-mode problem, Yau et al. (1980) [90] proposed the interaction integral method (IIM). Two independent equilibrium states of the cracked component are considered to separate modes I and II. State 1 correspond to the actual state for a given boundary conditions and state 2 correspond to an auxiliary state of either mode I or mode II near-tip fields. Equations related to this method are presented in Appendix A. The main advantage of the integral method is that coarse meshes can provide accurate estimations of the SIF [79, 91]. In addition, the contour or the domain integral far from the crack tip leads to an accurate SIF. It is therefore possible to determine *J* along various paths surrounding the crack tip.

Great efforts have been devoted to investigating different numerical *K*-solution methods. In the stress extrapolation method, stresses with lower precision are computed from the nodal displacement solution [79, 92, 93]. Accurate SIF calculation using various displacement-based methods requires a good numerical representation of the near-crack tip field fitting [78, 94]. Research has consistently shown that energy-based methods are more accurate than the near-tip field extrapolation methods [79, 92, 95]. The DEM and IIM are available in finite element codes, e.g., ANSYS® [96] and ABAQUS® [97].

2.4.2 Influencing parameters on SIF estimation

The effect of the selected element type on the accuracy of calculated SIF by different methods was analyzed by Han et al. (2015) [79]. The result is presented for typical crack geometries of center crack, eccentric crack, and edge crack. The use of quadratic element types results in a more accurate SIF calculation than linear element types. Guinea et al. (2000) [78] showed that adopting different shapes of the quadratic elements, 6-node triangle and 8-node quadrilateral elements, in the body itself had no noticeable effect on the accuracy of the calculated SIF by different displacement-

based SIF computation methods; however, Han et al. [79] did not find a consistent effect of different shapes on the results. Likewise, some investigators have compared regular element types, i.e., linear and/or quadratic elements, with singular element types, i.e., quadrilateral and/or triangular quarter-point elements, at the crack tip. They found that singular elements improve the accuracy of both displacement extrapolation [78, 94, 98] and *J*-integral methods [79, 98]. Lim et al. (1992) [94] compared various displacement-based SIF computation methods for center crack under tension and three-point bending specimens. They found that the quarter-point displacement technique with different quarter-point element sizes is generally more accurate than displacement extrapolation method with regular element type. Han et al. [79] found that *J*-integral values are stable in all integral paths when singular elements at the crack tip are used. The favorable effect of singular element types on the accuracy of SIF calculation is also presented in 2D and 3D finite element models of CT specimen by Qian et al. (2016) [92].

A number of studies investigated the influence of mesh configurations including element size and angular discretization on the SIF estimation [78, 79]. In ANSYS guide, the recommended first row of element size around the crack tip is $a/8$ or smaller, and roughly one element every 30° or 40° in the circumferential direction is proposed for a 2D model [96]. Guinea et al. [78] studied the effect of angular discretization from 3 to 9. Similar to the guide of ANSYS, approximately one element every 30° in the circumferential direction is recommended for a 2D model [78]. The element size was identified as the most influential factor for the numerically calculated SIF. Their study is limited to different displacement extrapolation techniques and the influence of local mesh refinement was not explored. Han et al. [79] numerically determined SIF for three element sizes ($a/10$, $a/20$, and $a/40$). They could not find any consistent effect of element size on the accuracy of SIF calculation by the DEM. They obtained K_I values with the *J*-integral method which agreed very well with the analytical solutions for three element sizes. Angular discretization and local mesh refinement were not surveyed by Han et al. The terms coarse mesh and fine mesh were used by Courtin et al. (2005) [91]; however, no precise quantification of the element size was provided. Most of the literature has focused on element size while there has been little discussion about angular discretization. Furthermore, no study has investigated the influence of local mesh refinement on the accuracy of mode I SIF estimation.

Both 2D and 3D models have been used to calculate the mode I SIF for a CT specimen [91, 92]. Qian et al. [92] determined that 2D models provide less accurate results than 3D models. Only a small number of studies have addressed the sensitivity of the SIF calculation accuracy to the Poisson's ratio of the material by displacement-based methods [78, 99]. Fu et al. (2012) [99] showed that the Poisson's ratio effects are more profound for the mode I SIF than the mode II. Although a number of comparative studies have been carried out in the past on mode I problems, there has been little discussion about mode II SIFs.

2.5 Fatigue of cruciform joint

Cruciform fillet welded joints have gained much attention owing to their broad applicability. They are commonly classified as either non-load-carrying or load-carrying. The partially penetrated welded joint in the turbine runners is assumed analogous to the thick load-carrying cruciform fillet welded joint (Figure 2.6a). The roundness of the weld toes is similar to a concave fillet weld, and the welded joint is partially penetrated. The complex loading condition in turbine runners is closer to simple bending than to pure bending.

Fatigue failure at the weld toe is prevalent in the complete (or full) joint penetration (CJP) fillet weld. However, fatigue cracking originating from crack-like defect is present at the weld root in the partial joint penetration (PJP) fillet weld. Locations of weld toe cracking and weld root cracking are shown in Figure 2.6b.

Figure 2.7 illustrates the load-carrying cruciform joints with flat face (mitre) and concave fillet welds, and under different loading conditions. Different fatigue assessment approaches such as nominal stress, structural or hotspot stress, effective notch stress, N-SIF, crack propagation, and strain energy density are employed in assessing the joint of weldments [100-104]. The IIW has published documents [13, 24] outlining the fatigue analyses of the cruciform weldments. Hobbacher (2016) [13] presented new recommendations for the IIW fatigue assessments of the weldments and a list of different structural details for fatigue resistance using the nominal stress method. The potential failure at the weld toe or weld root is limited to the structural detail of flat face fillet weld and the loading condition of tension (Figure 2.7a). For the same geometry type and loading condition, Fricke (2013) [24] also provided the guideline of the IIW on several fatigue

assessment approaches of the weld root. In the demonstration example, the effective notch stress, crack propagation, and strain energy density approaches are shown to be more conservative than the nominal stress and structural approaches.

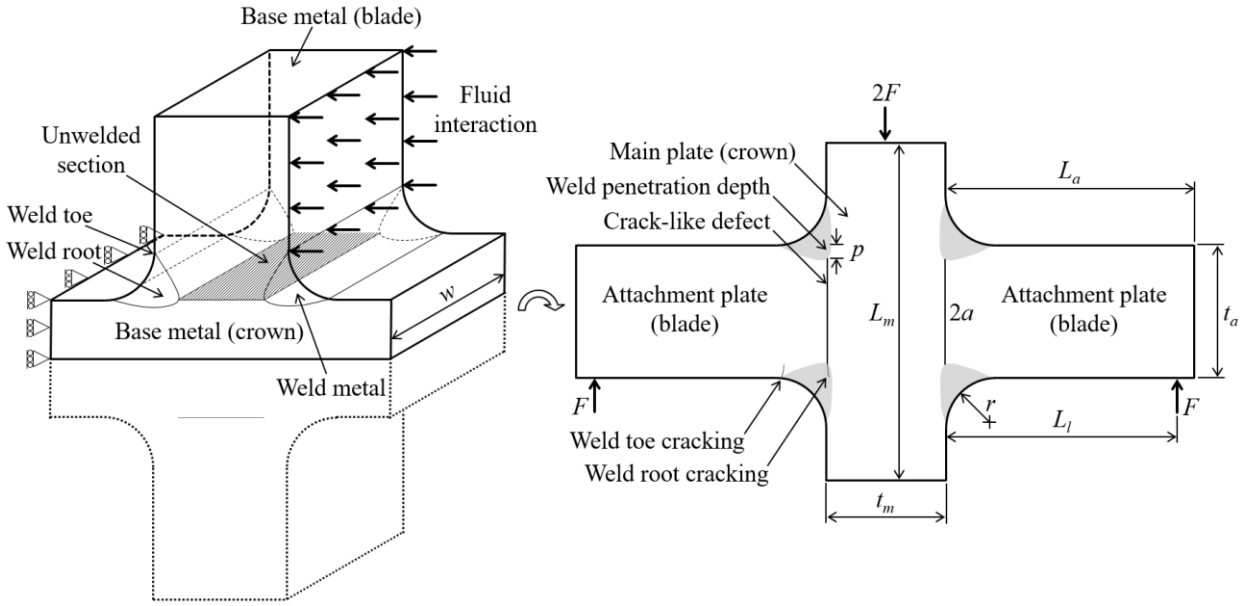

(a) (b)

Figure 2.6: Schematic view of the analogous load-carrying cruciform fillet welded joint to the partially penetrated welded joint in the turbine runners

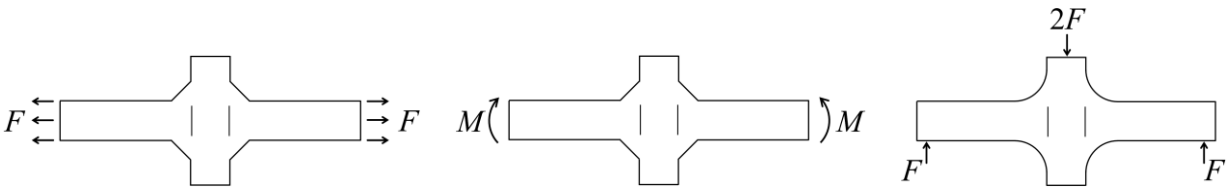

(a) Tension (b) Pure bending (c) Three-point bending

Figure 2.7: Load-carrying cruciform fillet welded joints: (a) and (b) flat face fillet weld, and (c) concave fillet weld

2.5.1 Fatigue failure mode transition

Two types of fatigue failure modes exist in a load-carrying cruciform fillet welded joint: cracking at the weld root and at the weld toe. Accordingly, two competing mechanisms characterize weld root and/or weld toe fatigue failures. The location of the most critical location depends highly on the throat thickness of the weld and thus the crack-like defect width [105, 106]. The condition leading to the transition between the two failure modes depends on the geometrical parameters of the weldment—the normalized critical weld root crack length and weld leg length (h in Figure 2.8) defined by the thickness of the plate [3, 107-110]. Fatigue failure mode transition between weld toe and weld root in structural steel is shown in Figure 2.8 [107].

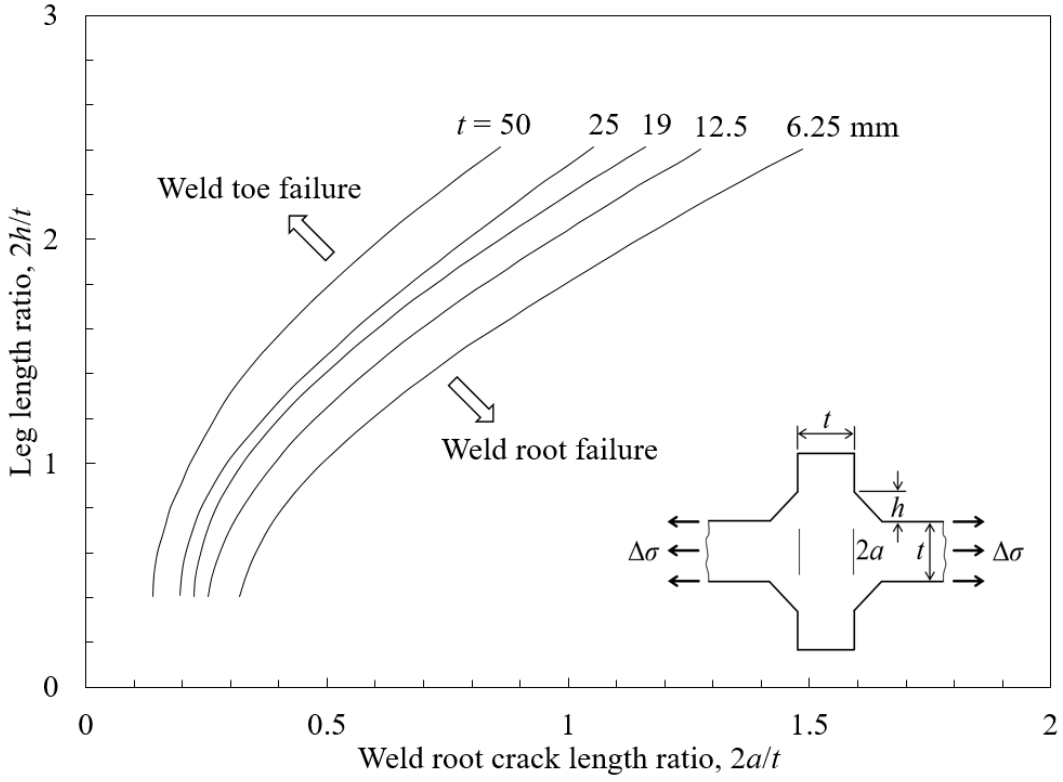

Figure 2.8: Fatigue failure mode transition between weld toe and root in the structural steel (reproduced and adapted from Maddox (1974) [107])

Further review of the literature, however, has shown that the transition between two failure modes cannot be characterized simply by the geometry parameters of the weld penetration depth and the weld leg length. The fatigue failure mode may also change with the magnitude of the applied stress at the load ratio of zero $(R = 0)$ [111-113]. Load-carrying cruciform fillet joints failed at the weld root during high stress fatigue loading, while the similar geometry weld toe exhibited fatigue failure at lower stress levels; this inconsistency has been explained by the existence of the different welding residual stress fields at the weld toe and the weld root [111, 112].

Understanding welding residual stress fields in the welded cruciform joint are important for better analyses of the fatigue behavior in the weldment. There is tensile residual stress near the weld toe and compressive residual stress in the vicinity of the weld root [114]. Barsoum and Lundback (2009) [115] conducted experimental and numerical analyses of residual stress fields in a T-joint fillet weld. Based on that study, it was found that there is high tensile residual stress near the weld toe while compressive residual stress is observed in the center of the plate. The residual stress distribution along a section at the weld root shows high compressive residual stress and tensile residual stress in the unwelded and welded sections, respectively.

The actual magnitude of residual stresses depends on the weld root plate gap and weld penetration depth. Kainuma and Mori (2008) [111] used numerical analysis to calculate the residual stress distribution at the weld toe and root of cruciform joint with flat face fillet weld. For zero plate gap, similar findings were obtained for residual stress fields by Barsoum and Lundback (2009) [115]. The model with a weld root plate gap showed relatively higher tensile residual stress at the weld toe due to the restriction in the unwelded portion. The tensile residual stress at the weld toe can decrease the fatigue life. The generated residual stress distribution along a section at the weld root resulted in higher compressive residual stress in the vicinity of the crack tip. The larger the compressive residual stress at the weld root, the greater the possibility of crack closure and hence enhanced fatigue life. In the case of two different weld penetration depths of welded tubular structures, Barsoum (2008) [116] performed experimental measurements and further numerical calculations of residual stresses at the weld root, where in both configurations compressive residual stress augmented for increasing weld penetration depth. Hence, the crack tip compressive residual stress can increase more the magnitude of crack closure for higher weld penetration depth.

It can be gathered from the aforementioned studies on the transition between modes that numerous investigations have been conducted focusing on the geometry of load-carrying cruciform joints with flat face fillet welds under fatigue loading condition of tension. However, so far none has studied the possible fatigue failure mode transition in the cruciform joint with a concave fillet weld under fatigue three-point bending.

2.5.2 Fatigue crack initiation and propagation at the weld toe

The research hitherto has tended to focus on the fatigue assessment of flat face fillet welds. The large scatter of weld toe failure in the *S–N* curve due to variation in the structural details of flat face fillet welds was reduced to conventional ranges of geometrically uniform specimens by applying the N-SIF approach [22]. For different geometry sizes, Lazzarin and Tovo (1998) [21] showed that the scatter in *S–N* curve of flat face fillet weld diminishes from ±40% to ±10% by employing the N-SIF approach, assuming K_1 is a meaningful parameter. Since the units of K_1 and K_2 at the weld toe (flat face fillet weld) are different from those of K_I and K_{II} at the weld root, the N-SIF fatigue assessment cannot be used for direct comparison of the weld toe and weld root failures [117].

The fatigue life can be predicted using crack propagation approach at the weld toe of flat face fillets. The crack initiation phase is often disregarded by assuming an initial crack length in the order of 0.1 mm, whereas the final crack length is considered to be the half plate thickness [24]. For the concave fillet weld geometry, disregarding the nucleation stage at the weld toe is not appropriate as the crack initiation life from the weld toe surface is significant.

At the weld toes of concave fillet welds, the fatigue phenomenon at the initiation stage is specified by a significant local stress. A very important step of fatigue strength evaluations at the notch of the concave fillet weld is the determination of the fatigue notch factor, $K_f = \sigma_{\text{smooth}} / \sigma_{\text{notch}}$ (σ_{smooth} and σ_{notch} are the fatigue strengths of smooth and notch members, respectively). This factor can be determined by the concept of stress concentration factor (SCF), $K_t = \sigma_{\max} / \sigma_n$ ($\sigma_{\max}$ and σ_n are the maximum stress at the notch and nominal stress, respectively) [118-120]. With no yielding at the hotspot of a weld toe, K_f can approximately equal K_t [119]. Fatigue crack initiation at the

weld toe correlates with surface roughness and residual stresses field at the weld toe of the concave fillet weld.

2.5.3 Fatigue crack propagation at the weld root

The stress at the weld root can be simply calculated on the plate section or it can be resolved on the weld throat section [110, 111]. Any variation in the structural details such as the plate thickness, weld penetration depth, and weld leg length induces an increase in the scatter when the nominal stress range on the plate section is used. In the N-SIF approach, the scatter band of weld root failures may decrease. Based on a thorough search of the relevant literature, it was concluded that this application of the N-SIF approach has not been conducted thoroughly for the weld root under three-point bending.

The SIF at the weld root crack tip is required in the N-SIF and crack propagation approaches. The weld root SIF results for load-carrying cruciform fillet welded joint in the literature are limited to the geometry of the flat face fillet weld, and the loading conditions of tension (Figure 2.7a) and pure bending (Figure 2.7b) [71, 121-123]. However, the SIF values at the weld root crack tip for load-carrying cruciform joint with concave fillet weld under three-point bending load have not yet been studied. What is not yet clear is the impact of weld toe geometry and importantly three-point loading on the SIF calculation at the weld root crack tip. The complex geometry and bending-type load lead to shear and normal stress fields at the weld root crack tip resulting in a mixed-mode problem.

According to the IIW guideline for the assessment of weld root fatigue [24], the crack propagation approach is well suited for weld root long crack in LEFM. In addition, this fatigue assessment of a component is applicable when crack initiation life is negligible.

2.5.4 Conclusion on fatigue of cruciform joint

Investigations concerning the fatigue life of cruciform joint weldments are sparse. The research to date on fatigue life of cruciform joints has often tended to focus on the conditions of non-load-carrying and load-carrying cruciform fillet welded joints. The geometry of load-carrying cruciform

joint has been particularly limited to flat face fillet welded joints (Figure 2.7a and b) and few studies have explored the cruciform joint with concave fillet weld (Figure 2.7c). In addition, little attention has been paid to the pure bending loads (Figure 2.7b) in comparison to tension load (Figure 2.7a). Thus far, there has been no study focusing on three-point bending (Figure 2.7c). Although considerable amount of research work has been carried out on the potential of weld toe failure in the CJP and PJP fillet welds, there are still scarce research on the weld root failure of PJP fillet weld. Up to the present, there has been little discussion about fatigue crack propagation at the weld root under tension fatigue load, and no research has yet linked the FCG behavior of CT specimen to that of the weld root in cruciform joint under bending load.

A thorough search of the relevant literature showed that fatigue crack propagation and fatigue life analysis of partially penetrated load-carrying cruciform joints with concave fillet weld under fatigue three-point bending load has not yet been studied (Figure 2.7c). This indicates a need to understand the various fatigue phenomena that exist for this geometry and loading condition.

CHAPTER 3 METHODOLOGY OF STUDY

3.1 Materials and cruciform welded specimens

Welded joints of thick blades and the band/crown in the Francis turbine runners (or the hub in the propeller runners) can be deemed representative of the joints of load-carrying cruciform fillet welds with certain simplified considerations. The partially penetrated welded joint is designed under constraints that are necessary to reproduce realistic conditions in turbine runners. As the structure size grows, the stress triaxiality will go up, which can increase the stress levels in the structure [124]. Therefore, the thickness of laboratory specimens ought to be selected as large as possible to represent similar thick welded joints in the turbine runners. A schematic model of the proposed specimen is shown in Figure 3.1. It is developed to characterize the weld toe and root fatigue lives; this feature therefore makes it an ideal specimen for studying the influence of weld penetration depth as well as the weld metal on fatigue behavior.

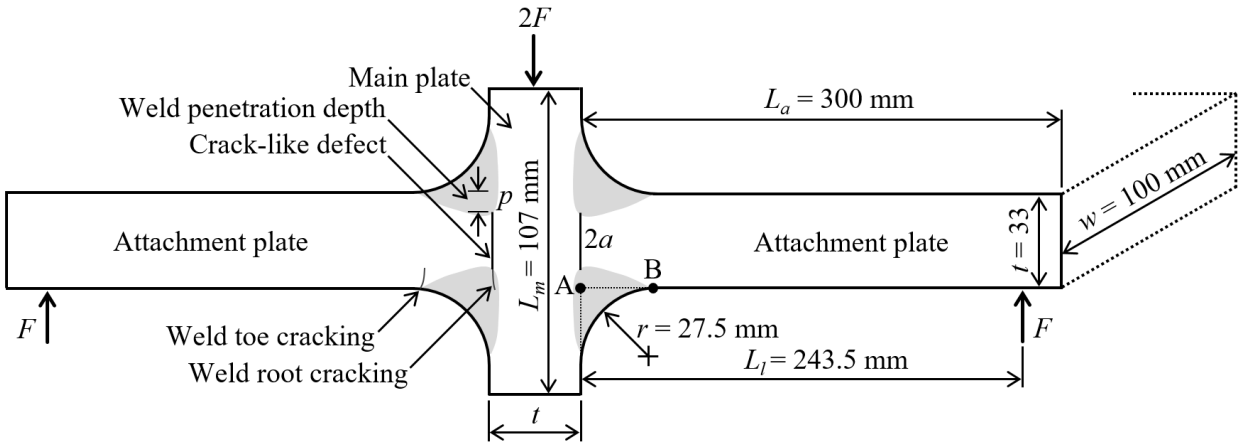

Figure 3.1: Schematic model of proposed cruciform fillet welded specimen under three-point bending

3.1.1 Material properties

The base metal is a wrought martensitic stainless steel AISI 415 (UNS S41500 or 13%Cr–4%Ni) [58]. CA6NM [57], commonly used in the fabrication of turbine runners, is the cast version of AISI 415. Owing to less dispersion in the results, AISI 415 is chosen instead of CA6NM. Nominal and measured chemical compositions and mechanical properties of the base metal are listed in Tables 3.1 and 3.2, respectively.

Table 3.1: Nominal and measured chemical compositions (wt.%) of base metal and welding electrodes

Classification	C	Cr	Ni	Mo	Mn	Si	P	S	N	Cu
AISI 415 (ASTM A240M)	<0.05	11.5–14.0	3.5–5.5	0.50–1.00	0.50–1.00	<0.60	<0.030	<0.030	-	-
AISI 415 (Manufacturer)	0.02	12.8	4.0	0.54	0.62	0.35	0.018	0.001	0.030	-
E410NiMo (AWS A5.22M)	<0.06	11.0–12.5	4.0–5.0	0.40–0.70	<1.0	<1.0	<0.04	<0.03	-	<0.75
E410NiMo [125]	0.02	11.6	4.5	0.53	0.4	0.4	0.01	0.01	0.003	0.01
E316L (AWS A5.22M)	<0.04	17.0–20.0	11.0–14.0	2.0–3.0	0.5–2.5	<1.0	<0.04	<0.03	-	<0.75
E316L (Manufacturer)	0.03	18.9	12.0	2.9	1.3	0.9	0.02	0.01	-	0.01

Two weld metals, martensitic and austenitic stainless steels, are used in this research. The former weld metal, which has a good weldability and a chemical composition matching to that of the base metal, is a E410NiMo (UNS W41036 or NiMo 0.02%C) steel [59]; it is used to reduce the detrimental microstructural changes induced by the welding process. Post-weld heat treatment (PWHT) as proposed by the American Welding Society (AWS) [59] indicates heating the specimen between 595 °C and 620 °C, holding for 1 h (−0, +15 minutes), and then air cooling it to ambient temperature. The austenitic filler metal E316L [59] is used because it requires no preheating, and no PWHT is proposed by the AWS. During their lifetime, turbine runners may undergo in situ repairs using welding materials that cannot be heat-treated. Thus, austenitic filler is appropriate.

The nominal and measured chemical compositions of the welding electrodes and the nominal and measured mechanical properties of the weld metals are given in Tables 3.1 and 3.2, respectively.

Table 3.2: Nominal and measured mechanical properties of base and weld metals

Classification	0.2% yield strength (MPa)	Tensile strength (MPa)	Elongation at rupture	Brinell Hardness (HBW)
AISI 415 (ASTM A240M)	>620	>795	>0.15	<302
AISI 415 (Manufacturer)	754±11	841±10	0.22±0.01	252±3
E410NiMo-HT (AWS A5.22M)	-	>760	>0.15	-
E410NiMo-AW [126]	783±6	1007±10	0.11±0.01	-
E410NiMo-HT [126]	765±5	895±4	0.152±0.004	-
E316L (AWS A5.22M)	-	>485	>0.3	-
E316L (Manufacturer)	395	550	0.50	-

Note: AW and HT correspond to as-welded and heat-treated, respectively.

3.1.2 Design of cruciform joints

The geometric parameters of load-carrying cruciform fillet welded joints were limited to the capacities of the available fatigue testing machine and flexure fixture in this study. The main plate and the attachment plate thicknesses were chosen according to the maximum nominal width of the flexure fixture and the plane strain condition [127]. Maximum specimen span distance was limited to the flexure fixture span length, and the extended length of the attachment plates was considered for supporting the deflection of the specimen. Maximum specimen deflection was calculated by using the classical beam theory to satisfy the testing machine displacement range. The geometry of a specimen and the loading locations on the attachment plates from the main plate L_l are

illustrated in Figure 3.1. The weld root crack length (unfused section length) $2a$ is characterized by the dimensionless parameter of the crack length over the thickness, $2a/t$.

To meet the objectives of this study (Section 1.3), four different test types are devised (Table 3.3). T1, T2, and T3 can potentially show the effect of weld penetration depth, and T4 can show the effect of the first weld pass material on fatigue strength. T1 and T2 present partial joint penetration (PJP) with $2a/t = 1/3$ and 2/3, respectively. There is no joint penetration for T3 and T4, meaning that the unwelded section embedded between the main and the attachment plates has the same length equal to the attachment plate thickness $(2a/t = 3/3)$. The first welding pass material was E410NiMo for T1, T2, and T3, and E316L for T4, whereas only weld metal E410NiMo was used to fill the weld toes after the first weld pass deposition.

Table 3.3: Four proposed test types

Specimen type	$2a/t$	First pass filler material
T1	1/3	E410NiMo
T2	2/3	E410NiMo
T3	3/3	E410NiMo
T4	3/3	E316L

3.1.3 Fabrication of weldments

Plates of AISI 415 were prepared following a freehand plasma cutting of the original thick rolled block, and portions affected by plasma cutting heat were sawed off, and the remaining material was machined to its final dimensions. The weld penetration depth was controlled by providing an appropriate root face on the attachment plates. Plates were aligned and attached to each other in a cruciform position using tack welding. To prevent the start and end effects of the welding process [128, 129], two auxiliary appendix joints were tack welded to the plate assembly; hence, welding was started from and ended on the auxiliary appendix joints. Plates were fixed to decrease plate

distortion and warpage during the welding process of the joints by welding two rigid stiffeners to the plate assembly. Rigid frames clamped together the main and the attachment plates. The plate assembly was then installed on the welding jig. The plate assembly with auxiliary appendices and stiffeners installed on the welding jig is shown in Figure 3.2.

Figure 3.2: Plate assembly with auxiliary appendices and stiffeners installed on the welding jig. A Scompi robotic welding machine [130] is located next to the welding jig

A fully automated flux-cored arc welding (FCAW) machine was used to perform weld depositions on the welded joints of the plate assembly. To achieve a reproducible welding condition, a Scompi® robot, developed at Hydro-Quebec Research Institute [130], was used to weld the joints of the plates; the torch of the FCAW machine was fixed on the robotic arm. Figure 3.2 demonstrates the initial position of the Scompi and welding gun of the FCAW machine fixed on the robotic arm. The welding parameters for two weld metals are given in Table 3.4. For weld metal E410NiMo, a preheating treatment at 100 °C decreases the cooling rate in the weld metal and the heat-affected zone (HAZ) to produce a more ductile metallurgical structure with a resistance to hydrogen

cracking and also reduces the shrinkage stresses [131]. Note that austenitic stainless steel E316L was used because it does not require a preheating step [59].

Table 3.4: Welding parameters for two weld metals used by the FCAW machine

Welding electrode	Preheat temp. (°C)	Interpass temp. (°C)	Voltage (V)	Current (A)	Torch speed (mm/s)	Heat input (J/mm)	Filler deposit rate (kg/h)	Welding position	Shielding gas
E410NiMo	>100	<200	26.8	260	7.5	929	5.0	2F (Pass 1 to 4) 1F (Pass 5 to end)	Argon-25% CO2
E316L	<50	n/a	27.4	215	7.5	785	5.0	2F (Pass 1)	Argon-25% CO2

A number of passes (15, 14, 12, and 12) were applied to the fillet welds of T1, T2, T3, and T4, respectively. Extra weld pass depositions were carried out to ensure sufficient material was available for weld toe grinding. Manual burr-grinding followed by polishing were then performed to round the corners at the weld toes. The final radius at each weld toe measured 27.5 ± 0.3 mm. Surface roughness at the weld toes was measured parallel to the main plate, and the roughness average value R_a was between 1 and 3 μm.

The weld beads were quality-checked by visual inspection, magnetic particle examination, liquid penetrant test, and ultrasonic examination [132, 133]. Only acceptable welded assemblies passed to the next stage of specimen preparation. To perform PWHT, the welded assemblies were slowly heated to 595 °C, held for 5 h, and then slowly air-cooled to the ambient temperature [59]. The temperature contrast between different points of the welded assemblies varied between 595 °C and 598 °C. Following PWHT, maximum tensile residual stresses were reduced by almost 70% in the hotspot of a multi-pass T-joint [128] and 75% in a five-bead V-type welded specimen [134]. Each welded assembly was eventually cut lengthwise and machined into several welded specimens of 100 mm or 35 mm width. Figure 3.1 schematically shows the cruciform joint layout. After fabrication, the weld root crack length *a* and weld penetration depth *p* were measured for different test types. The averages values are presented in Table 3.5.

Table 3.5: Weld root crack length and weld penetration depth for four test types

Specimen type	Weld root crack length, a (mm)	Weld penetration depth, p (mm)
T1	7	9.5
T2	12	4.5
T3	16	0.5
T4	16	0.5

3.2 Experimental procedure

3.2.1 Bending setup

The tests were performed using a 250-kN MTS® servo-hydraulic machine and a 250-kN Instron® flexure fixture (three-point bending fixture). The fixture was mounted and then leveled on the servo-hydraulic machine. Two shelves parallel to the flexure fixture were fixed on the two columns of the servo-hydraulic machine. Traveling microscopes (with a precision of 10 μm) were positioned on each shelf and leveled. They were used with cold light sources to detect crack initiation and propagation at each weld toe and root under tension. The welded specimen was installed on the flexure fixture and its deflection during the monotonous bending tests was measured by the combination of a plunger and extensometer. Different components of the bending setup and the welded specimen installed on the bending fixture are shown and highlighted in Figure 3.3.

3.2.2 Monotonous bending tests

To define the maximum load before plastic deformation for the fatigue testing, monotonous bending tests at ambient temperature were performed on two welded specimens of 35 mm width. The tests were conducted on welded specimens of T2 and T3 to detect the effect of different weld penetration depths, if any. The graphs of three-point bending load F versus maximum specimen deflection $z_{\max}$ is presented in Figure 3.4.

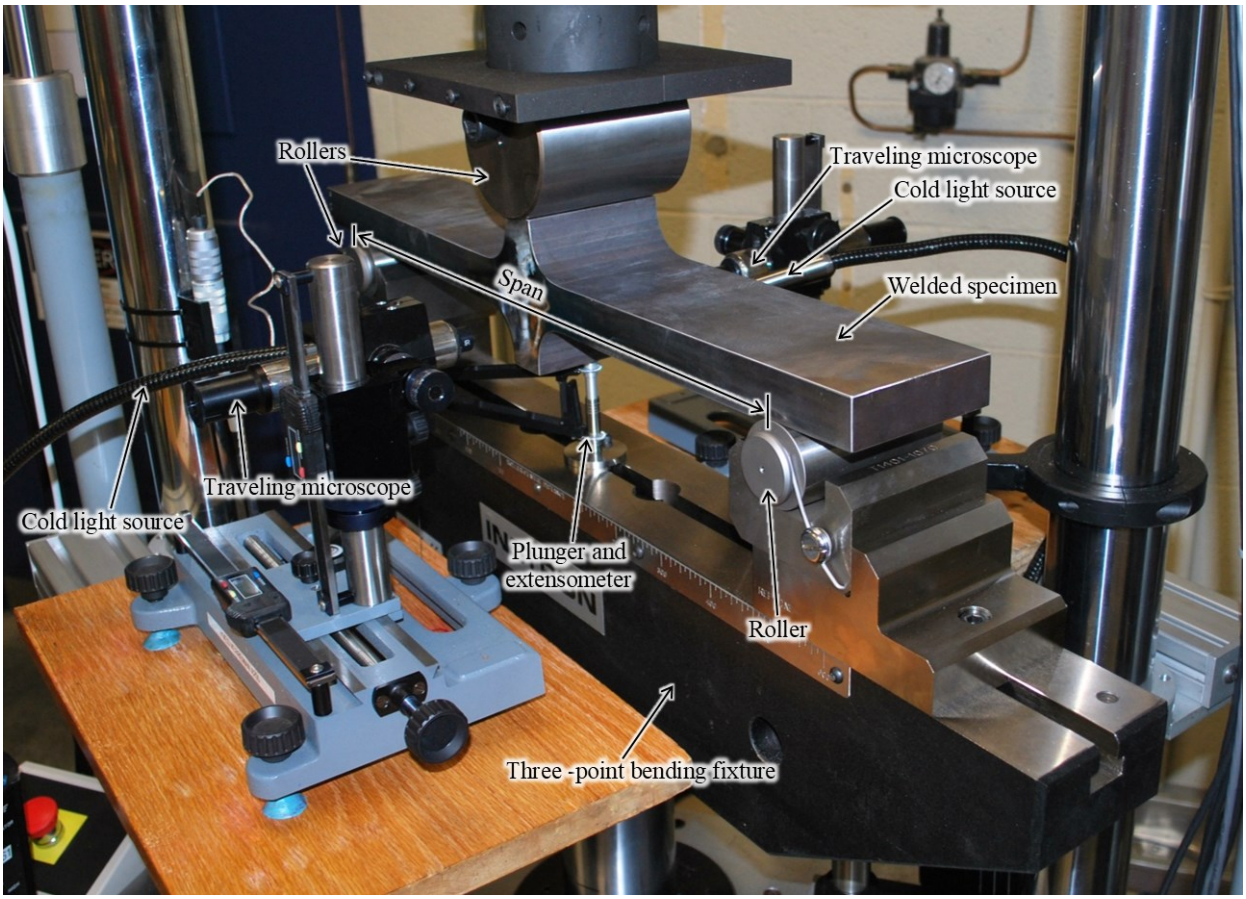

Figure 3.3: Experimental setup and welded specimen installed on the bending fixture

The corresponding nominal bending stress at point A (Figure 3.1) is presented on the primary vertical axis and is calculated based on the classical beam theory as:

$$\sigma_n = \frac{6FL_l}{wt^2} \tag{3.1}$$

where L_l is the applied load location on the attachment plate; w and t are the width and the thickness of the attachment plates, respectively.

Determining the yield strength based on the offset method is not feasible when the corresponding strain data are not available. Thus, the proportional limit—the highest point attained before the line begins to curve—was initially well defined in the bending load–deflection curves. The corresponding nominal bending stresses of proportional limit at the weld root (point A in

Figure 3.1) and at the weld toe (point B in Figure 3.1) were calculated as 821 MPa and 728 MPa, respectively. The yield strengths (measured by the tension tests) of the base metal AISI 415 and the weld metal E410NiMo (Table 3.2) are comparable to the nominal bending stress of proportional limit at the weld toe (point B in Figure 3.1).

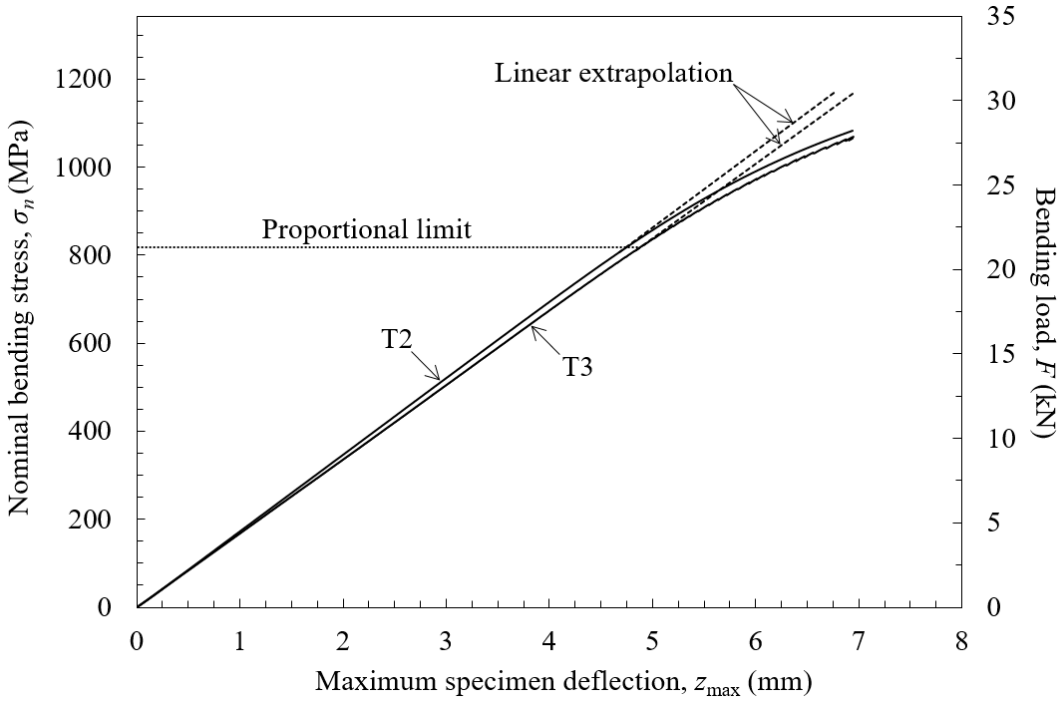

Figure 3.4: Bending load and nominal bending stress (at point A in Figure 3.1) versus maximum specimen deflection for T2 and T3

3.2.3 Fatigue testing

The experimental fatigue tests were performed at constant amplitude load. The loading waveform was sinusoidal and its frequency ranged from 1 to 16 Hz. Table 3.6 lists the applied stress levels and frequencies of the fatigue test. The maximum nominal bending stress σ_{max} calculated at the weld root varied between 28% and 95% of the proportional limit (821 MPa). The nominal bending stress range $\Delta\sigma_n$ was calculated at a load ratio R of 0.1. The nominal bending stress range at the proportional limit $\Delta\sigma_{n,\,PL}$ is equal to 739 MPa.

Table 3.6: Applied stress levels and frequencies

Maximum nominal bending stress, σ_{max} (MPa)	230	250	270	330	420	510	600	690	780
Proportional limit percentage (%)	28	30.5	33	40	51	62	73	84	95
Nominal bending stress range, $\Delta\sigma_n$ (MPa)	207	225	243	297	378	459	540	621	702
Frequency (Hz)	15–16	12–14	10–12	9–10	8–9	7–8	6–7	5–6	1–5

All tests were conducted at ambient temperature. Prior to performing the tests, the lateral surfaces were polished to obtain a mirror-like finish to facilitate the detection of weld toe and root cracks. Because of the complex and time-consuming fabrication processes of welded specimens, one specimen was tested for each fatigue bending stress range.

3.3 Crack propagation at the weld roots

There are two crack-like defects at the weld roots with the same initial crack length a_i. Thus, the cracks can propagate simultaneously or not. The first scenario is to have a symmetrical crack propagation at the weld roots as depicted in Figure 3.5a. The secondary crack a_s therefore propagates simultaneously with the leading crack a_l $(a_i < a_s = a_l)$. The second scenario is to have a dissymmetrical crack propagation at the weld root as presented in Figure 3.5b. In this condition, only the leading crack a_l propagates at one weld root $(a_i = a_s < a_l)$. The crack propagation from crack-like defects at the weld roots can also occur anywhere between these two scenarios $(a_i < a_s < a_l)$.

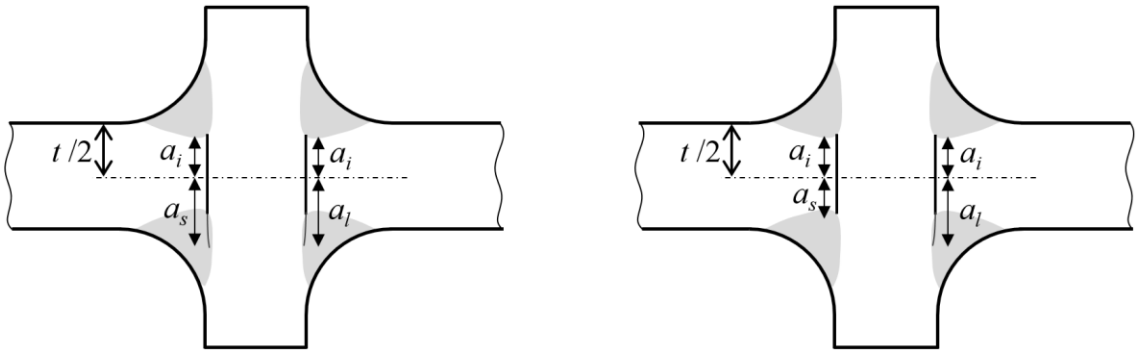

(a) (b)

Figure 3.5: (a) Symmetrical crack propagation and (b) dissymmetrical crack propagation

3.4 Numerical methodology for SIF calculation

For a complex crack geometry in a load-carrying cruciform joint with a concave fillet weld under three-point bending load, the SIF solution has not been established. Therefore, numerical methods are used to calculate the SIF at the weld root crack tip. To validate the results, a numerical study of the parameters influencing the accuracy of the computed SIF values is carried out for typical crack geometry of a center crack under tension load. The numerical results are compared with the analytical solution reported by Isida [72], and some recommendations to increase the accuracy of calculated mode I SIFs are given. The assessment of mode I and mode II SIFs at the weld root crack tip of a load-carrying cruciform fillet welded joint loaded under three-point bending is then carried out following the recommendations.

3.4.1 Center crack

A 2D plane strain model of a center crack under tension loading was generated to analyze the numerical values of K_I. Symmetric boundary conditions were applied on the normal plane and on the plane of crack propagation; therefore, one-quarter geometry (Figure 3.6) was used in the finite element analysis (FEA). The specimen geometry is characterized by a dimensionless parameter $h/b,$ and the crack length is quantified by the dimensionless parameter $\alpha = a/b,$ in which h and

b are the half specimen height and width, respectively, and a is the crack length. Geometric parameters b and h were given values of 40 mm and 60 mm $(h/b=1.5)$, respectively, with the crack length dimensionless parameter $a/b=0.5$. For fully linear elastic behavior, the elastic modulus E and Poisson's ratio ν of the material were taken as 200 GPa and 0.3, respectively. The model was subjected to a uniform tensile stress σ of 100 MPa.

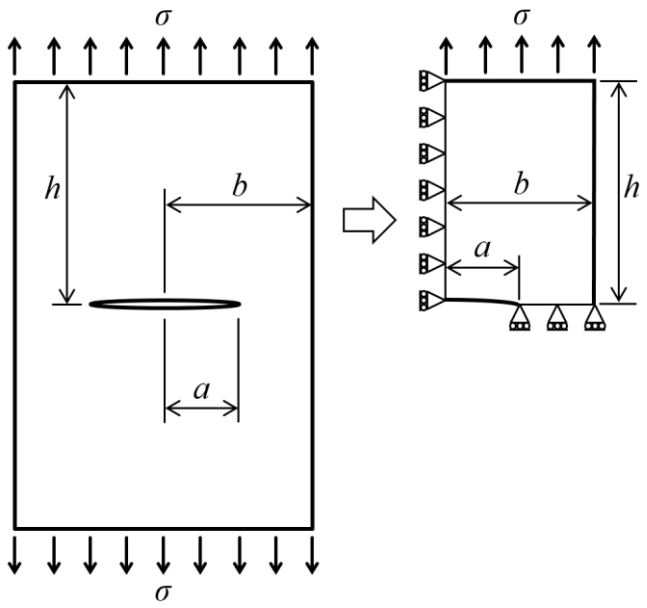

Figure 3.6: 2D schematic model of the full and one-quarter geometries of the center crack

The mode I SIF from the analytical solution reported by Isida [72] for a typical through-thickness center crack in a finite width sheet is considered. The geometry factor Y presented by Isida is exact to four significant digits for $h/b=1.5$ and $a/b=0.5$. For each studied variable, the numerical results were compared with those calculated by Isida. The percent difference e_K was defined as follows:

$$e_K(\%)=\frac{K_{I(\mathrm{FEM})}-K_{I(\mathrm{Isida})}}{K_{I(\mathrm{Isida})}}\times 100 \tag{3.2}$$

where $K_{I(\mathrm{FEM})}$ is the SIF calculated using the finite element method (FEM). It is important to note that the term "exact estimation" for the K value refers to the range $-0.01\% < e_K < +0.01\%$. To investigate the influence of different parameters using FEM, several models and calculations (more than 520) were undertaken.

Influencing parameters

Numerical K-solution methods

Two different methods were used to calculate the SIFs: (i) the displacement extrapolation method (DEM) and (ii) the interaction integral method (IIM). The former was evaluated over the nodes associated with the crack face of the first row. The convergence of the latter method was evaluated over four integral paths adjacent to the first row at the crack tip to ensure effective validation of the K values. For the center crack, only the existence of mode I is considered.

Types of quadratic elements

The recommended quadratic element type in ANSYS® is used for a 2D model [96]. Triangular quarter-point elements were used at the crack tip, as suggested by Barsoum [76], while regular 6-node triangle or 8-node quadrilateral elements were adopted for the remainder of the finite element model, as shown in Figure 3.7.

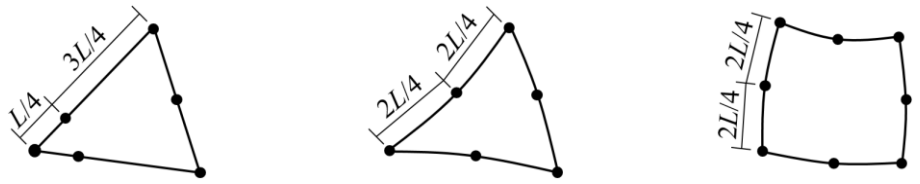

(a) (b) (c)

Figure 3.7: Different quadratic element types: (a) triangular quarter-point, (b) 6-node triangle, and (c) 8-node quadrilateral; L is the size of the element side connected to the crack tip in (a), while it represents the element size in (b) and (c)

Angular discretization around the crack tip and finite element size

The number of elements (n) in the circumferential direction at the crack tip can be varied. The influence of using $n = 2–18$ elements in 180° was investigated. The arrows in Figure 3.8 indicate the crack tip locations for angular discretizations of 2, 3, 5, 6, and 12 elements.

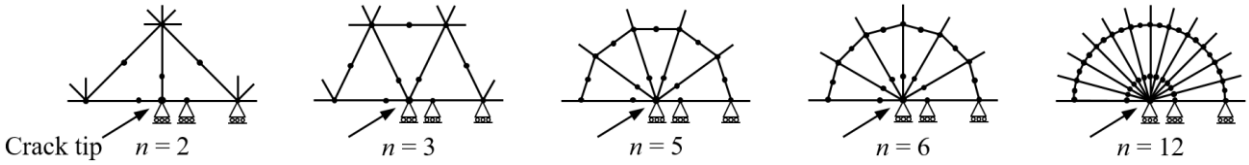

Figure 3.8: Different angular discretizations around the crack tip

To investigate the influence of angular discretization, element sizes in the body L_B and around the crack tip L_T were considered to be the same (uniform mesh). This influence was investigated by testing models with element sizes ranging from $a/3$ to $a/50$.

Local mesh refinement

A fine mesh in the vicinity of the crack tip is necessary to capture the variation in the strain and stress fields. Therefore, a parameter defined as the ratio of the body element size to the crack tip element size (mesh size ratio), L_B / L_T, was investigated as a local mesh refinement parameter. Some typical mesh patterns are illustrated in Figure 3.9.

Poisson's ratio

The Poisson's ratio of the material was varied between 0 and 0.48, and its influence on the SIF was explored.

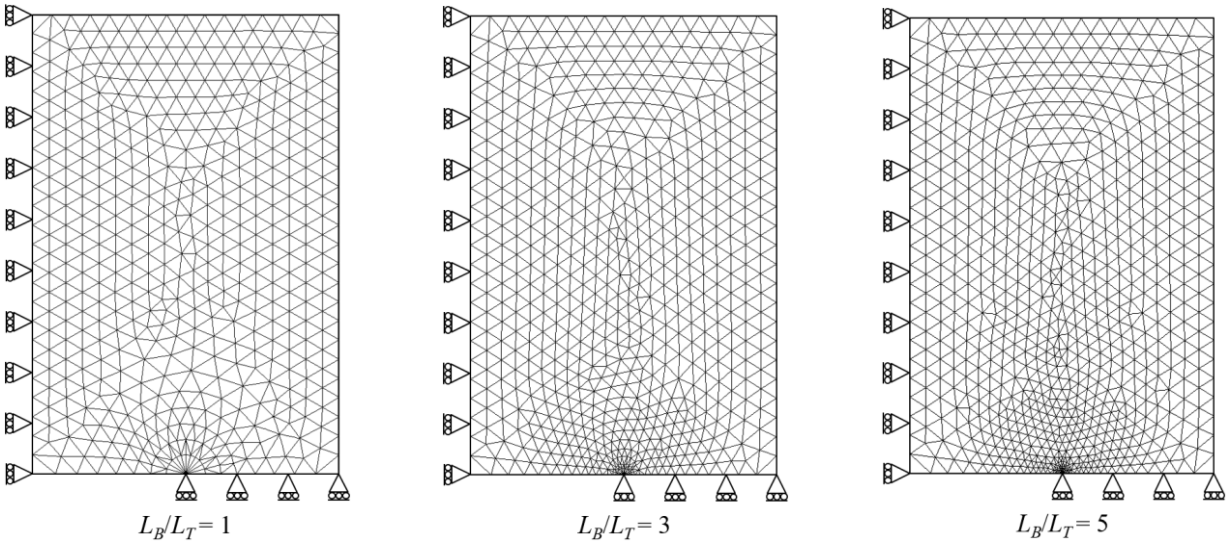

Figure 3.9: 2D finite element mesh patterns of a center crack for $a/b = 0.5$, $n = 12$, and $L_B = a/8$

Crack length

Different crack lengths were considered by changing the dimensionless parameter for the crack length a/b from 0.1 to 0.6 at intervals of 0.1.

3.4.2 Load-carrying cruciform joint

The SIF for a load-carrying cruciform joint with a concave fillet weld under three-point bending was calculated for the weld root crack tip. The weld toes are rounded, as shown in Figure 3.10. The complex geometry and bending-type load produce shear and normal stress fields at the weld root crack tip; therefore this analysis is a mixed-mode problem. DEM and IIM were employed to calculate the mode I and mode II SIFs. The convergence of the IIM was evaluated over three integral paths adjacent to the first row of singular elements at the crack tip. Only a limited number of weld root SIF results obtained with numerical methods are available for a load-carrying cruciform joint with a flat face fillet weld under tension and pure bending [71, 121-123].

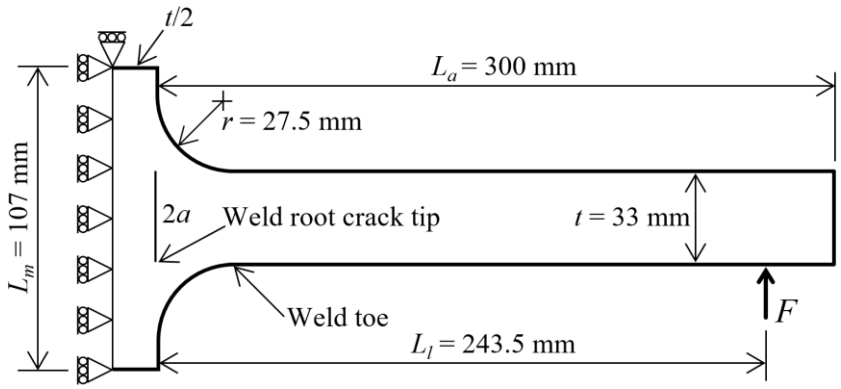

Figure 3.10: 2D symmetry model of a load-carrying cruciform fillet welded joint loaded under three-point bending

The plane strain condition in the 2D symmetry model was analyzed in this study. The geometry of the cruciform joint and its symmetry and loading conditions are shown in Figure 3.10. The weld root crack length is characterized by a dimensionless parameter, $2a/t$ (t is the plate thickness). For fully linear elastic behavior, the elastic modulus E and Poisson's ratio ν were taken as 200 GPa and 0.3, respectively. The model was subjected to a three-point bending load F with a corresponding nominal bending stress at the weld root of 100 MPa. Triangle quarter-point elements were used at the crack tip, while 6-node triangle elements were adopted for the rest of the finite element model. The mesh patterns for two crack lengths, $2a/t = 6/9$ and $9/9$, are shown in Figure 3.11. The mesh distributions for different crack lengths were identical within the crack tip box.

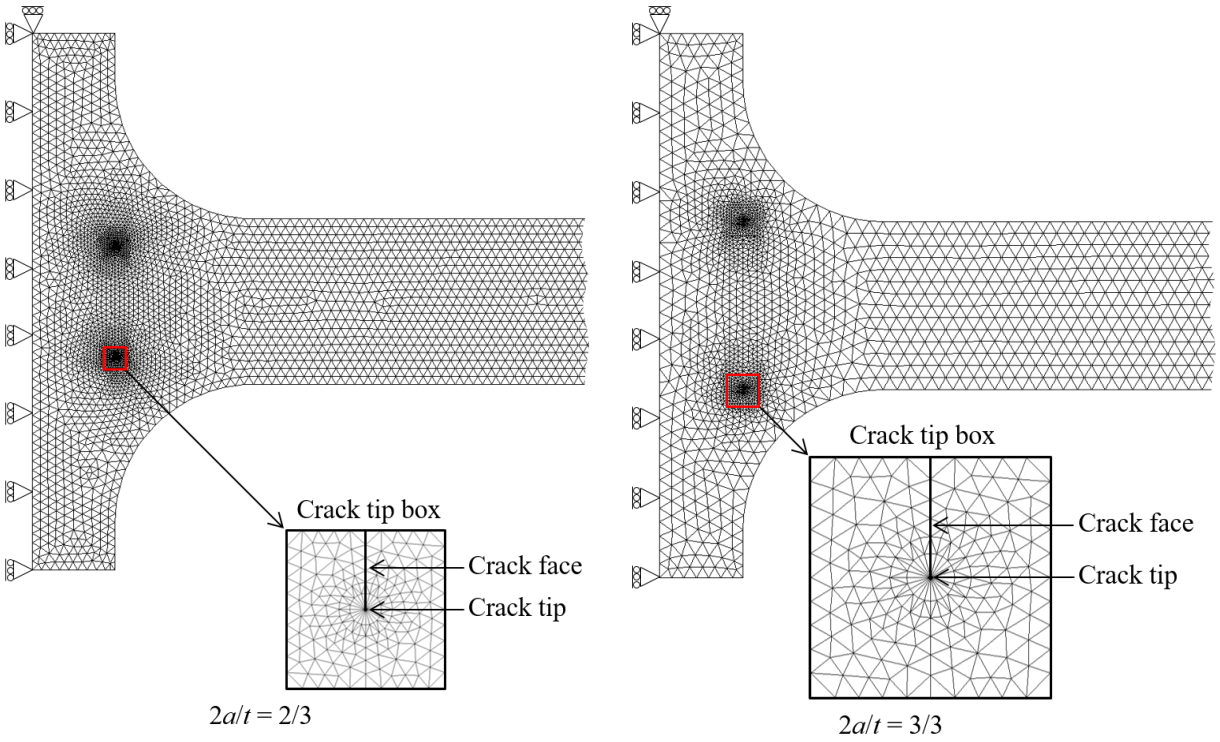

Figure 3.11: Two mesh patterns of the cruciform joint for $n = 12$ in 180°, $a / L_B = 6$, and $L_B / L_T = 5$

CHAPTER 4 EXPERIMENTAL RESULTS

4.1 Fatigue *S–N* data

The nominal bending stress range at point A (Figure 3.1) is employed to analyze the fatigue test data. In Figure 4.1, the scatter plot of fatigue test results and the mean curves, determined by the least squares method (linear regression), are shown for all test types in a log–log scale. The range of fatigue lives spans a low cycle fatigue (LCF) of 3.32×10^4 cycles and a high cycle fatigue (HCF) of 8.34×10^6 cycles.

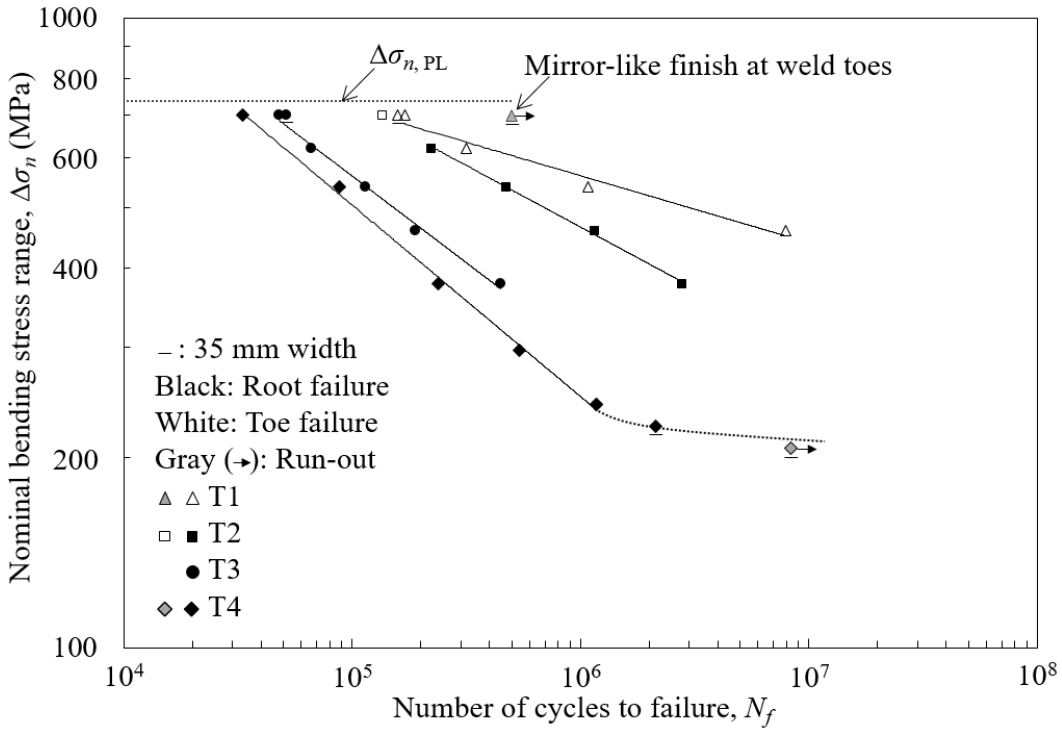

Figure 4.1: *S–N* curve of different test types

All T1 specimens failed at the weld toe. Figure 4.2 outlines the fracture surface of the weld toe failure of T1. A semi-elliptical crack is observed at the crack front of the fatigue fracture surface. At stress ranges of 459 and 540 MPa, no cracks were initiated at the weld roots, but for higher stress ranges, small cracks were observed at the weld roots.

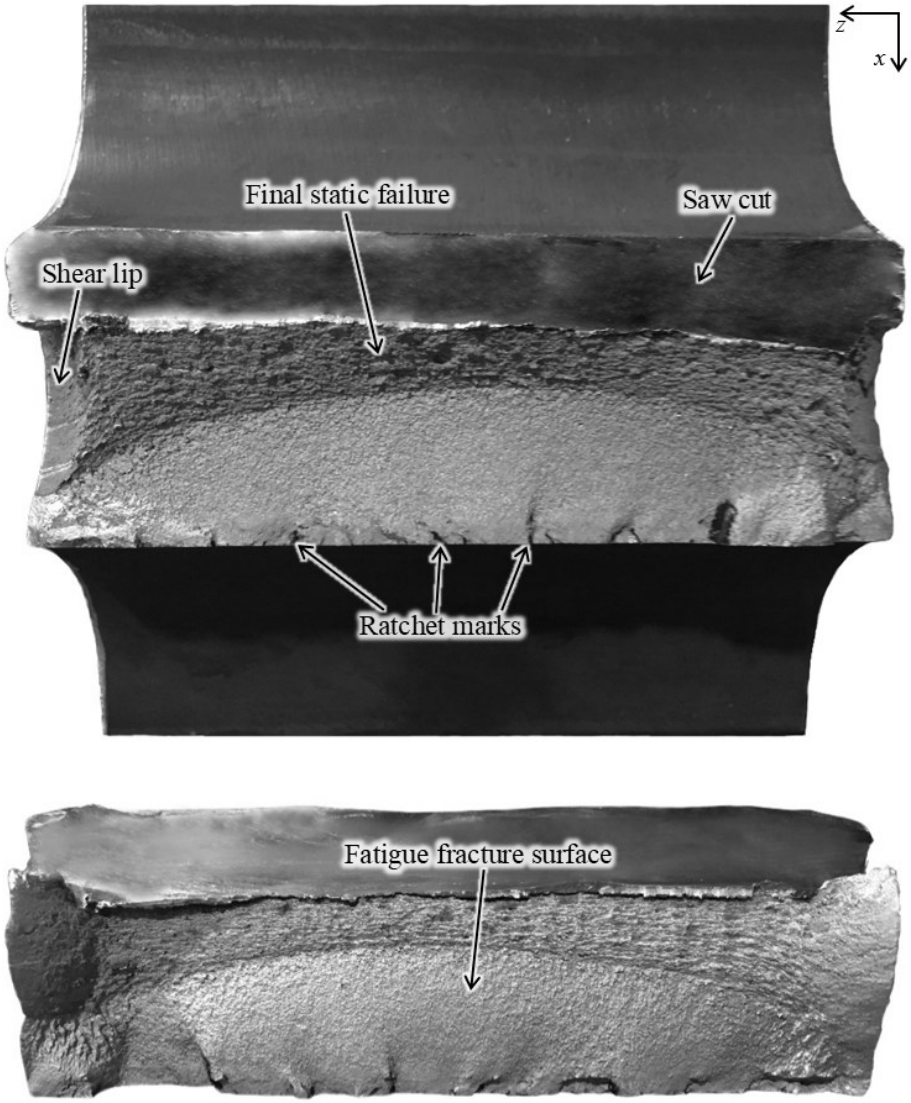

Figure 4.2: Welded joint of T1 after final failure at the weld toe

T2 specimens failed at the weld root except at the highest stress ranges. Figure 4.3 shows the fracture surface of the weld root failure of T2. At $\Delta\sigma_n = 621$ MPa, a crack length of 4.15 mm was observed at the lateral surface of weld toe, although the final fatigue failure occurred at the weld root (Figure 4.4a). The leading crack at the highest stress range of 702 MPa occurred at the weld toe and its fatigue failure therefore prevailed (Figure 4.4b).

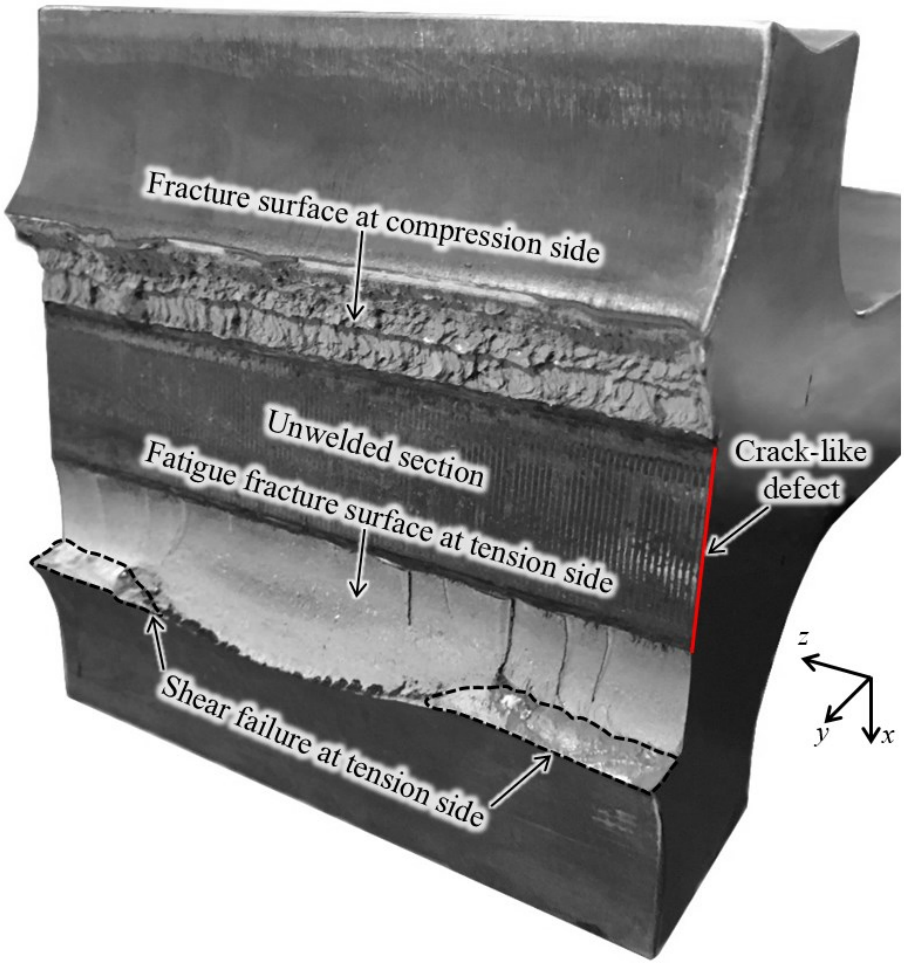

Figure 4.3: Welded joint of T2 after final failure at the weld root

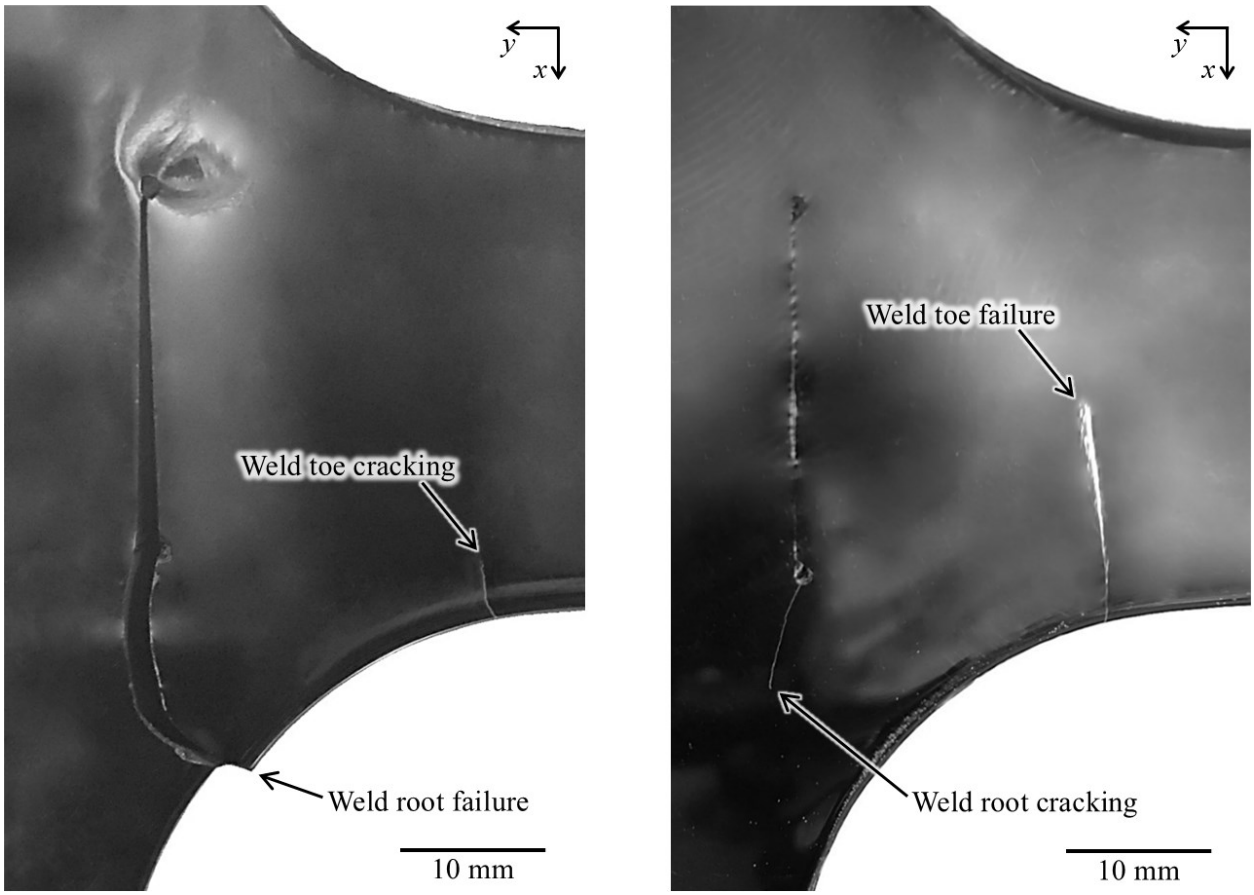

Figure 4.4: Fatigue failure mode transition observed for T2: (a) final fatigue failure at the weld root crack and (b) final fatigue failure at the weld toe crack

T3 and T4 failed at the weld roots (except the run-out at $\Delta\sigma_n = 207$ MPa for T4). T3 presents higher fatigue strength compared to T4; the difference is between 23% and 47% of fatigue lives in the stress range 378 to 702 MPa. The only parameter responsible for this effect is the first-pass weld metal. Hence, most of the fatigue lives at the weld root are spent in the first millimeter of a crack propagation. Figure 4.5 presents the fracture surface of the weld root failure of T3.

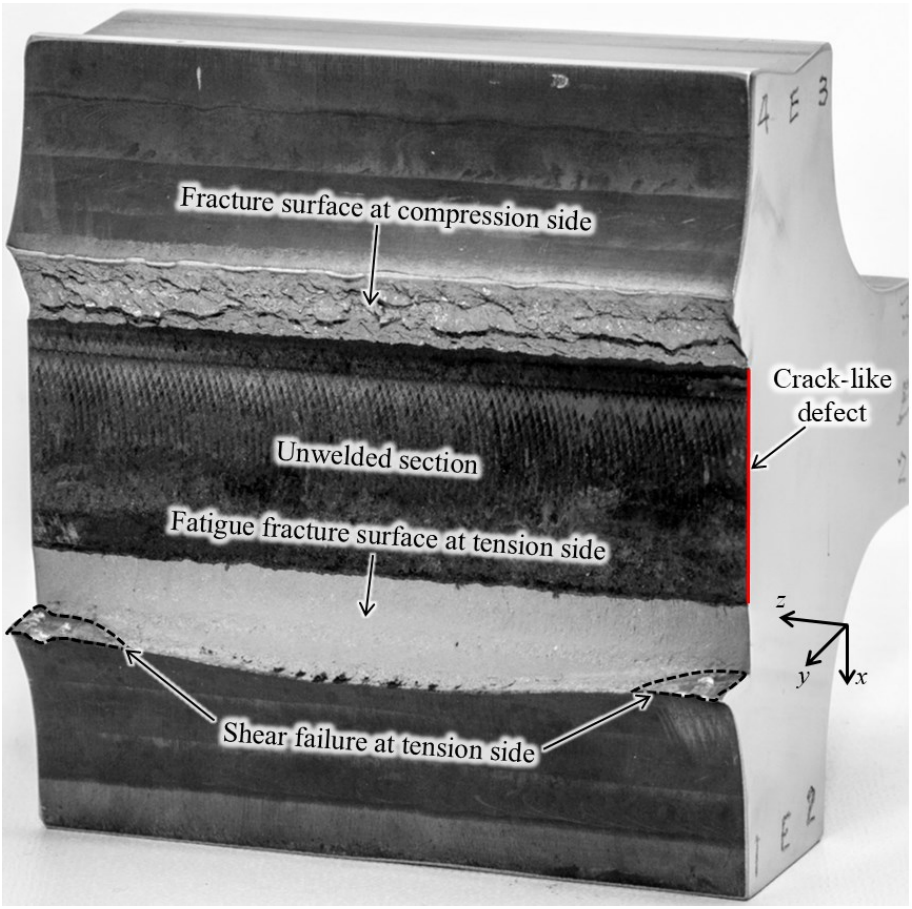

Figure 4.5: Welded joint of T3 after final failure at the weld root

The scatter plot of fatigue test results for each test type exhibits a higher linear correlation in the log–log scale with the exception at lower stress ranges for T4, where the data follow a nonlinear regression pattern to become gradually horizontal in the HCF. For T1 and T3, specimen widths of 35 mm $(w/t = 1.06)$ and 100 mm $(w/t = 3.03)$ do not show a considerable difference in fatigue lives at $\Delta\sigma_n = 702$ MPa.

Initial crack length a_i and final leading crack length a_f at the weld root, and number of cycles to failure N_f are listed in Table 4.1 for T2 and T3. At $\Delta\sigma_n = 540$ MPa of T3, beach marking technique was used in order to visualize fatigue crack propagating at the crack front of the weld root. More detail is given in Section 4.3.

Table 4.1: Initial crack length a_i, final leading crack length a_f, and number of cycles to failure N_f at different stress ranges for T2 and T3

$\Delta\sigma_n$ (MPa)	T2			T3		
	a_i (mm)	a_f (mm)	N_f (cycles)	a_i (mm)	a_f (mm)	N_f (cycles)
378	12	23.07	2785762	16	24.52	448966
459	12	20.60	1146808	16	22.62	188724
540	12	24.86	470463	16	23.82	114265
621	12	25.05	222607	16	24.62	66377
702	12	*	135830	16	23.35	47812

* There was fatigue failure at the weld toe.

4.2 Crack initiation at the weld toe and root

The number of cycles corresponding to a crack initiation length less than 150 μm, either at the weld toe or at the weld root, was defined as the crack initiation life N_i [113, 135]. At the lateral surfaces, weld toes and roots of each welded specimen therefore were inspected frequently utilizing traveling microscopes capable of detecting the crack initiation.

Crack initiation life was recorded for one failed specimen at the weld toe of T1. At $\Delta\sigma_n = 621$ MPa, the fatigue life ratio of crack initiation N_i / N_f was equal to 98%. To evaluate the influence of weld toe surface roughness on the fatigue life, the weld toe surfaces of one T1 specimen were polished to a mirror-like finish. Consequently, a significantly longer weld toe fatigue life was observed at $\Delta\sigma_n = 702$ MPa (Figure 4.1). Thus, most of the fatigue life was expended in the initiation of a crack at the weld toe.

In Table 4.2, the fatigue life ratio of crack initiation N_i / N_f is listed at the weld root for T2, T3, and T4. The fatigue life ratio of crack initiation at the weld root is less than 9%. Therefore, the gap-tip at the weld root is significant enough to be considered as a crack-like defect.

Table 4.2: Fatigue life ratio of crack initiation at the weld root for each test type

Specimen type	Stress range $\Delta\sigma_n$(MPa)	Fatigue life ratio of crack initiation N_i / N_f(%)
T2	378 to 621	<9
T3	378 to 702	<5
T4	243 to 702	<6

Figure 4.6 shows the scatter bands for weld toe and weld root failures. The predicted number of cycles is calculated by linear least squares fitting curves for each test type. Weld toe failures are scattered more widely compared to weld root failures. This also confirms the intrinsic feature of crack initiation from the surface of the weld toe and that the gap-tip at the weld root can be considered as a crack-like defect.

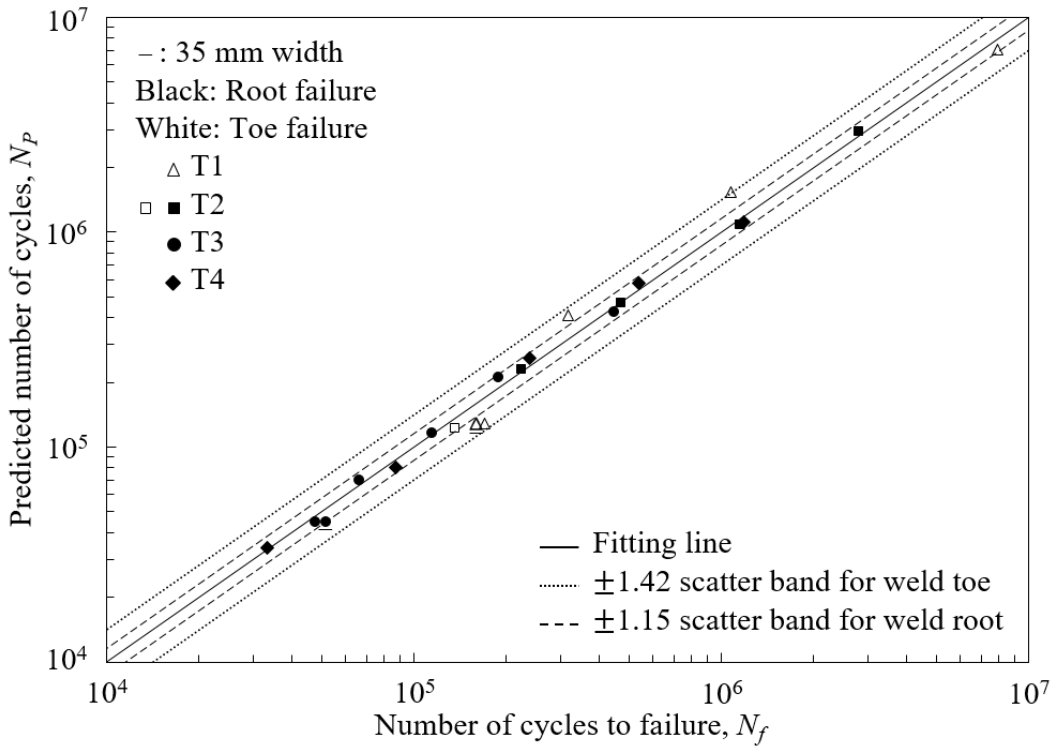

Figure 4.6: Scatter bands for weld toe and weld root failures

4.3 Fatigue crack front

Fatigue crack propagating at the crack front of the weld root was visualized by using the so-called beach marking technique. The visibility of crack surface striations was generated by reduction of the stress range and increase of the frequency. For a specimen of T3, the load ratio therefore was altered from 0.1 ($\Delta\sigma_n = 540$ MPa, frequency at 6–7 Hz) to 0.7 ($\Delta\sigma_n = 180$ MPa, frequency at 12–14 Hz) at the constant maximum bending load ($\sigma_{\max} = 600$ MPa). Figure 4.7 presents the beach mark loading pattern and Table 4.3 gives the number of cycles *N* for each individual block of beach mark.

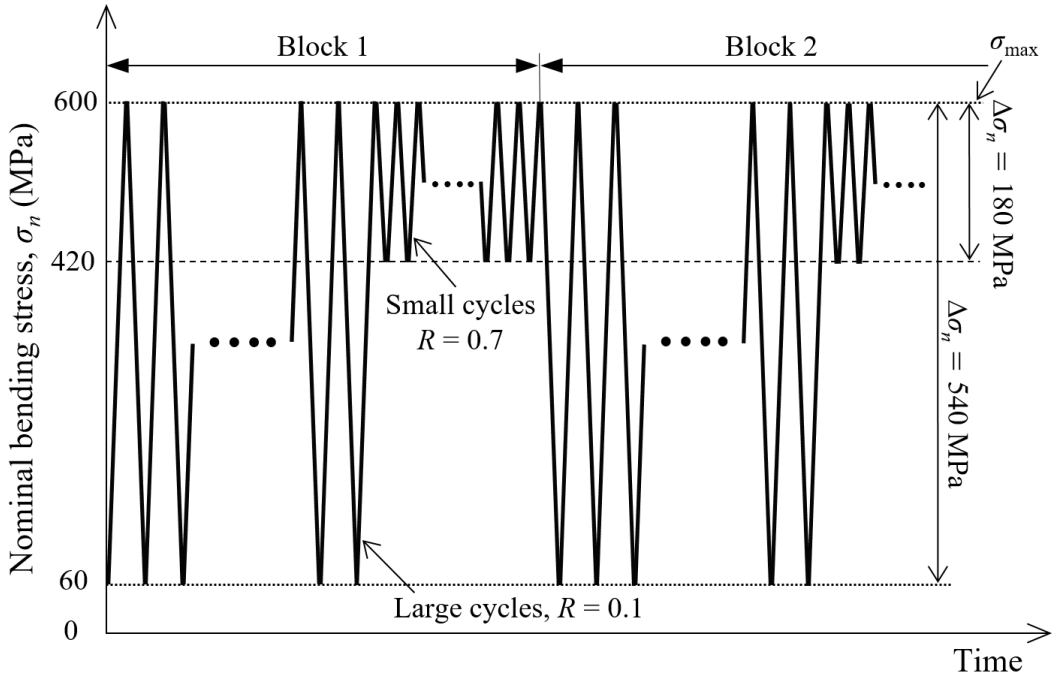

Figure 4.7: Fatigue beach mark loading pattern at constant σ_{max}

Figure 4.8 shows the beach marks created during crack propagation. A uniform through crack is observed at the crack front and in a large region at the middle of the fatigue fracture surface ($a/2c \simeq 0$, a and c are the crack depth and width, respectively).

Table 4.3: Number of large $(R = 0.1)$ and small $(R = 0.7)$ cycles for each individual block of beach mark

Block, n	1	2	3	4	5	6	7
$R = 0.1$	27010	25000	21000	16500	13500	9500	1755
$R = 0.7$	75000	63000	49500	40500	26500	16000	-

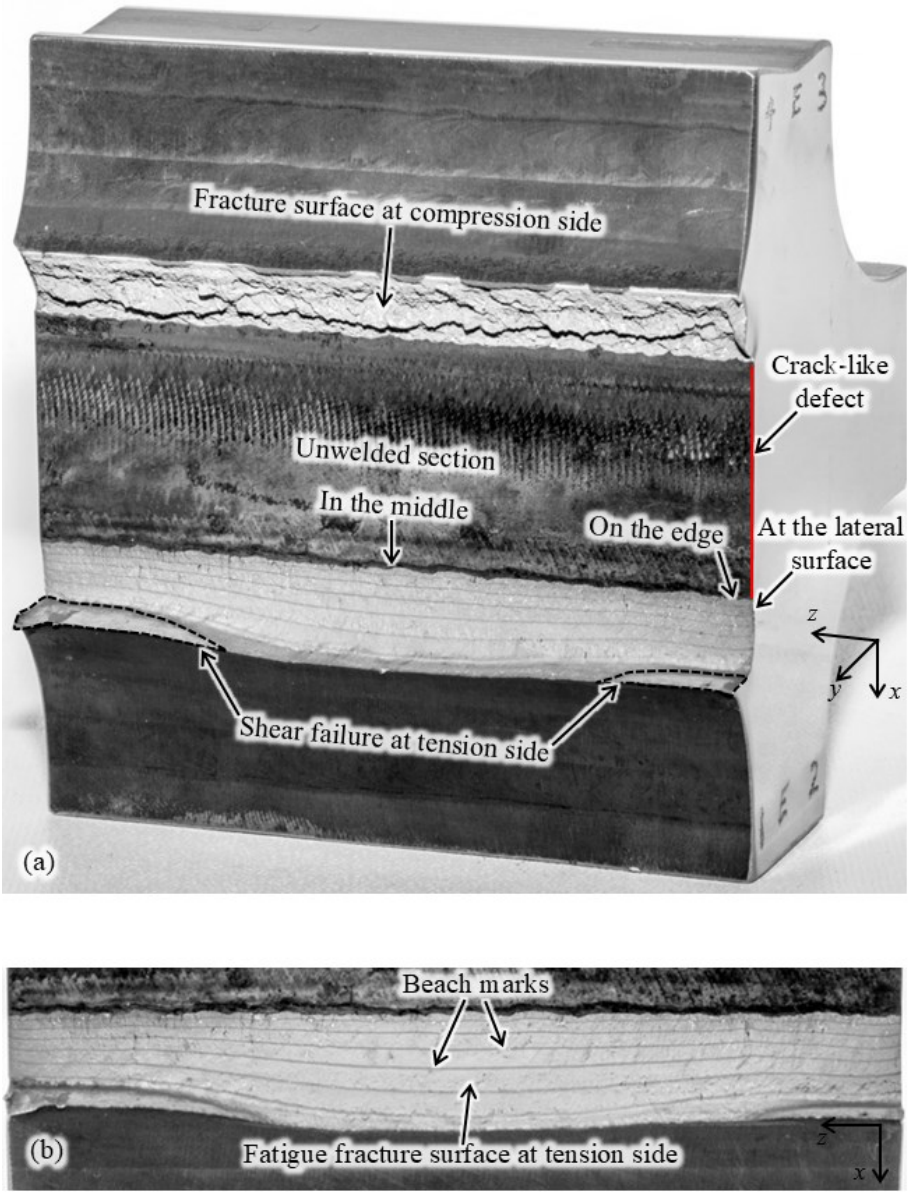

Figure 4.8: (a) Broken welded joint after final fracture and (b) experimental fatigue beach marks created during crack propagation

Figure 4.9 shows crack length versus fatigue life ratio for crack propagation at the lateral surface and on the fracture surface. Figure 4.8a shows the locations used to measure the crack length. The results are presented for the crack length induced by large cycles, and by large and small cycles. The number of small cycles is not considered on the horizontal axis. All curves exhibit a

quasi-immediate crack propagation from the crack front. Half fatigue life $(N / N_f = 0.5)$ has been spent to merely propagate the crack by approximately 2 mm. Crack length monitored at the lateral surface demonstrates close to that on the edge of the fracture surface. For high fatigue life ratio, there is a gradually increasing difference between crack lengths monitored at the lateral surface and measured in the middle of the fracture surface. The crack growth in the middle of the fracture surface is slightly faster when the crack is longer. Crack monitoring at the lateral surface can be implemented effectively to calculate FCGR for a long range of fatigue life ratio.

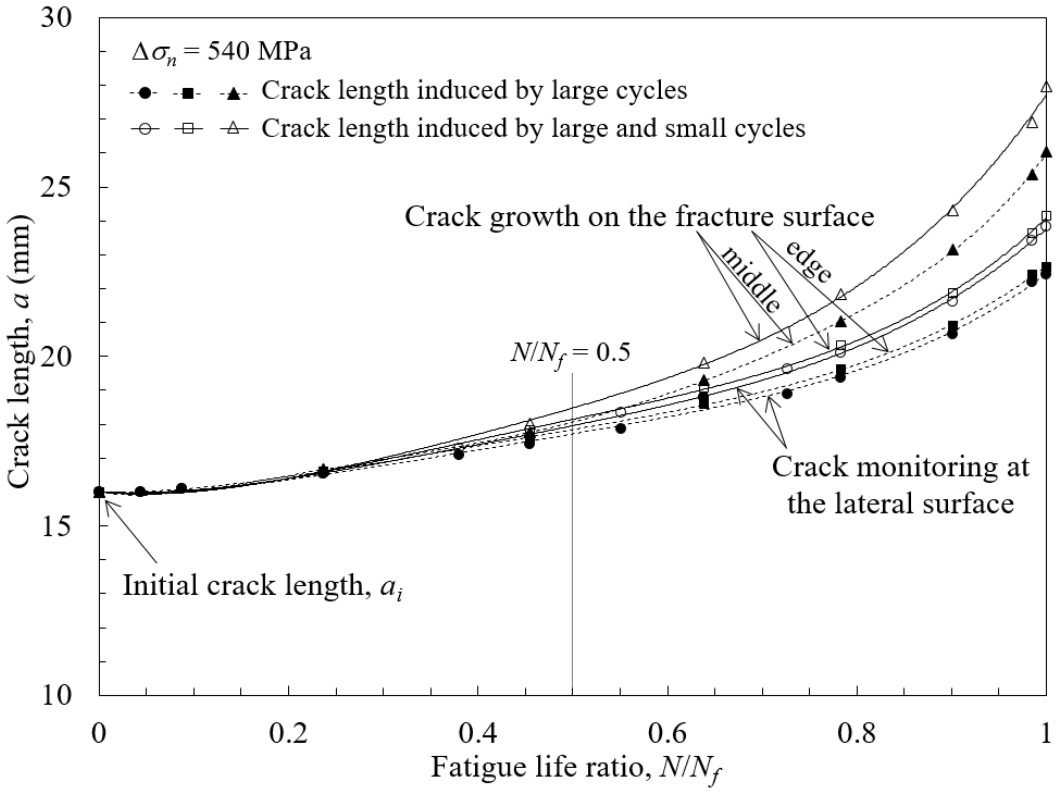

Figure 4.9: Fatigue crack length induced by large cycles, and by large and small cycles at three locations: at the lateral surface, and on the edge and in the middle of the fracture surface

4.4 Crack growth at the weld root

Figure 4.10 shows the leading and secondary crack lengths versus fatigue life ratios for the weld roots in tension. The crack length was monitored by the traveling microscopes at the lateral surfaces. A quasi-immediate crack propagation is found from leading roots for T2 and T3.

For T2, there was no quasi-simultaneous propagation of two fatigue cracks at the two weld roots in tension. T3 presented a quasi-simultaneous propagation of two fatigue cracks at the two weld roots in tension except at the lowest stress range of 378 MPa.

At $N / N_f = 0.5,$ crack length between 1.3 and 2.6 mm was measured for leading cracks at the weld root of T2 whereas it was between 1.6 and 2.3 mm for T3. Hence, the role of first weld pass strength is significant in the total fatigue life at the weld root. A similar result was found in the case of austenitic and martensitic first weld passes.

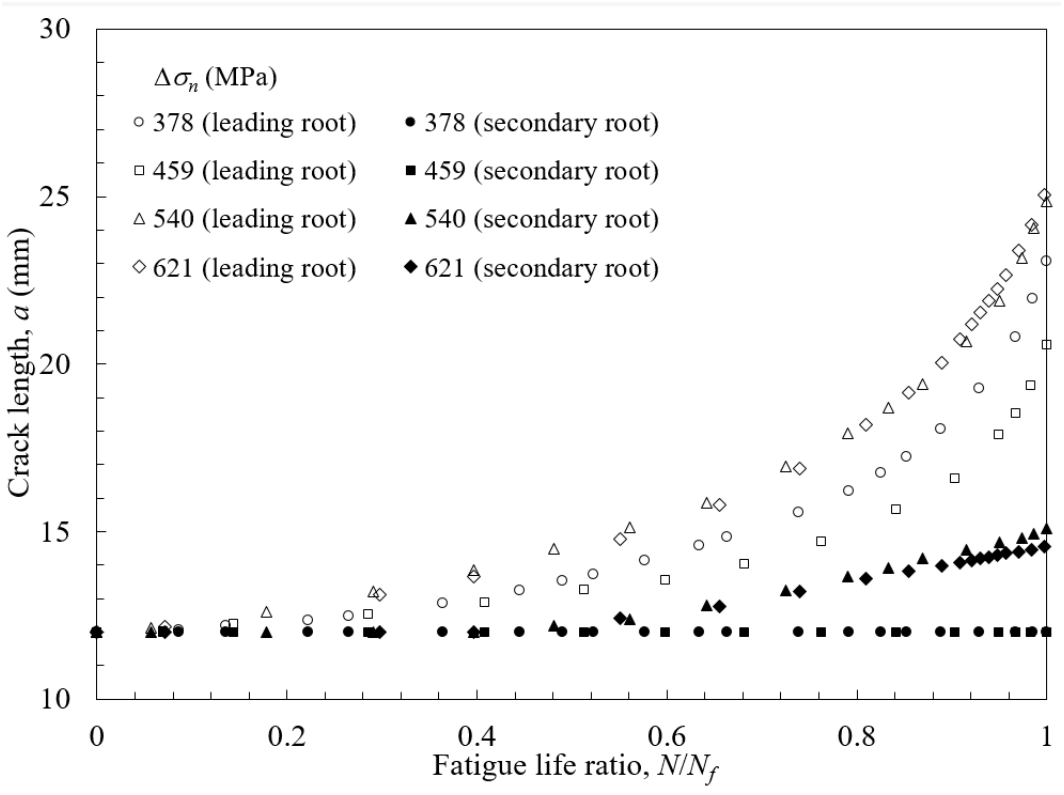

(a)

Figure 4.10: Lengths of leading and secondary cracks versus fatigue life ratios for the weld roots in tension: (a) T2 and (b) T3

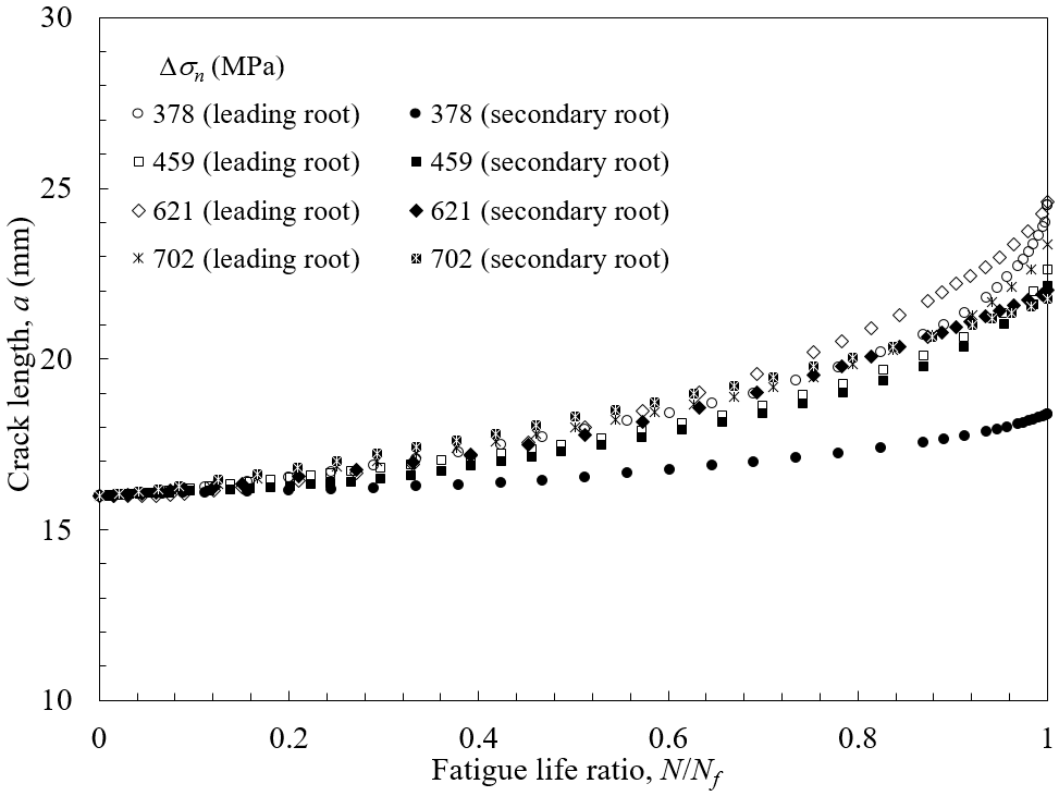

(b)

Figure 4.10 (continued): Lengths of leading and secondary cracks versus fatigue life ratios for the weld roots in tension: (a) T2 and (b) T3

CHAPTER 5 NUMERICAL COMPUTATIONS AND RESULTS

5.1 Assessment of mode I and mode II SIFs

The current numerical study presented in the following section explores the parameters influencing the accuracy of computed mode I SIFs of a through-thickness center crack. The displacement extrapolation method (DEM) and interaction integral method (IIM), implemented in the ANSYS® software [96], are employed. The numerical results are compared with the analytical solution reported by Isida [72], and some recommendations are given to increase the accuracy of calculated mode I SIFs. These are then used to assess mode I and mode II SIFs at the weld root crack tip of a load-carrying cruciform fillet welded joint loaded under three-point bending. The pertinence of the recommendations for mode I SIF calculations and the mixed-mode SIF sensitivity to the influencing parameters are then evaluated. The results of this section are published in Journal of Failure Analysis and Prevention [136].

5.1.1 SIF analysis of the crack tip of a center crack

Influence of numerical K-solution methods

The percent difference e_K is given in Table 5.1 for the modeling conditions of $a/b = 0.5$, $n = 2$ and 12, $a/L_B = 5$ and 10, and $L_B/L_T = 1$ and 5. Parameters are introduced in Section 3.4.1. The results obtained with IIM are considerably more accurate than those obtained with DEM. This observation further supports the presumption that the energy-based method is more accurate and efficient to compute SIFs than the near-tip field extrapolation method [79, 91, 95, 98].

Influence of different types of quadratic elements

For 6-node triangle and 8-node quadrilateral elements, adopting different shapes of the quadratic elements in the body itself had no noticeable effect on the accuracy of the calculated SIF (Table 5.1). This was also concluded by Guinea et al. [78]; however, Han et al. did not find a

consistent effect of different shapes on the results [79]. For the rest of this study, only 6-node triangle elements were used for the body.

Table 5.1: Percent difference e_K with respect to the analytical solution reported by Isida [72] for different conditions

$(n,\ a/L_B,\ L_B/L_T)$	DEM		IIM	
	Triangle	Quadrilateral	Triangle	Quadrilateral
(2, 5, 1)	−6.83	−7.65	−0.54	−0.87
(12, 5, 1)	+0.21	+0.23	−0.01	−0.01
(12, 5, 5)	+0.07	+0.09	0.00	−0.02
(2, 10, 1)	−6.61	−7.67	−0.28	−0.85
(12, 10, 1)	+0.13	+0.15	0.00	−0.01
(12, 10, 5)	+0.08	+0.09	0.00	−0.01

Influence of angular discretization around the crack tip and finite element size

Figure 5.1 shows the effects of different angular discretizations around the crack tip and element sizes on the results obtained with DEM and IIM. The results are presented for $n = 2$ to 18 and for a very coarse mesh of $a/3$ to a very fine mesh of $a/50$. The combination of angular discretization and element size plays a significant role in the accuracy of the numerical *K*-solution with DEM (Figure 5.1a). Compared to the element size, the angular discretization has a greater effect on the SIF estimation. Furthermore, as illustrated in Figure 5.1b (a close-up view of Figure 5.1a), there is no significant change in the estimated K_I values between the fine mesh of $a/20$ and $a/50$. Figure 5.1c (and the close-up view in Figure 5.1d) depicts the effects of different angular discretizations around the crack tip and element sizes on the results obtained with IIM. When

discretization with at least 5 elements around the crack tip was used, the K_I value converges to an exact estimation for element sizes of less than $a/5$.

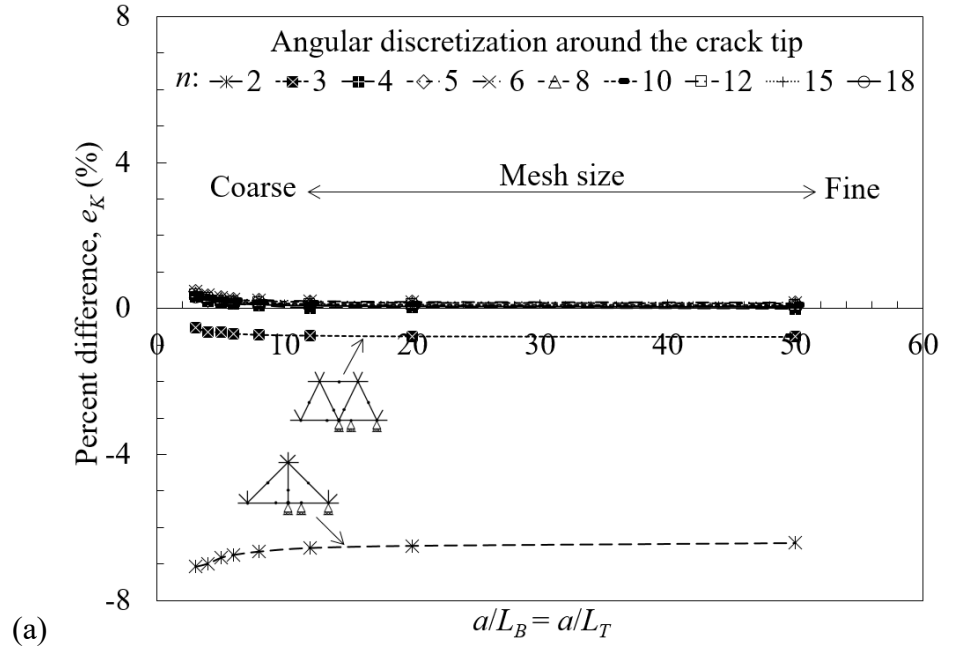

(a)

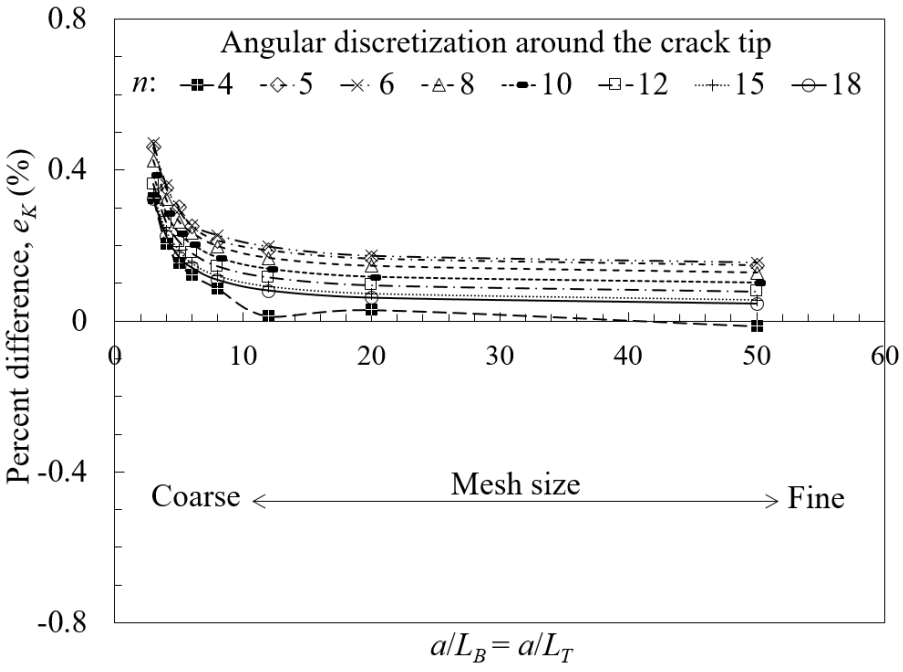

(b)

Figure 5.1: Effects of angular discretization around the crack tip and element size on the accuracy of the K_I value calculated with: (a) and (b) DEM, and (c) and (d) IIM

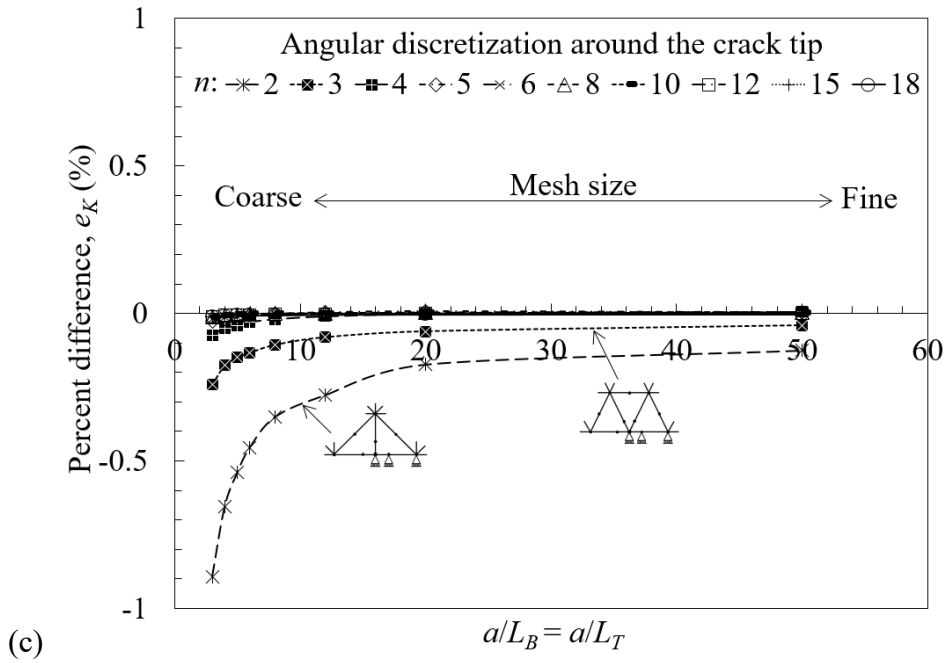

(c)

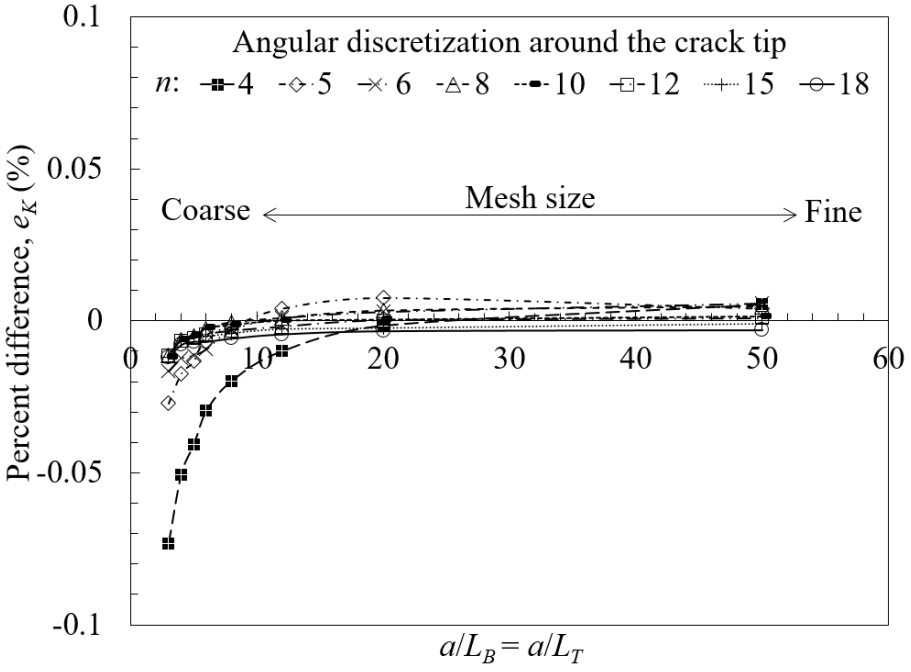

(d)

Figure 5.1 (continued): Effects of angular discretization around the crack tip and element size on the accuracy of the K_I value calculated with: (a) and (b) DEM, and (c) and (d) IIM

The recommended element size at the crack tip for DEM is $a/8$ or smaller [96], and roughly one element every 30° in the circumferential direction $(n=6)$ is suggested for a 2D model [78, 96]. These conditions yield a percent difference of +0.23. The computed error is +0.14% for one element every 15° $(n=12)$. This represents an improvement in the accuracy of approximately 40%, while the number of elements increased by a mere 1.3% (from 918 to 930). For two ranges of percent difference with DEM, Table 5.2 compares the number of elements in the model required for different combinations of angular discretization around the crack tip and element size. For a given percent difference range, a smaller number of elements can be achieved when a larger angular discretization around the crack tip and larger element size were introduced.

Table 5.2: Number of elements required for different combinations of angular discretization around the crack tip and element size for two ranges of percent differences obtained with DEM

e_K (%)	n	$a/L_B = a/L_T$	Number of elements
+0.17 to +0.18	18	5	440
	12	6	544
	10	8	920
	8	12	2002
	6	20	5822
+0.11 to +0.12	15	8	944
	12	12	2062
	10	20	5818
	9	50	35100

Influence of local mesh refinement

Figure 5.2 shows the effect of local mesh refinement on the results obtained with DEM and IIM for $L_B / L_T = 1$ to 10. An angular discretization around the crack tip of $n = 12$ was selected. The percent difference is presented in two ways in Figure 5.2: (i) the element size in the body is constant while the element size around the crack tip decreases (Figure 5.2a and c), and (ii) the element size around the crack tip is constant while the element size in the body increases (Figure 5.2b and d).

For both conditions with DEM (Figure 5.2a and b), a consistent increase in the accuracy of the K_I values is obtained by increasing the mesh size ratio from 1 to 6 (Zone I), while its behavior becomes more chaotic at mesh size ratios of 6 or greater (Zone II) for larger element sizes. In other words, a higher mesh size ratio does not inevitably result in better estimation of K_I values. Local mesh refinement at the crack tip and coarsening mesh in the body have a slightly favorable effect for smaller element sizes with DEM. IIM (Figure 5.2c and d) achieves K_I values which are very close to the reference for mesh size ratios from $L_B / L_T = 1$ to 6 (Zone I), while its value becomes more chaotic at mesh size ratios of 6 or greater (Zone II).

Influence of Poisson's ratio

Figure 5.3 shows the effect of the Poisson's ratio on the calculated K_I values under different conditions. An angular discretization around the crack tip of $n = 12$ was selected as in the previous section, while $a / L_B = 10$ and 20, and $L_B / L_T = 1,\ 5$, and 10.

Varying the Poisson's ratio from 0 to almost 0.4 had little effect on the K_I value estimated with DEM; however, the percent difference dramatically decreases for Poisson's ratios from 0.4 to 0.48. For $L_B / L_T = 1$ and 5 and Poisson's ratios between 0 and 0.4, the K_I value estimated with IIM is exact.

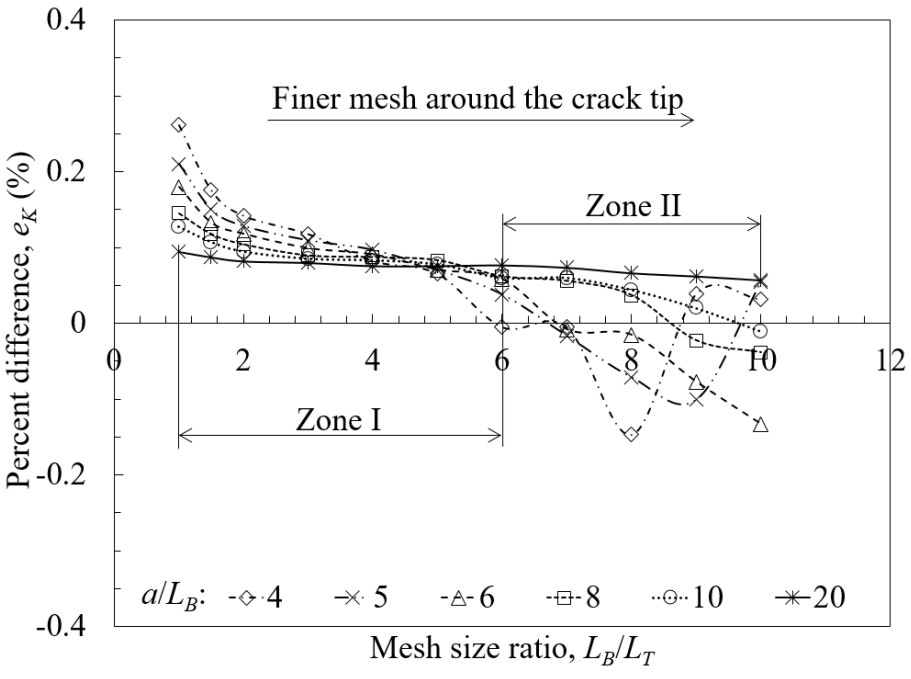

(a)

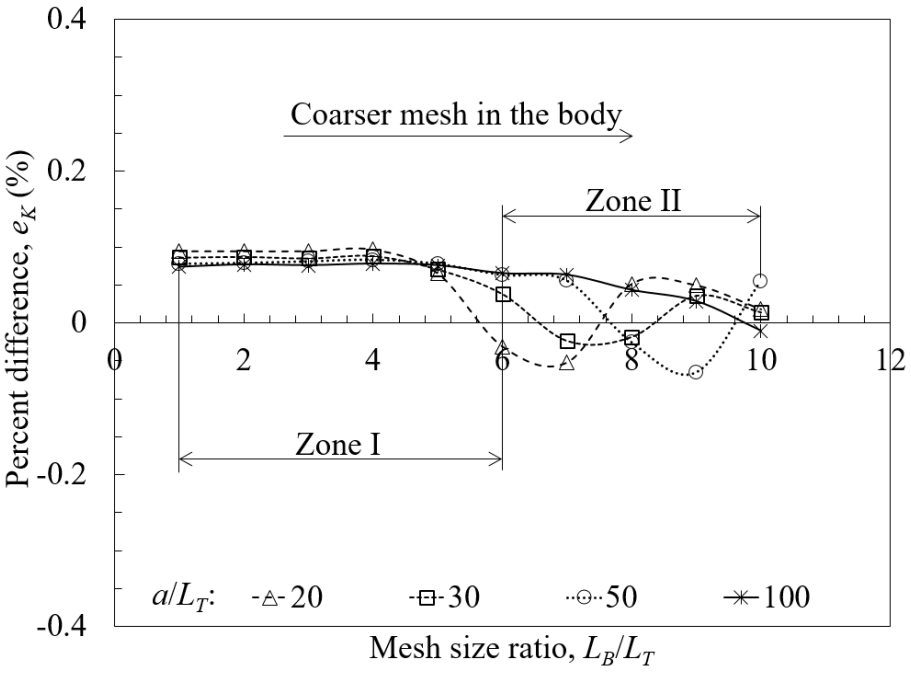

(b)

Figure 5.2: Effect of local mesh refinement on the accuracy of the K_I values calculated with: (a) and (b) DEM, (c) and (d) IIM

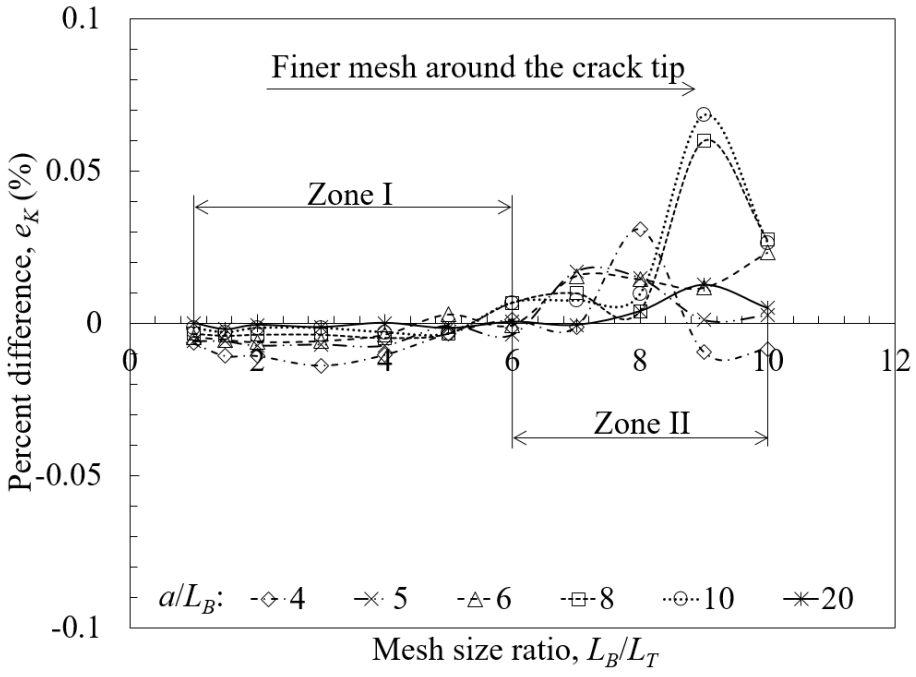

(c)

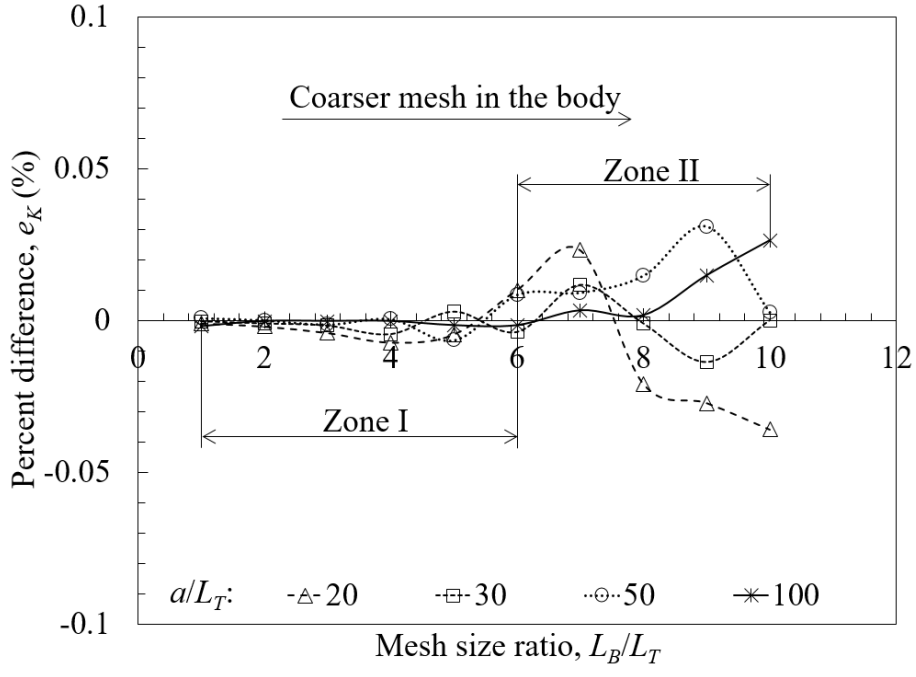

(d)

Figure 5.2 (continued): Effect of local mesh refinement on the accuracy of the K_I values calculated with: (a) and (b) DEM, (c) and (d) IIM

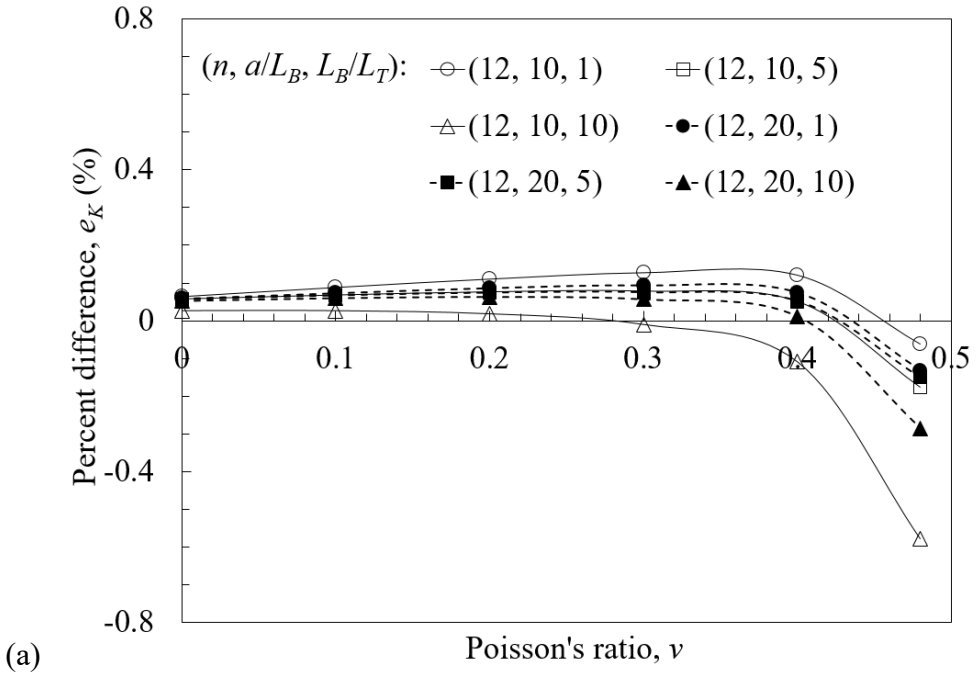

(a)

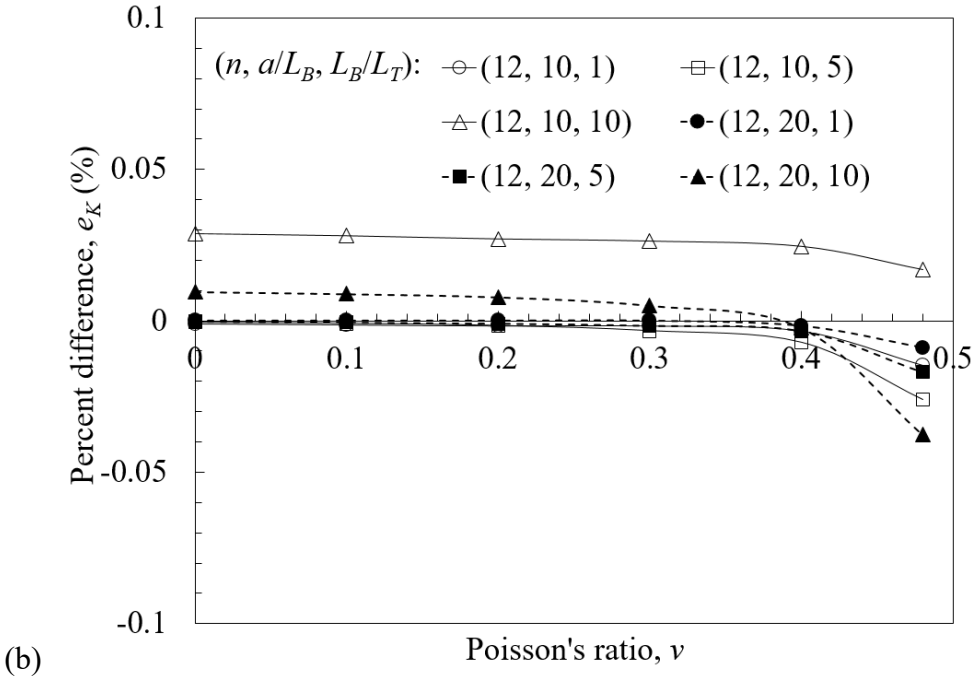

(b)

Figure 5.3: Effect of the Poisson's ratio on the accuracy of the K_I values calculated with: (a) DEM and (b) IIM

Influence of crack length

Figure 5.4 compares the percent difference in the results obtained with DEM and IIM for a/b from 0.1 to 0.6. Angular discretization around the crack tip, similar to the last two sections, was $n=12,$ while $a/L_B=10$ and 20 and $L_B/L_T=1,$ 5, and 10. Accurate analytical results reported by Isida [72] are presented to four significant digits except for $a/b=0.6;$ for this crack length, it is given to three significant digits. For all crack lengths, the results obtained with DEM are less accurate than those obtained with IIM. The local mesh refinement exhibits a consistently favorable effect on the K_I value accuracy except at $a/L_B=10$ and $L_B/L_T=10.$

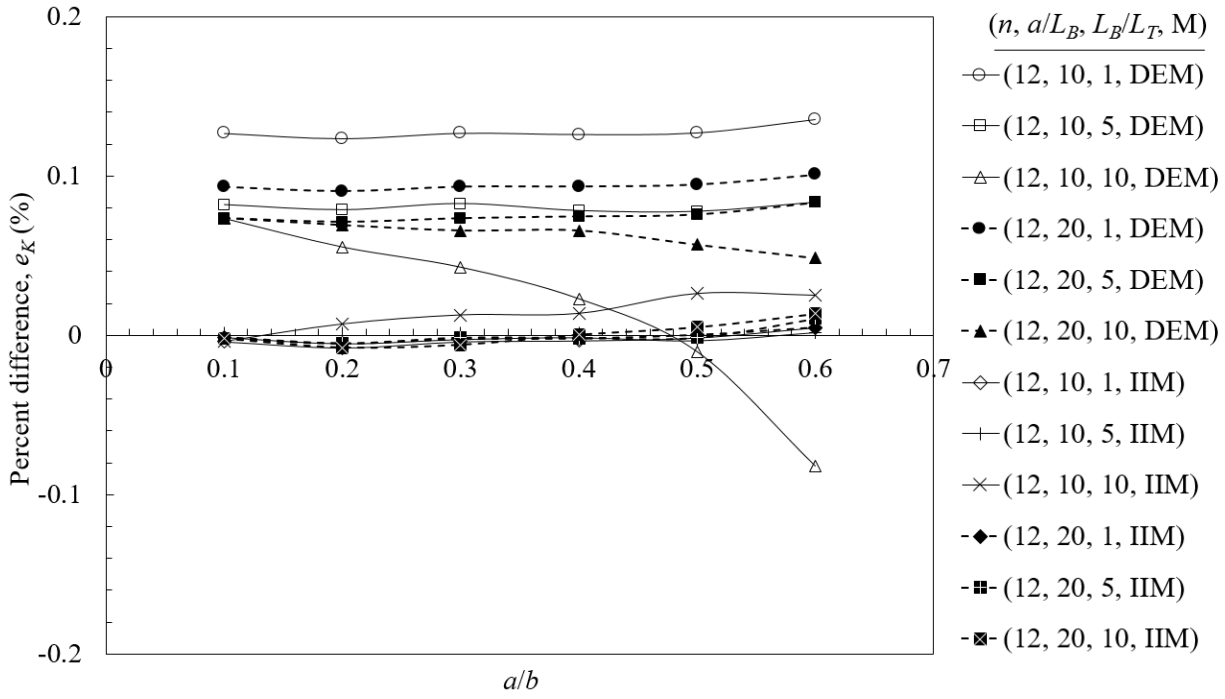

Figure 5.4: Effect of crack length on the accuracy of K_I values calculated with DEM and IIM

The geometry factor, *Y*, for the analytical solution and the two numerical methods is listed in Table 5.3 for varying crack length dimensionless parameters, $a/b.$ The results indicate that an accurate estimation was obtained with DEM and an exact estimation with IIM for three digits after

the decimal point. The percent difference with DEM can therefore be calculated from the results of the energy-based IIM, which is used in the following section to investigate a cruciform joint.

Table 5.3: Geometry factors, $Y = K_I / (\sigma\sqrt{\pi a})$, for different crack length dimensionless parameters

a/b	Analytical solution	DEM		IIM	
	Isida (1971) [72]	(12, 10, 5)	(12, 20, 5)	(12, 10, 5)	(12, 20, 5)
0.1	1.007	1.008	1.008	1.007	
0.2	1.029	1.030	1.029	1.029	
0.3	1.066	1.067	1.067	1.066	
0.4	1.122	1.123	1.123	1.122	
0.5	1.203	1.204	1.204	1.203	
0.6	1.32	1.322	1.322	1.321	
0.7	-	1.506	1.506	1.505	

Note: $(x,\ x,\ x)$ corresponds to $(n,\ a/L_B,\ L_B/L_T)$.

5.1.2 SIF analysis of the weld root crack tip of a cruciform joint

Influence of angular discretization around the crack tip

The effect of angular discretization around the crack tip for three crack lengths, $2a/t = 3/9,\ 6/9,$ and $9/9$ of the cruciform joint $(L_B/L_T = 5)$ and for one crack length, $a/b = 0.5,$ of a center crack $(L_B/L_T = 1$ and 5) were analyzed. The results for both geometries were obtained for $n = 5$ to 18

(36° to 10°). The element size in the body L_B was defined as $a/15$ in order to satisfy the exact estimation condition obtained with the energy-based method.

For the cruciform joint, while IIM presented rather stable mode I and mode II SIFs, DEM delivered slightly decreasing K_I and dramatically increasing K_{II} values for n from 5 to 18. The recommendations made previously for the center crack therefore satisfied the exact estimation with the energy-based IIM. The error in the estimation of K_I and K_{II} values with DEM can be calculated from the results obtained with IIM. The percent difference was calculated as follows:

$$e_K(\%) = \frac{K_{I,\,II(\mathrm{DEM})} - K_{I,\,II(\mathrm{IIM})}}{K_{I,\,II(\mathrm{IIM})}} \times 100 \tag{5.1}$$

Figure 5.5 shows the percent difference with DEM calculated using Equation (5.1) for both the cruciform joint and center crack geometries. Errors in the calculation of K_I values exhibit the same trend in both geometries with increasing angular discretization number. The percent difference for the cruciform joint is nearly the same as for the center crack. In other words, angular discretization has the same effect on the K_I value estimated with DEM for both typical and complex crack geometries. For the mode II SIF, the trend in the percent difference is completely different from that of the mode I SIF. Angular discretization has a strongly favorable effect on estimation of the mode II SIF. It can also be observed that crack length has an effect on the estimation of the mode II SIF, while the mode I SIF is almost independent of the crack length.

Influence of finite element size

The effect of the finite element size for three crack lengths, $2a/t = 3/9,\ 6/9,$ and $9/9,$ of the cruciform joint $(L_B/L_T = 5)$ and for one crack length, $a/b = 0.5,$ of the center crack $(L_B/L_T = 1$ and 5) was investigated. The percent differences were calculated in both geometries for a/L_B from 6 to 50. An angular discretization of $n = 12$ was chosen to satisfy the exact estimation condition of the energy-based method.

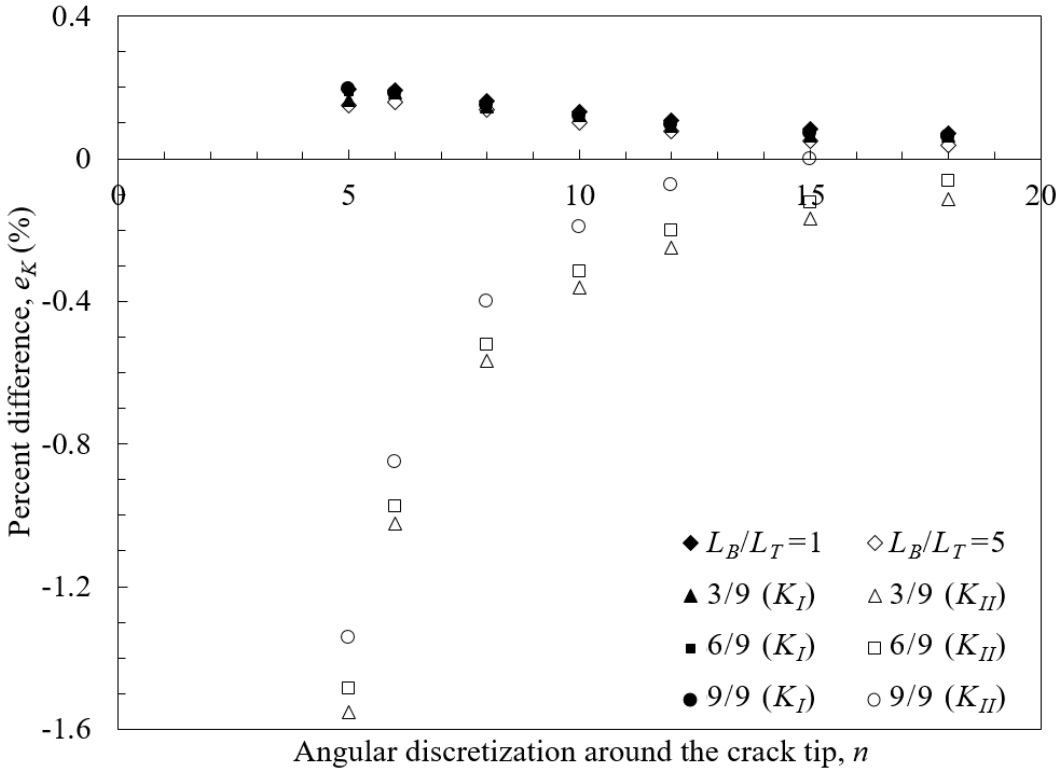

Figure 5.5: Effect of angular discretization around the crack tip on the accuracy of K_I and K_{II} values obtained with DEM for three crack lengths, $2a/t = 3/9,\ 6/9,$ and $9/9,$ of the cruciform joint $(L_B/L_T = 5)$ and for one crack length of the center crack $(L_B/L_T = 1$ and $5)$

For the cruciform joint, while IIM presented rather stable mode I and mode II SIFs, both the K_I and K_{II} values obtained with DEM are inversely proportional to the increase in element size from $a/6$ to $a/50$. The percent differences of the K_I and K_{II} values estimated with DEM can be calculated using Equation (5.1). Figure 5.6 presents the percent difference for the results obtained with DEM. The errors in the calculation of K_I values for both geometries illustrate the same trend with decreasing element size. The percent difference presented for the cruciform joint is similar to the center crack, and therefore the percent difference from Figure 5.1a (or b) is applicable to complex crack geometries. Similar to the angular discretization effect, element size has a significant effect on the mode II SIF estimation for large crack lengths. The mode II SIF can also be significantly affected by the crack length.

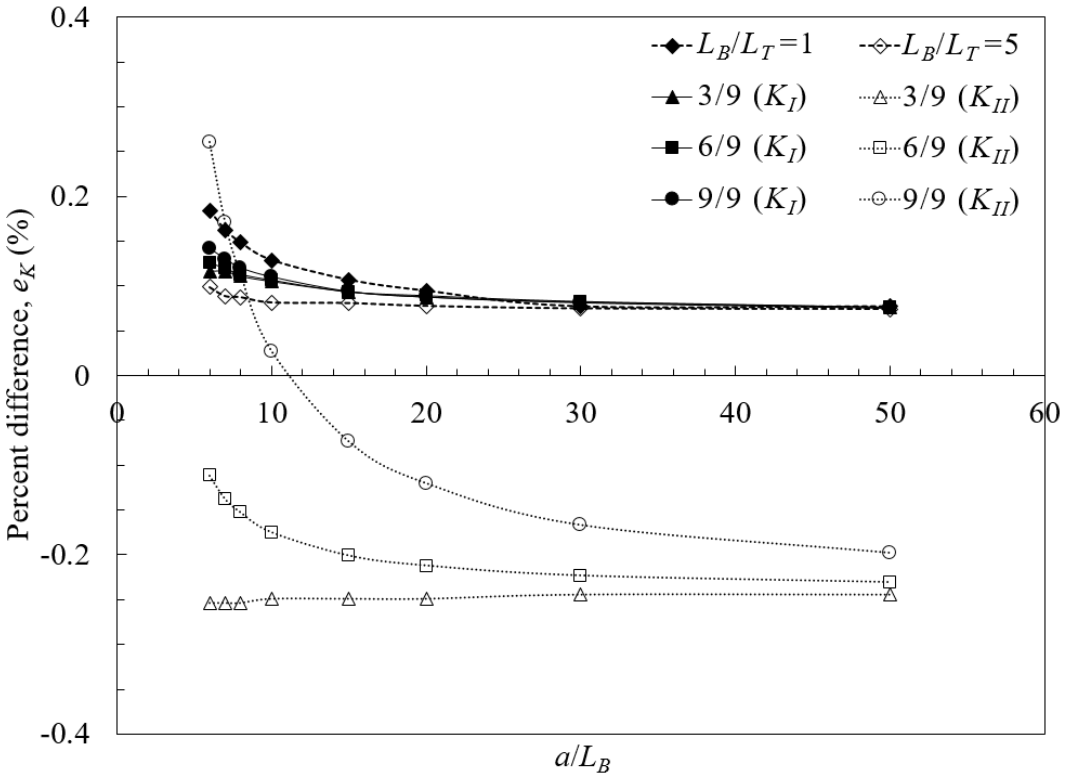

Figure 5.6: Effect of element size on the accuracy of K_I and K_{II} values obtained with DEM for three crack lengths, $2a/t = 3/9,\ 6/9,$ and $9/9,$ of the cruciform joint $(L_B/L_T = 5)$ and for one crack length of the center crack $(L_B/L_T = 1$ and 5)

Influence of crack length on DEM

Figure 5.7 shows the e_K for the calculation of the SIF by DEM with respect to the SIF calculated with IIM (Equation (5.1)) for crack lengths, $2a/t,$ from $2/9$ to $12/9$. The angular discretization number, element size in the body, and mesh size ratio were $n = 12$ in 180° (15° each), $a/15,$ and 5, respectively. As shown in Figures 5.4, 5.5, and 5.6, the percent difference in the calculation of K_I with DEM is almost independent of the crack length, while the percent difference in the K_{II} value is dependent.

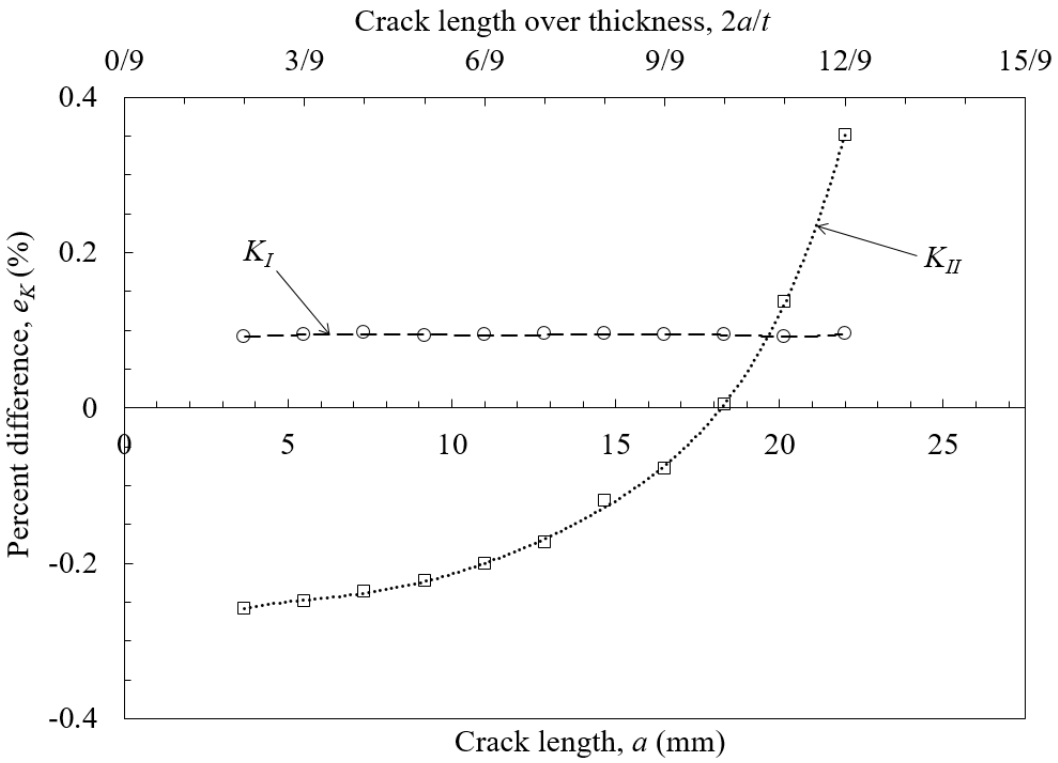

Figure 5.7: Effect of crack length in the cruciform joint on the accuracy of K_I and K_{II} values calculated with DEM

5.2 Numerical computations for studied cruciform joint

The ANSYS® finite element software package [96] was used to calculate the stress intensity factor (SIF) and the non-singular *T*-stress at the weld root crack tip, and the stress concentration factor (SCF) at the weld toe notch in the load-carrying cruciform fillet welded joint. The plane strain condition in a 2D model exploiting lateral symmetry was analyzed in this study (Figure 5.8a). In the cases of symmetrical and dissymmetrical crack propagations, plane strain condition in a full 2D model was generated instead. Under fully linear elastic behavior, elastic modulus *E* and Poisson's ratio ν of the material were set as 195 GPa [65] and 0.3, respectively. The model was subjected to a three-point bending load *F*. The corresponding nominal bending stress range at the weld root was equal to 100 MPa calculated from Equation (3.1) (at point A in Figure 3.1).

The use of quadratic elements instead of linear elements results in more accurate calculations [79]. Six-node triangle elements therefore were adopted in the finite element model. To calculate accurate SIF and *T*-stress at the weld root and SCF at the weld toe, local mesh refinements were generated in the vicinity of the weld root crack tips and the weld toe radius, see Figure 5.8a.

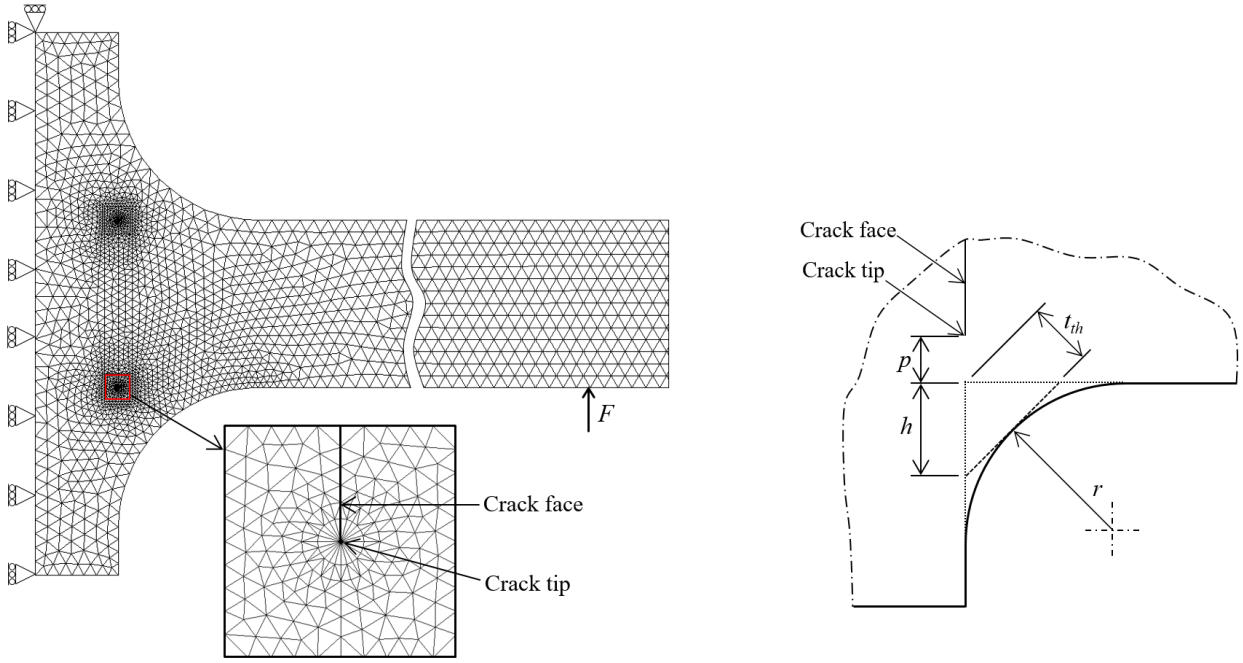

(a) (b)

Figure 5.8: (a) Mesh pattern for $r = 27.5$ mm and $2a/t = 3/3$ with designation of boundary conditions and loading. (b) Leg length *h* for flat face fillet weld based on the conventional design method for the theoretical throat t_{th}

5.2.1 SIF at the weld root crack tip

Triangular quarter-point elements were used at the crack tip to represent the crack tip singular strain field, as suggested by Barsoum [76, 82]. The result of the integral method is independent of the integration contour which allows the contour to be chosen far from the crack tip yet with a good accuracy. The convergence of the method was evaluated over three integral paths adjacent to the

first row of singular elements at the crack tip to ensure effective validation of the *K* values. The numerical simulation of the SIF was carried out using the optimum parameters investigated in Section 5.1.

SIF for initial crack length

The IIM [90], which is based on the path independent *J*-integral [88], was employed to calculate the mode I (K_I) and mode II (K_{II}) SIFs. The equivalent SIF (K_{eq}) was then given by:

$$K_{eq} = \sqrt{K_I^2 + K_{II}^2} \tag{5.2}$$

Figure 5.9 shows the ΔK_I, ΔK_{II}, and ΔK_{eq} computed for studied load-carrying cruciform fillet welded joint with concave fillet weld (round weld toes) under three-point bending load. In addition, the $\Delta K_{eq,\,\mathrm{FP}}$ and $\Delta K_{eq,\,\mathrm{BS}}$ are presented for a flat face fillet weld under pure bending load. The $\Delta K_{eq,\,\mathrm{FP}}$ (dashed line) was numerically calculated and $\Delta K_{eq,\,\mathrm{BS}}$ (solid line) was determined from existing equations given by the British Standard [71]. The leg length *h* for the flat face fillet weld was determined according to the conventional design method for the theoretical throat t_{th} as schematically shown in Figure 5.8b. The ΔK_{eq} was 27%, 21%, and 15% less than $\Delta K_{eq,\,\mathrm{BS}}$ for $2a/t = 1/3,\ 2/3$, and 3/3, respectively.

SIF for symmetrical and dissymmetrical crack propagations

The domain integral method [89] which is based on the *J*-integral method [88] was used to calculate the SIF. The path independent *J*-integral for a cracked body is equal to the energy release rate in linear elastic material [88], therefore the equivalent SIF K_{eq} for plane strain condition was calculated from:

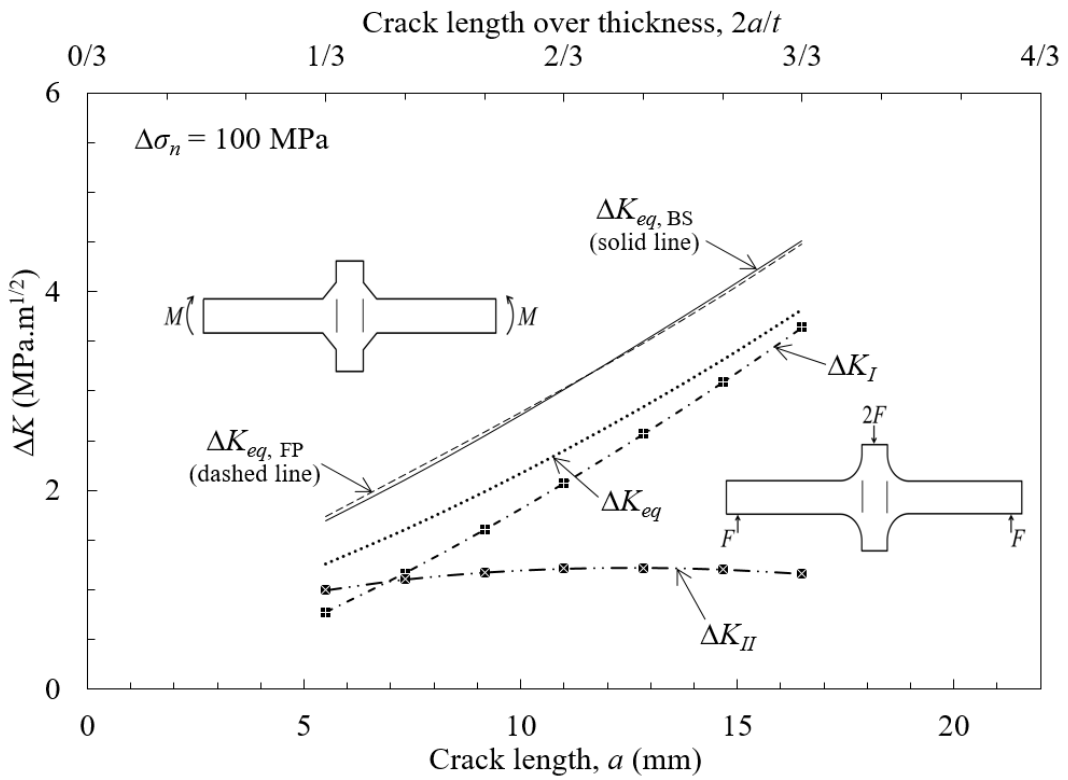

Figure 5.9: SIF versus weld root crack length for load carrying cruciform fillet welded joints

$$K_{eq} = \left(\frac{JE}{1-\nu^2} \right)^{1/2} \tag{5.3}$$

The equivalent SIF range ΔK_{eq} was calculated for two conditions of symmetrical and dissymmetrical crack propagations. Figure 5.10 presents ΔK_{eq} in terms of crack length a for symmetrical and dissymmetrical crack propagations for each T2 and T3 conditions. The averaged ΔK_{eq} curves display a deviation of less than 2% with respect to symmetrical and dissymmetrical crack propagation curves. Thus, averaged $a - \Delta K_{eq}$ curves of T2 and T3 were utilized for these two scenarios and any crack propagation scenario between them in this study.

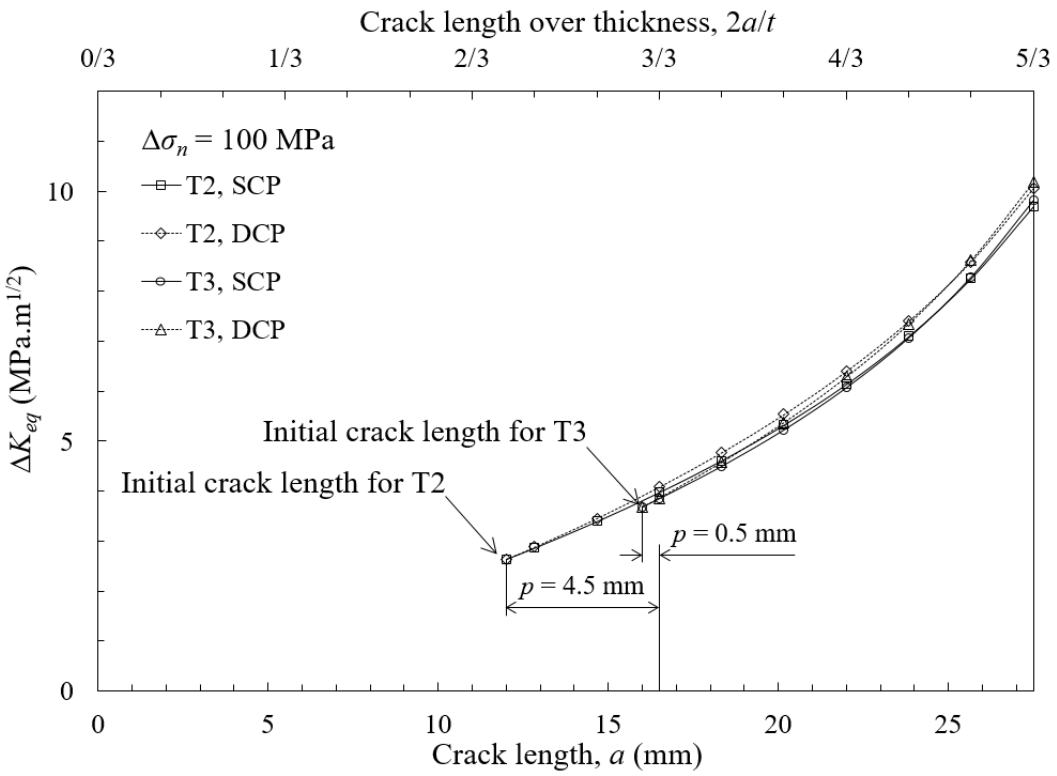

Figure 5.10: Equivalent SIF range versus crack length for symmetrical (SCP) and dissymmetrical (DCP) crack propagations of T2 and T3

5.2.2 Non-singular *T*-stress

The stress field for mode I in the *x*-direction in a crack vicinity is expressed by [38]:

$$\sigma_{xx} = \frac{K_I}{\sqrt{2\pi r}} \cos\frac{\theta}{2}\left[1 - \sin\frac{\theta}{2}\sin\frac{3\theta}{2}\right] + T + O(r^{1/2}) \tag{5.4}$$

Two different approaches have been used to calculate the *T*-stress: (i) the displacement method and (ii) the stress difference method. The former method was proposed by Ayatollahi et al. (1998) [137] that can be used for any geometry and loading configuration; this method does not rely on either multiple analyses or special purpose numerical procedures.

The higher order terms are negligible around the crack tip and therefore, σ_{xx} in Equation (5.4) includes only the singular term and the *T*-stress. The *T*-stress can be determined by eliminating the

singular term along $\theta = -\pi$ or $+\pi$, and therefore $\sigma_{xx} = T$. According to the Hooke's law, it can be written:

$$T = E'\varepsilon_{xx} = E'\frac{\mathrm{d}u_x}{\mathrm{d}x} = E'\left[\frac{u_x(x) - u_x(0)}{x}\right] \tag{5.5}$$

where E' is the effective elastic modulus, which is equal to E and $E/(1-\nu^2)$ for plane stress and plane strain conditions, respectively; ε_{xx} and u_x are the strain and displacement parallel to the crack face; and $u_x(0)$ denotes u_x at the crack tip. The *T*-stress can be similarly calculated for a mixed-mode problem by setting:

$$T = \frac{E'}{2}\left[\left(\frac{\mathrm{d}u_x}{\mathrm{d}x}\right)_{\theta=-\pi} + \left(\frac{\mathrm{d}u_x}{\mathrm{d}x}\right)_{\theta=+\pi}\right] = \frac{E'}{2}\left[\frac{u_x(x,-\pi) + u_x(x,+\pi)}{x}\right] \tag{5.6}$$

The latter method was proposed by Yang et al. (1999) [138] that can be used directly by a single finite element analysis; the elastic *T*-stress can efficiently and accurately compute at a point ahead of a crack tip $(\theta = 0)$ by setting:

$$T = \lim_{r\to 0}\left(\sigma_{xx} - \sigma_{yy}\right) \tag{5.7}$$

where σ_{yy} is the stress field in the *y*-direction. By the distance from the crack tip, the errors in the computed values of stress increase and their difference may effectively eliminate the errors. Simplicity in expression and less computation are the advantages of this method.

Leevers and Radon (1982) [40] proposed a dimensionless parameter called the stress biaxiality ratio *B* (Equation (2.5)). This crack tip stress field parameter can be considered as geometry-independent relative to the load biaxiality ratio. Table 5.4 presents the stress biaxiality ratio for two initial crack lengths calculated with the two methods. T2 and T3 have approximately similar negative stress biaxiality ratios. The negative *T*-stress was also obtained by Dong and Guedes Soares (2015) [112] for load-carry cruciform joints with flat face fillet weld under tension.

Table 5.4: Stress biaxiality ratios for T2 and T3

Method	T2	T3
Displacement method	–2.08	–2.06
Stress difference method	–2.88	–2.59

5.2.3 SCF at the weld toe notch

At the weld toe notch, an assessment of the sensitivity of the numerical results of principal stress to mesh size was performed. The mesh sensitivity analysis indicated that a minimum element size of 0.2 mm achieved better convergence to the results acquired for the studied geometries. The elastic SCF (K_t) was obtained by dividing the numerically calculated hotspot stress at the weld toe (the maximum principal stress at the weld toe notch) by the nominal stress through the analytical solution (Equation (3.1)) at point B (Figure 3.1) of the smooth beam:

$$K_t = \frac{\sigma_{\max}}{\sigma_n} \tag{5.8}$$

Figure 5.11 illustrates the elastic SCFs for different weld toe radii in terms of weld root crack lengths. As expected, the SCF is inversely correlated to the radius of the weld toe. The most striking result emerging from the data is that there is an augmentation of the SCF at the weld toe as a result of increasing the crack length at the weld root. For the weld toe radius of 27.5 mm, the SCF of no joint penetration $(2a/t = 3/3)$ is 1.5% higher than CJP. This effect is more pronounced on fatigue lives in the log–log scale *S*–*N* curve.

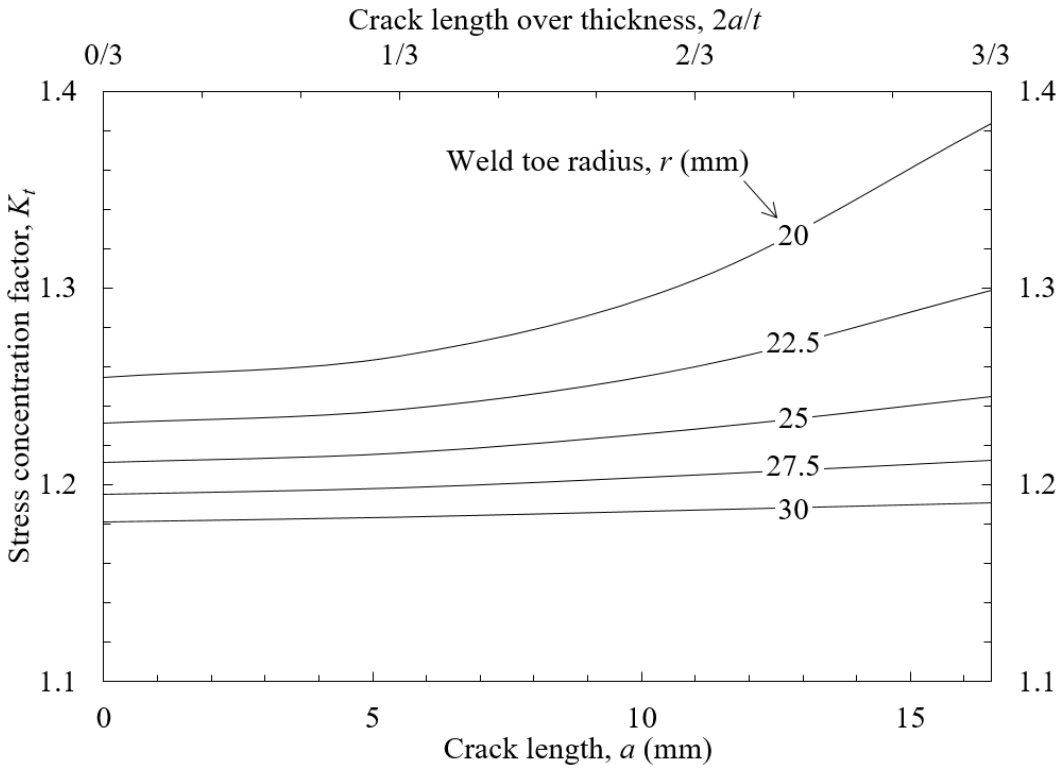

Figure 5.11: Effect of weld root crack length and weld toe radius on the elastic SCF at the weld toe

CHAPTER 6 GENERAL DISCUSSION

The nominal stress and N-SIF approaches are, respectively, used to investigate the failure mode transition and to unify the weld root fatigue strength of different weld penetration depths in load-carrying cruciform fillet welded joints under three-point bending load. The influence of different weld metals on the fatigue strengths of the presented geometry is investigated using these two approaches.

Weld root fatigue crack growth are then analyzed for two different weld penetration depths (T2 and T3). The main objective is to determine the FCG behavior in cruciform joint and compare with that of the compact tension (CT) specimen. Another objective is to evaluate the accuracy of the crack propagation approach in predicting fatigue life of cruciform joints. The findings of these sections will lead to a better understanding of the FCG behavior and fatigue life prediction for the weld root of the load-carrying cruciform fillet welded joint under bending load.

6.1 Fatigue failure mode transition

The assumption is based on the well-known fact that for a given material, the negative inverse slope of the fatigue *S–N* curve (in the log–log scale) obtained by testing a notched member is different from that obtained by testing a cracked member. The negative inverse slopes k of the fatigue *S–N* curves are listed in Table 6.1. The negative inverse slope of a weld toe failure is larger than that of a weld root failure (i.e., the weld toe failure of a notched member exhibited a lower slope compared to that of the weld root failure of a cracked member in the *S–N* curve). Various parameters such as weld penetration depth, weld metal fatigue property, roughness of the weld toe surface, SCF at the weld toe, and welding residual stress fields at the weld toe and root govern the fatigue failure mode transition.

For the weld toe failure, the fatigue phenomenon at the initiation stage is characterized by the roughness of the weld toe surface and the local stress field of the notched member. The effect of a mirror-like finish at the weld toe on the prolongation of fatigue life is shown in Figure 4.1. The slope of the weld toe failure curve, $k = 9.43,$ is sharper than that of smooth specimen, $k_{\text{smooth}} > 10$

[139, 140]. The fatigue notch factor K_f is a very important step in fatigue strength evaluations at the notch of a weld toe. It can be interpreted by the concept of SCF K_t [119, 120], which can also be affected by the weld toe radius and weld root crack length (Figure 5.11). Moreover, the fatigue strength of the weld toe can be affected by the high tensile welding residual stress present near the weld toe [111, 115].

Table 6.1: Negative inverse slope for each test type evaluated from Figure 4.1

Specimen type	Stress range, $\Delta\sigma_n$(MPa)	Negative inverse slope, k
T1	459 to 702	9.43
T2	378 to 621	5.13
T3	378 to 702	3.64
T4	243 to 702	3.29

The SIF (Figure 5.9) and crack closure effect represent a very important step in fatigue strength evaluations at the crack tip of the weld root. The closure measurements of AISI 415 at $R = 0.1$ of the CT specimens demonstrated that the crack closure is considerable at a SIF range lower than 21 MPa.m$^{1/2}$ (Figure 2.3) [65]. Additionally, there exists compressive welding residual stress in the vicinity of the weld root [111, 115], which can increase the magnitude of crack closure at the weld root of the cruciform joint. A higher compressive residual stress may have a favorable effect on fatigue life by closing the weld root crack face. For a specific $\Delta\sigma_n$, the crack closure is more likely to occur for smaller weld root crack length. Thus, T2 exhibits a lower sharp slope compared to T3 and T4.

The fatigue failure mode transition between weld toe and weld root can be observed in Figure 4.1. Different slopes of weld toe (T1) and weld root (T2) curves eventually lead to the fatigue failure mode transition. The T2 cruciform joint failed from the weld root at the low-stress range fatigue loading, while the similar geometry experienced fatigue failure from the weld toe at a higher stress

range. Interestingly, this finding is contrary to the results of studies conducted by other groups on load-carrying cruciform joints with flat face fillet welds under tension load [111, 112].

6.2 Consolidation of weld penetration depth effect

For a geometrically ideal cruciform joint with a crack-like defect at the weld root, the stress is singularly similar to the stress field at the crack tip. The N-SIF approach therefore can be effectively used for fatigue strength prediction. The experimental data on fatigue test results of T2 and T3 are plotted in Figure 6.1. On the secondary vertical axis, they are reconsidered in terms of equivalent SIF range ΔK_{eq} (Figure 5.9) obtained in Section 5.2.1.

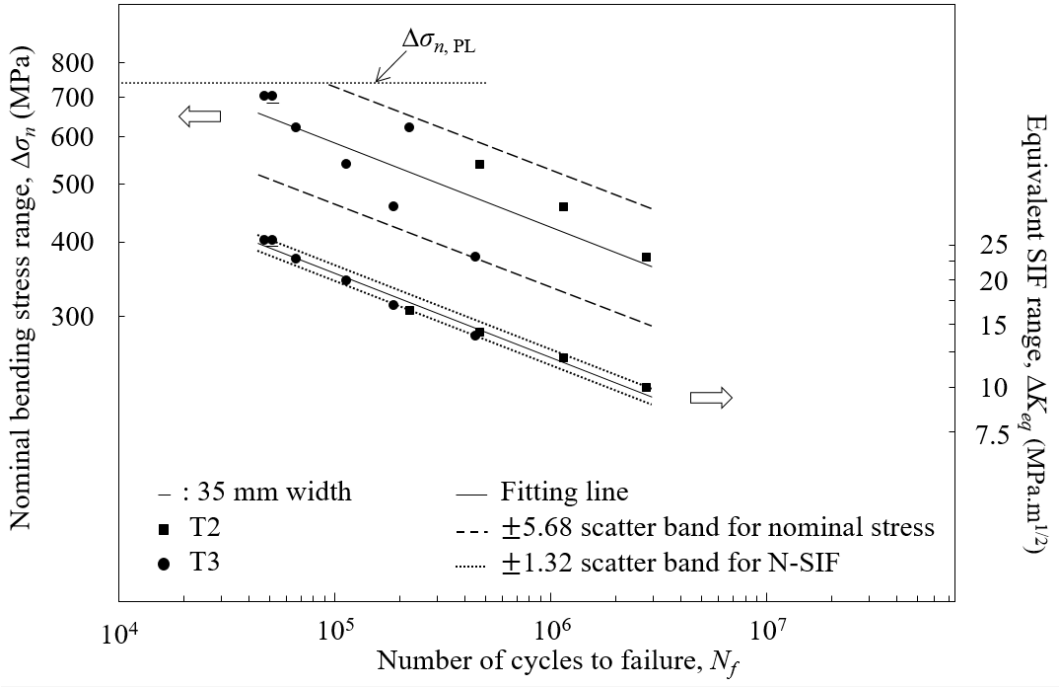

Figure 6.1: Nominal bending stress range and equivalent SIF range versus fatigue life

The nominal stress approach for T2 and T3 based on a single curve appears to be scattered more widely compared to the N-SIF approach. In fact, the crack initiation and crack propagation at the weld root are not controlled by only the nominal stress. It is evident that the scatter band decreases

considerably, meaning that the equivalent SIF range ΔK_{eq} is an influential parameter in fatigue strength prediction of weld root. In addition, implementing mode I SIF range ΔK_I (scatter band: ± 1.48) in comparison with ΔK_{eq} is not sufficient for decreasing the scatter band. The residual scatter mainly depends on differences in the slopes of T2 and T3 owing to variations in the crack closure intensity at the weld roots and the intrinsic scatter of fatigue experimental data for a single test type.

6.3 Fatigue strength of martensitic and austenitic stainless steels

The comparison of fatigue crack growth rate (FCGR) between martensitic (AISI 415, E410NiMo, and CA6NM) [64, 65] and austenitic (316L and E316L) [68] stainless steels (Figure 2.4), demonstrates that the FCGR of martensitic stainless steels is relatively lower than austenitic stainless steels. This confirms the results presented in Figure 4.1, concluding that martensitic weld metal E410NiMo has higher fatigue strength in comparison with austenitic weld metal E316L.

The fatigue *S–N* data of all weld root failures by the nominal stress approach are widely scattered owing to the effect of weld penetration depth and weld metal differences, hence creating an enlarged uncertainty space which naturally makes it an inapt option for evaluating design integrity. In contrast, the N-SIF approach can be effectively employed to show the effect of weld metals on fatigue strength. Figure 6.2 shows two curves characterizing the fatigue strength of martensitic and austenitic weld metals. Martensitic stainless steel exhibits higher fatigue strength when compared to austenitic stainless steel.

At HCF (more than 8×10^6 cycles), no cracking was observed at the weld roots of T1 and T4 corresponding to $\Delta\sigma_n = 459$ and 207 MPa, respectively. At these stress ranges, the magnitudes of equivalent SIF ranges are 7.07 and 7.62 MPa.m$^{1/2}$. Similar SIF values have been presented in the literature concerning the threshold SIF ranges for long cracks in the base and weld metals. The values of the threshold SIF range ΔK_{th} vary between 2 and 5 MPa.m$^{1/2}$ for martensitic stainless steels of AISI 415 and E410NiMo [64, 141], whereas they vary from 3 to 12 MPa.m$^{1/2}$ for austenitic stainless steels of E316L and 316L [142-144]. The threshold SIF ranges for both weld metals are indicated in Figure 6.2.

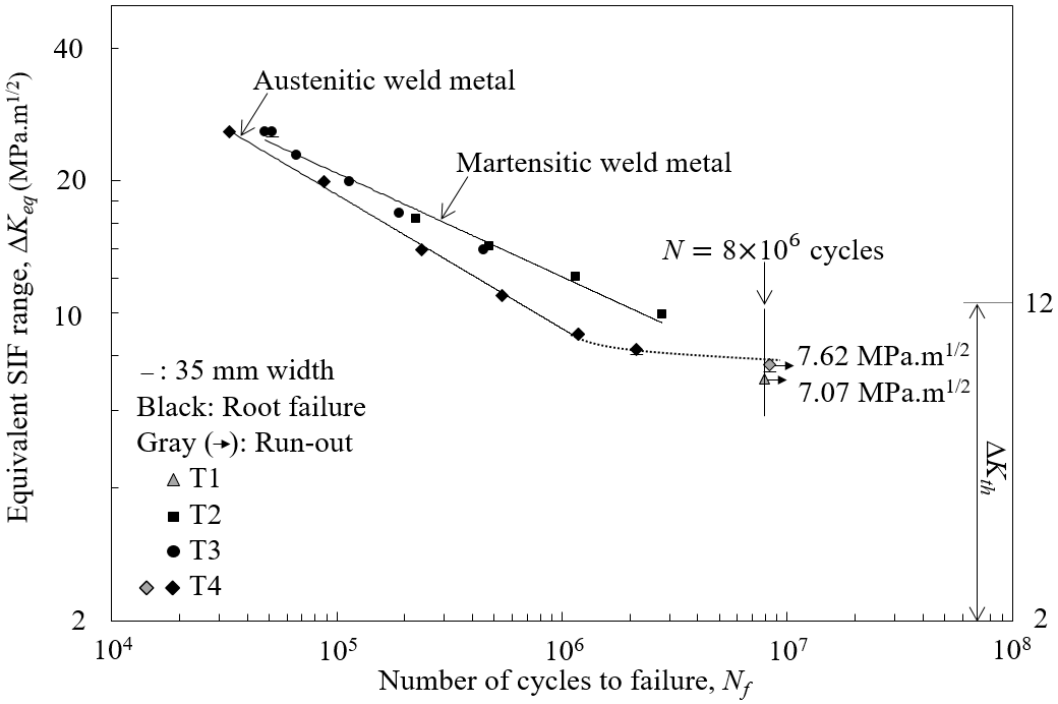

Figure 6.2: Effect of weld metals on the fatigue strengths by the N-SIF approach. The threshold SIF ranges for martensitic [64, 141] and austenitic [142-144] stainless steels are depicted

6.4 Fatigue crack growth behavior at the weld root

Fatigue cracking test is traditionally carried out on CT test specimens with standard geometry. CT specimens are highly constrained crack tips while in practice the weld root crack tip constraint of load-carrying cruciform fillet welded joints is different. Therefore, crack assessment is necessary to the fatigue crack propagation integrity analysis.

Figure 6.3 shows FCG behavior of T3 at $R = 0.1$ and 0.7. The crack lengths were measured from beach marked specimen at the lateral surface and in the middle of the fracture surface (Figure 4.9). The corresponding SIF range ΔK is calculated from the averaged $a - \Delta K_{eq}$ curve of symmetrical and dissymmetrical crack propagations for T3 (Figure 5.10). The applied stress ranges were 540 MPa at $R = 0.1$ and 180 MPa at $R = 0.7$. Crack length monitored at the lateral surface behaved almost similarly to that measured in the middle of the fracture surface. Hence, monitoring the crack length at the lateral surface is an appropriate technique to calculate FCGRs. For two load ratios,

the FCG behaviors of cruciform joint are compared with those measured for the CT specimen made from AISI 415 [65]. The cruciform joint at $R = 0.1$ demonstrates slightly lower FCGRs than those of CT specimen while it is almost similar at $R = 0.7$.

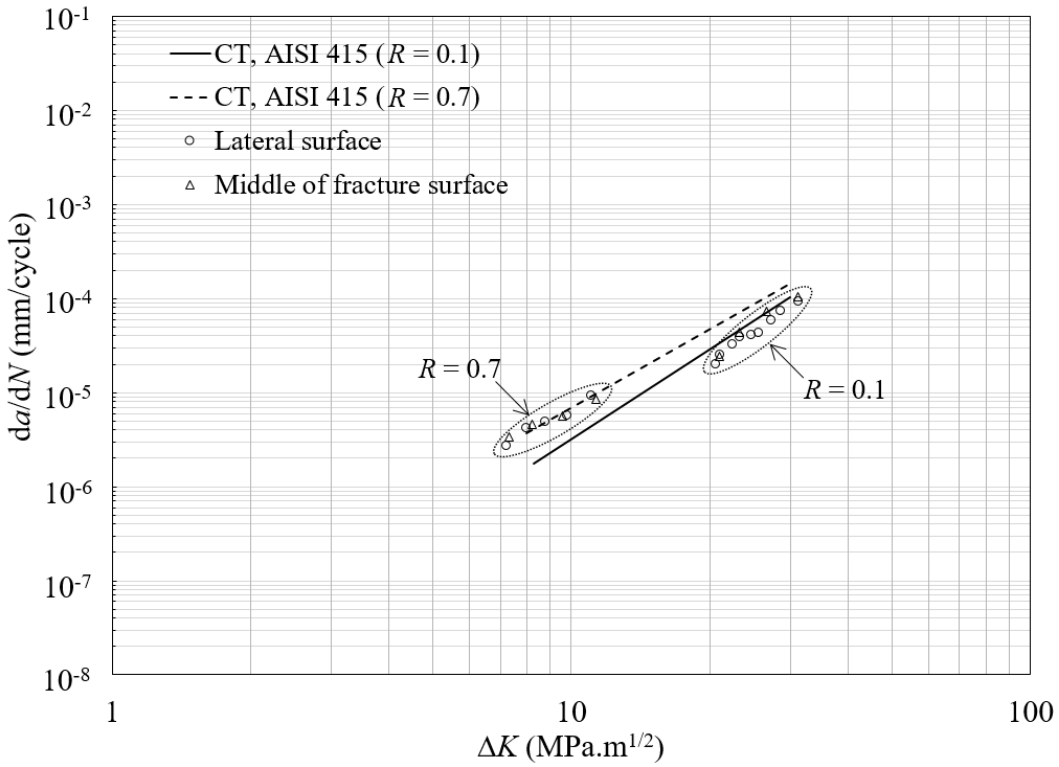

Figure 6.3: FCGR versus SIF range at $R = 0.1$ and 0.7 for cruciform joint and CT specimen [65]

At $R = 0.1,$ the scatter data of FCG behavior of T2 and T3 are presented in Figure 6.4 for different stress ranges. The leading crack lengths from Figure 4.10 and the averaged $a - \Delta K_{eq}$ curve of symmetrical and dissymmetrical crack propagations from Figure 5.10 are considered. The results are compared with FCG behavior of CT specimen made from AISI 415 [65]. The CT specimen closure measurements of AISI 415 at $R = 0.1$ indicated that the crack closure is considerable at a SIF range lower than 21 MPa.m$^{1/2}$ (Figure 2.3). At low SIF range, the FCGR scatter range of T2 and T3 is lower than CT specimen whereas at high SIF range, the FCGR scatter range of T2 and T3 approaches the CT specimen. The difference between FCGRs of cruciform joint and CT

specimen can be explained by the fatigue stress state variation at the crack tip and the crack closure intensity.

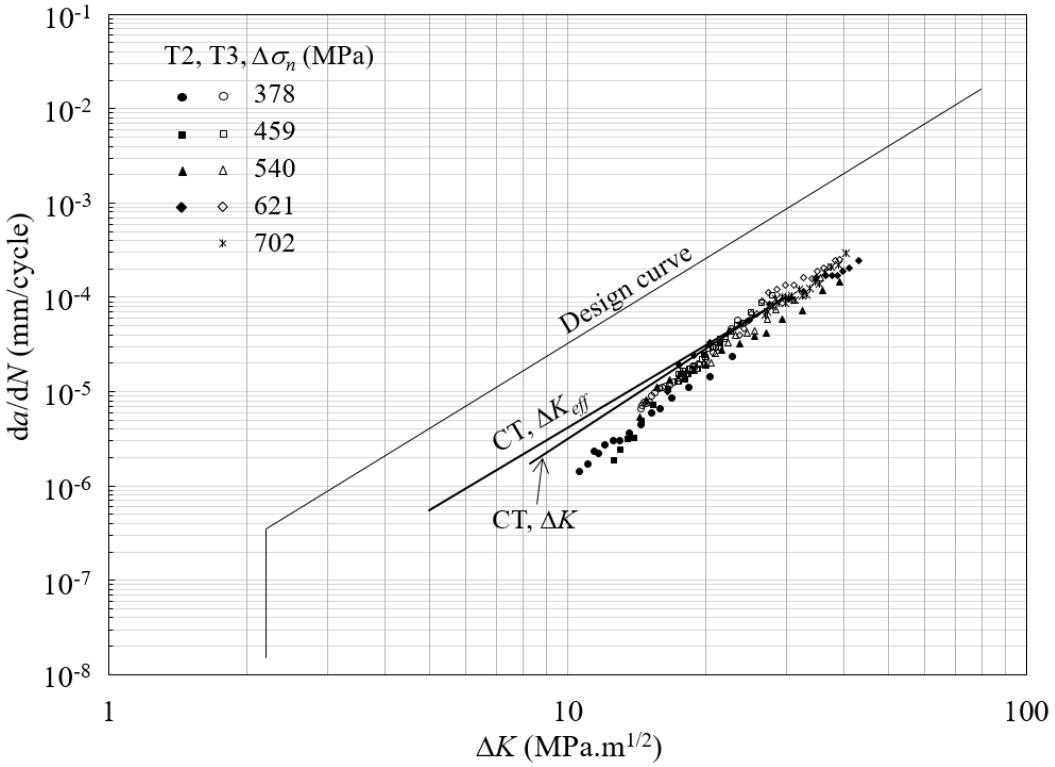

Figure 6.4: Comparison of FCG behavior at $R = 0.1$ for cruciform joint, CT specimen [65], and design curve [6]

The cruciform joints have negative stress biaxiality ratio while CT specimens present a positive value. For crack lengths in the range of $a/W = 0.2$ and 0.7, the stress biaxiality ratio is positive between 0.09 and 0.60 [40] (W is the width of the CT specimen). The stress biaxiality ratios for T2 and T3 are negative as presented in Table 5.4. The level of stress triaxiality at the crack tip is reduced by the negative (compression) non-singular T-stress and is strengthened by the positive (tension) non-singular T-stress [145]. Negative T-stress in a cruciform joint leads to loss of crack tip constraint while positive T-stress in a CT specimen leads to high crack tip constraint. Thus, the magnitude of triaxiality in cruciform joint is reduced with decreasing T-stress and this reduction can also diminish the FCGR.

The existence of the compressive welding residual stress in the vicinity of the weld root [111, 115] is another reason for the difference in FCGRs and that is favorable from a fatigue resistance point of view. The compressive residual stress can decrease the load ratio and therefore the FCGR. At lower SIF range, it tends to close the weld root crack opening, and the $K_{\min}$ is not high enough to overcome the closing effect. The compressive residual stress therefore can increase the magnitude of crack closure at the weld root of cruciform joint. Additionally, in the near threshold regime, the sliding crack surface interferences (roughness- and oxide-induced crack closure) are more pronounced under mixed-mode problem in cruciform joints.

As FCGRs of cruciform joints and CT specimens are similar at $R = 0.7$ and at high SIF range of $R = 0.1,$ the effects of negative T-stress and compressive welding residual stress are evidently insignificant. Turbine runners design methods use the conservative design curve presented in Figure 6.4 [6]. The conservative design curve has significantly higher FCGR than the ones observed in cruciform joint and CT specimen made from real material commonly used in the fabrication of turbine runners.

6.5 Fatigue life prediction at the weld root

The crack propagation approach has been employed for predicting the fatigue life at the weld root. During constant amplitude stressing $\Delta\sigma,$ SIF range increases with the crack length propagation (Figure 5.10). In addition, FCGR depends on the SIF range (Figure 6.4). The growth rate therefore is not constant and it increases with the crack increment. By integrating the Paris' power law [23], predicted number of cycles N_P can be eventually calculated from:

$$N_P = \int_{a_n}^{a_{n+1}} \frac{\mathrm{d}a}{C\, f(\Delta K, a)^m} \tag{6.1}$$

where a_n and a_{n+1} are start and end leading crack lengths, respectively; C and m are material constants of fatigue crack propagation of the CT specimen presented in Figure 6.3. $f(\Delta K, a)$ is the SIF range as a function of crack length. The averaged $a - \Delta K_{eq}$ curve is considered in the fatigue life calculation (Figure 5.10). Figure 6.5 shows the predicted number of cycles versus the actual

number of cycles for each block of beach marked specimen at $R = 0.1$ and 0.7. The results of crack lengths at the lateral surface and in the middle of the fracture surface are compared. The fatigue life prediction is more accurate when fatigue crack propagation parameters of the CT specimen at load ratio of 0.7 are introduced.

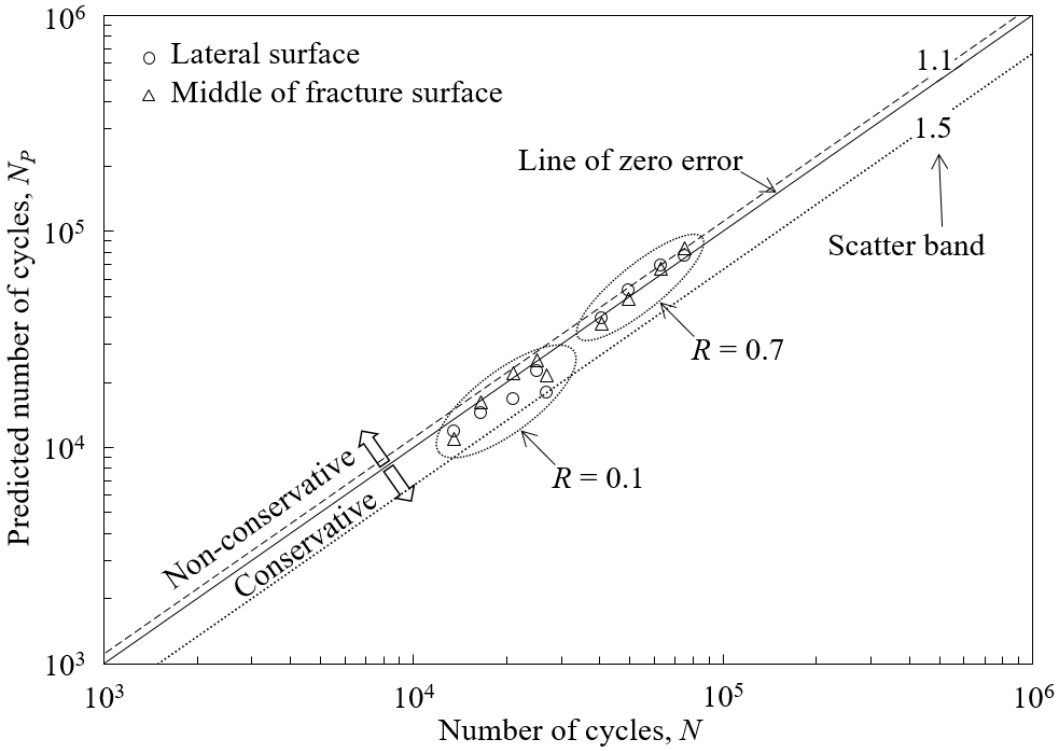

Figure 6.5: Predicted and actual number of cycles for each recorded crack increment

The entirety of the predicted number of cycles N_P for a specimen is calculated by the summation of crack initiation life N_i and crack propagation life N_p as:

$$N_P = N_i + N_p \tag{6.2}$$

The gap-tip at the weld root is significant enough to be considered as a crack-like defect (Table 4.2) and that the crack initiation life is negligible, $N_i \simeq 0$. The entirety of fatigue life of beach marked

specimen is therefore calculated by the summation of fatigue life of seven blocks of large and small cycles as:

$$N_P = \sum_{n=1}^{7}\left[\left(\int_{a_n}^{a_{n+1}} \frac{\mathrm{d}a}{C\,f(\Delta K,a)^m}\right)_{R=0.1} + \left(\int_{a_n}^{a_{n+1}} \frac{\mathrm{d}a}{C\,f(\Delta K,a)^m}\right)_{R=0.7}\right] \tag{6.3}$$

The predicted number of cycles shows the conservative scatter band of 1.1 for FCG behavior of CT specimen. The crack propagation approach is also implemented to predict the total fatigue lives for T2 and T3 specimens. As such:

$$N_P = \int_{a_i}^{a_f} \frac{\mathrm{d}a}{C\,f(\Delta K,a)^m} \tag{6.4}$$

For each specimen, initial and final leading crack lengths are listed in Table 4.1. Figure 6.6 shows the comparison of the predicted number of cycles and the actual number of cycles to failure for T2 and T3 specimens.

When using the fatigue crack propagation parameters of the CT specimen, the prediction method is meaningfully conservative at low SIF range for T2 and T3. As mentioned previously, the stress triaxiality at the crack tip was reduced by the negative *T*-stress. Furthermore, the $K_{\min}$ value is not high enough to overcome the closing effect induced by the compressive welding residual stress. Therefore, ignoring the effect of *T*-stress and welding residual stress would contribute to the overestimation of fatigue lives of weld root at low SIF range.

By using fatigue crack propagation parameters of design curve, the predicted number of cycles compared to the actual number of cycles is conservative from 7.6 up to 27.0 scatter bands. Thus, the use of the design curve reference of FCG behavior provides a conservative approach for predicting fatigue life in turbine runners.

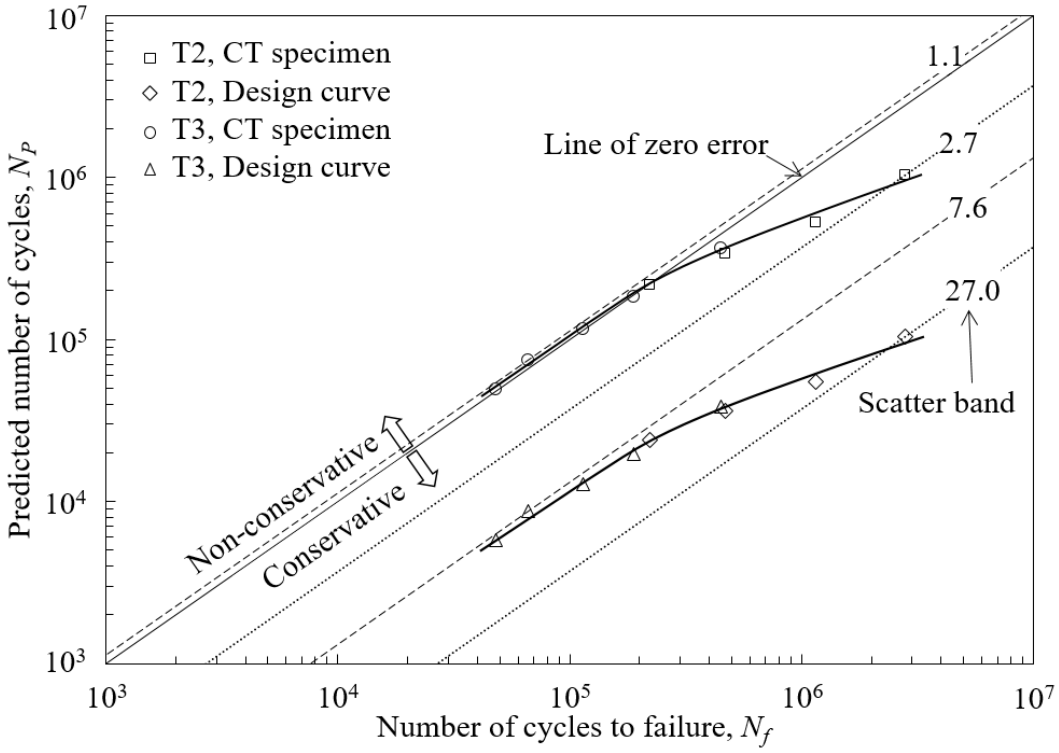

Figure 6.6: Predicted and actual number of cycles for T2 and T3 failures

CHAPTER 7 CONCLUSIONS AND RECOMMENDATIONS

7.1 Conclusions

This thesis studied the fatigue life of load-carrying cruciform joints with concave fillet weld (round weld toes) under three-point bending load, and performed fatigue life analysis on the weld root and toe cracking. The geometry was designed such that it enabled the investigation of the influence of the weld penetration depth and the weld metal of E410NiMo and E316L on fatigue strength. The cruciform joints were made of AISI 415 plates. The designed cruciform fillet welded joints are considered representative of the welded joints observed in turbine runners after fabrication while avoiding the influence of other factors such as the inclination of the blades. The particular partial joint penetration weld was manufactured under realistic conditions that are necessary to reproduce the turbine runners.

Moreover, a numerical study of the parameters influencing the accuracy of computed stress intensity factor (SIF) values was performed in this thesis. From the findings presented in this study, the following key conclusions can be drawn:

Fatigue life analysis

- Fatigue life at the weld toe demonstrates that the weld toe surface finish has a favorable effect on the crack initiation life of weld toe. Crack initiation life at the weld root shows that the gap-tip is significant enough to be considered as a crack-like defect.
- Owing to the initiation of a crack from surface, the weld toe failure in the *S–N* curve is widely scattered compared to the weld root failure at a crack-like defect.
- The weld root crack length not only has a significant effect on the SIF at the weld root, but also has a gradual effect on the SCF at the weld toe; the effect on the SCF at the weld toe is more notable when a smaller weld toe radius is introduced.

- The SIFs from British Standard for a load-carrying cruciform joint with flat face fillet welds under pure bending are larger than those computed for concave fillet welds under three-point bending.
- The negative inverse slope of the fatigue curve at the weld root (cracked member) is different from that at the weld toe (notched member).
- The fatigue test results indicated that the origin of fatigue failure changes with the weld penetration depth and the magnitude of the nominal bending stress range. For these particular specimens, there was potential for weld root failure at a low stress range, while the mode of failure changed to the weld toe for higher fatigue bending stress ranges.
- Owing to the effect of different weld penetration depths, the scatter of the experimental data of fatigue failure at the weld root is very pronounced in the *S–N* curve. The N-SIF approach can consolidate the *S–N* data of different weld penetration depths, and shows that the equivalent SIF range is an important contributing parameter in fatigue strength prediction.
- The welded joints made with martensitic weld metal E410NiMo have higher fatigue strengths than those made with austenitic weld metal E316L.

Crack propagation at the weld root

- Uniform through crack propagation (non semi-elliptical crack) was observed in a large region on the fracture surface of the weld root.
- Half fatigue life $N / N_f = 0.5$ is spent to merely propagate the crack by approximately 2 mm at the weld root. Thus, the effect of the first weld pass fatigue strength is significant in the total fatigue life at the weld root.
- At low SIF range of $R = 0.1,$ the FCGR of cruciform joints is lower than CT specimen. The negative *T*-stress at the weld root crack tip, the compressive welding residual stress in the vicinity of the weld root, and the crack closure intensity are the reasons for the reduction in FCGR of cruciform joints.

- At high SIF range of $R = 0.1,$ the FCGR of cruciform joints approaches that of the CT specimen. The effects of negative *T*-stress and compressive welding residual stress on FCGR are not pronounced. At $R = 0.7,$ the cruciform joints show similar FCGR value as that of the CT specimen.
- Crack propagation approach is a proper technique to predict the fatigue life of weld root crack when an appropriate FCG behavior is introduced and when there is no crack closure. The approach is conservative in the low SIF range owing to the difference in fatigue stress state and crack closure intensity.

Numerical computation of mode I and mode II SIFs

Comparison between the analytical calculation [72] and numerical simulation of the mode I SIF for a center crack under tension shows that:

- Mode I SIFs obtained with IIM are more accurate than those obtained with DEM.
- Adopting different quadratic element types in the body itself does not have a significant effect on the accuracy of the SIF calculated with either method.
- Angular discretization around the crack tip followed by the element size substantially affects the estimation of the K_I value. For element sizes of $a/8$ or less and a minimum of $n = 12$ elements (15° each), the percent difference obtained with DEM is less than +0.15. With IIM, the K_I value estimation is exact $(-0.01\% < e_K < +0.01\%)$ for element sizes of $a/6$ or less and a minimum of $n = 5$ elements (36° each).
- Local mesh refinement at lower mesh size ratios has a favorable effect on SIF calculation with DEM, while it slightly affects the accuracy of the SIF calculated with IIM. At larger mesh size ratios, there is no consistency in the estimated results for either method.
- Poisson's ratios from 0 to 0.4 slightly affect the SIFs estimated with DEM, but this variation in the Poisson's ratio does not have any effect on the exact estimation obtained with IIM at $L_B / L_T = 1$ and 5.

- The accuracies of the mode I SIFs obtained with both methods are not affected by crack length, except at high mesh size ratios.

Considering the recommendations made for the mode I SIF calculation, the assessment of mode I and mode II SIFs at the weld root of a load-carrying cruciform joint with a concave fillet weld under three-point bending shows that:

- IIM gives accurate SIFs for both modes at different crack lengths.
- The accuracy of the mode I SIF calculated with DEM is independent of the crack length, while that of the mode II SIF is highly dependent.

7.2 Recommendations for future work

This study has raised several questions in need of further research work. From the findings presented in this thesis, the following key recommendations can be given for future work:

- An experimental measurement and/or numerical calculation involving welding residual stress fields of weld root of different weld penetration depths is desired. This can be conducted on the geometry of cruciform fillet welded joint and real section of turbine runners welded joint. More information on the residual stress fields would help to establish a deeper understanding of fatigue failure mode transition and FCG behavior.
- It would be interesting to compare the fatigue lives of the similar geometry of load-carrying cruciform fillet welded joint free of any welding residual stresses with the ones presented in this study. An unfused section can be created in the root of a cruciform joint. The results could separate the effect of non-singular *T*-stress from welding residual stress fields on the FCG behavior.
- More research into PWHT effect on weld root residual stress field is still necessary before obtaining a definite answer to the question on whether or not the PWHT has a detrimental effect on the FCG behavior and fatigue life of weld root crack. Likewise, it would be interesting to assess the PWHT effect on weld toe residual stress field and understand whether it has favorable effect on the FCG behavior and fatigue life of weld toe. More tests on weld root and toe failures

of as-weld cruciform joint will be useful to verify the PWHT effect on the weld root and toe residual stress fields.

- Further research regarding the role of different loading configurations would be worthwhile. For instance, it would be interesting to assess the effects of multi-axial loading or tension loading on FCG behavior at the weld root and toe.

REFERENCES

[1] B. Papillon, J. L. Gagne, S. Giroux, and M. Sabourin, "Turbine rehabilitation: Chute-des-Passes case study," presented at the HydroVision, Portland, Oregon, 2002.

[2] K. H. Frank, "The fatigue strength of fillet welded connections," PhD Thesis, Lehigh University, Bethlehem, 1971.

[3] K. H. Frank and J. W. Fisher, "Fatigue strength of fillet welded cruciform joints," *Journal of the Structural Division,* vol. 105, pp. 1727-1740, 1979.

[4] M. Sabourin, J. L. Gagne, S. Giroux, A. St-Hilaire, and J. Terreault, "Mechanical loads and fatigue analysis of a francis runner," presented at the Hydrovision, Montreal, Canada, 2004.

[5] M. Gagnon, S. A. Tahan, P. Bocher, and D. Thibault, "Impact of startup scheme on Francis runner life expectancy," presented at the 25th IAHR Symposium on Hydraulic Machinery and Systems, IOP Conference Series: Earth and Environmental Science, 2010.

[6] M. Sabourin, D. Thibault, D.-A. Bouffard, and M. Lévesque, "New Parameters Influencing Hydraulic Runner Lifetime," presented at the 25th IAHR Symposium on Hydraulic Machinery and Systems, Timisoara, Romania, 2010.

[7] M. Sabourin, D. Bouffard, and F. Paquet, "Runners Experience Longer Life," *Ansys Advantage,* vol. II, pp. 25-26, 2008.

[8] J. Lanteigne, M. Sabourin, T. Bui-Quoc, and D. Julien, "The Characteristics of the Steels used in Hydraulic Turbine runners," presented at the 24th IAHR Symposium on Hydraulic Machinery and Systems, Foz Do Iguassu, Brazil, 2008.

[9] ASTM E647, "Standard Test Method for Measurement of Fatigue Crack Growth Rates," ed: American Society for Testing and Materials, 2015.

[10] A. Wöhler, "Versuche über die Festigkeit der Eisenbahnwagen Achsen (Experiments on the stability of the railroad car axles)," *Zeitschrift für Bauwesen,* vol. 10, 1860 (in German).

[11] O. H. Basquin, "The exponential law of endurance tests," presented at the Proc. American Society for Testing Materials, 1910.

[12] A. Hobbacher, "The new IIW recommendations for fatigue assessment of welded joints and components–A comprehensive code recently updated," *International Journal of Fatigue,* vol. 31, pp. 50-58, 2009.

[13] A. Hobbacher, *Recommendations for fatigue design of welded joints and components*: Springer International Publishing, 2016.

[14] A. F. Hobbacher, "New developments at the recent update of the IIW recommendations for fatigue of welded joints and components," *Steel Construction,* vol. 3, pp. 231-242, 2010.

[15] M. L. Williams, "Stress singularities resulting from various boundary conditions in angular corners of plates in extension," *Journal of Applied Mechanics,* vol. 19, pp. 526-528, 1952.

[16] G. R. Irwin, "Analysis of stresses and strains near the end of a crack traversing a plate," *Journal of Applied Mechanics,* vol. 24, pp. 361-364, 1957.

[17] D. Radaj, "Stress singularity, notch stress and structural stress at spot-welded joints," *Engineering Fracture Mechanics,* vol. 34, pp. 495-506, 1989.

[18] Y. Verreman and B. Nie, "Early development of fatigue cracking at manual fillet welds," *Fatigue & Fracture of Engineering Materials & Structures,* vol. 19, pp. 669-681, 1996.

[19] T. Boukharouba, T. Tamine, L. Niu, C. Chehimi, and G. Pluvinage, "The use of notch stress intensity factor as a fatigue crack initiation parameter," *Engineering Fracture Mechanics,* vol. 52, pp. 503-512, 1995.

[20] R. Yuuki, T. Ohira, H. Nakatsukasa, and W. Yi, "Fracture mechanics analysis and evaluation of the fatigue strength of spot welded joints," *Transactions of the Japan Society of Mechanical Engineers, Series A,* vol. 51, pp. 1772-1779, 1985 (in Japanese).

[21] P. Lazzarin and R. Tovo, "A notch intensity factor approach to the stress analysis of welds," *Fatigue & Fracture of Engineering Materials & Structures,* vol. 21, pp. 1089-1103, 1998.

[22] P. Lazzarin and P. Livieri, "Notch stress intensity factors and fatigue strength of aluminium and steel welded joints," *International journal of fatigue,* vol. 23, pp. 225-232, 2001.

[23] P. C. Paris and F. Erdogan, "A critical analysis of crack propagation laws," *Transactions of the ASME, Journal of Basic Engineering,* pp. 528-534, 1963.

[24] W. Fricke, "IIW guideline for the assessment of weld root fatigue," *Welding in the World,* vol. 57, pp. 753-791, 2013.

[25] W. Elber, "Fatigue crack closure under cyclic tension," *Engineering Fracture Mechanics,* vol. 2, pp. 37-45, 1970.

[26] W. Elber, "The significance of fatigue crack closure," *Damage Tolerance in Aircraft Structures, ASTM STP 486,* pp. 230-242, 1971.

[27] M.-L. Zhu, F.-Z. Xuan, and S.-T. Tu, "Effect of load ratio on fatigue crack growth in the near-threshold regime: A literature review, and a combined crack closure and driving force approach," *Engineering Fracture Mechanics,* vol. 141, pp. 57-77, 2015.

[28] N. Walker and C. Beevers, "A fatigue crack closure mechanism in titanium," *Fatigue & Fracture of Engineering Materials & Structures,* vol. 1, pp. 135-148, 1979.

[29] P. Paris, R. Bucci, E. Wessel, W. Clark, and T. Mager, "Extensive study of low fatigue crack growth rates in A533 and A508 steels," in *Stress Analysis and Growth of Cracks: Proceedings of the 1971 National Symposium on Fracture Mechanics: Part 1*, 1972.

[30] R. Pippan and A. Hohenwarter, "Fatigue crack closure: a review of the physical phenomena," *Fatigue & fracture of engineering materials & structures,* vol. 40, pp. 471-495, 2017.

[31] A. F. Blom and D. K. Holm, "An experimental and numerical study of crack closure," *Engineering Fracture Mechanics,* vol. 22, pp. 997-1011, 1985.

[32] D. L. Davidson, "Fatigue crack closure," *Engineering Fracture Mechanics,* vol. 38, pp. 393-402, 1991.

[33] A. Vasudeven, K. Sadananda, and N. Louat, "A review of crack closure, fatigue crack threshold and related phenomena," *Materials Science and Engineering: A,* vol. 188, pp. 1-22, 1994.

[34] A. J. McEvily, "On crack closure in fatigue crack growth," in *Mechanics of fatigue crack closure*, ed: ASTM International, 1988.

[35] N. Louat, K. Sadananda, M. Duesbery, and A. Vasudevan, "A theoretical evaluation of crack closure," *Metallurgical Transactions A,* vol. 24, pp. 2225-2232, 1993.

[36] R. Pippan, F. Riemelmoser, H. Weinhandl, and H. Kreuzer, "Plasticity-induced crack closure under plane-strain conditions in the near-threshold regime," *Philosophical Magazine A,* vol. 82, pp. 3299-3309, 2002.

[37] J. K. Donald, R. G. Pettit, and M. A. James, "Crack Size and Shape Considerations Related to Near-Threshold Fatigue Crack Growth Rate Behavior," *Materials Performance and Characterization,* vol. 7, 2018.

[38] M. L. Williams, "On the stress distribution at the base of a stationary crack," *Journal of Applied Mechanics,* vol. 24, pp. 109-114, 1957.

[39] S. G. Larsson and A. J. Carlsson, "Influence of non-singular stress terms and specimen geometry on small-scale yielding at crack tips in elastic-plastic materials," *Journal of the Mechanics and Physics of Solids,* vol. 21, pp. 263-277, 1973.

[40] P. S. Leevers and J. C. Radon, "Inherent stress biaxiality in various fracture specimen geometries," *International Journal of Fracture,* vol. 19, pp. 311-325, 1982.

[41] M. H. Meliani, Z. Azari, G. Pluvinage, and Y. G. Matvienko, "The effective T-stress estimation and crack paths emanating from U-notches," *Engineering Fracture Mechanics,* vol. 77, pp. 1682-1692, 2010.

[42] J. Tong, "T-stress and its implications for crack growth," *Engineering Fracture Mechanics,* vol. 69, pp. 1325-1337, 2002.

[43] N. A. Fleck, "Finite element analysis of plasticity-induced crack closure under plane strain conditions," *Engineering Fracture Mechanics,* vol. 25, pp. 441-449, 1986.

[44] P. Hutař, S. Seitl, and Z. Knésl, "Effect of constraint on fatigue crack propagation near threshold in medium carbon steel," *Computational materials science,* vol. 37, pp. 51-57, 2006.

[45] Z. Knésl, S. Seitl, and P. Hutar, "Accounting for effects of constraint on propagation of a fatigue crack," *WIT Transactions on Engineering Sciences,* vol. 37, 2002.

[46] I. Varfolomeev, M. Luke, and M. Burdack, "Effect of specimen geometry on fatigue crack growth rates for the railway axle material EA4T," *Engineering Fracture Mechanics,* vol. 78, pp. 742-753, 2011.

[47] M. Ayatollahi, M. R. Moghaddam, and F. Berto, "T-stress effects on fatigue crack growth–Theory and experiment," *Engineering Fracture Mechanics,* vol. 187, pp. 103-114, 2018.

[48] M. Aliha and H. Gharehbaghi, "The effect of combined mechanical load/welding residual stress on mixed mode fracture parameters of a thin aluminum cracked cylinder," *Engineering Fracture Mechanics,* vol. 180, pp. 213-228, 2017.

[49] A. Parker, "Stress intensity factors, crack profiles, and fatigue crack growth rates in residual stress fields," in *Residual stress effects in fatigue*, ed: ASTM International, 1982.

[50] Y. E. Ma, P. Staron, T. Fischer, and P. E. Irving, "Size effects on residual stress and fatigue crack growth in friction stir welded 2195-T8 aluminium–Part II: Modelling," *International Journal of Fatigue,* vol. 33, pp. 1426-1434, 2011.

[51] M. Beghini and L. Bertini, "Fatigue crack propagation through residual stress fields with closure phenomena," *Engineering Fracture Mechanics,* vol. 36, pp. 379-387, 1990.

[52] H.-Y. Li, K.-W. Xu, N.-S. Hu, and J.-W. He, "Improvement of short fatigue crack growth model in the residual stress field," in *Computer Methods and Experimental Measurements for Surface Treat*. vol. 8, ed: WIT Transactions on Engineering Sciences, 1995, p. 8.

[53] J. J. Newman, "A crack opening stress equation for fatigue crack growth," *International Journal of fracture,* vol. 24, pp. R131-R135, 1984.

[54] L. R. Link, "Fatigue crack growth of weldments," in *Fatigue and fracture testing of weldments*, ed: ASTM International, STP 1058, 1990, pp. 16-33.

[55] H. Li, H. Sun, P. Bowen, and J. Knott, "Effects of compressive residual stress on short fatigue crack growth in a nickel-based superalloy," *International Journal of Fatigue,* vol. 108, pp. 53-61, 2018.

[56] A. Chernyatin, Y. G. Matvienko, and I. Razumovsky, "Fatigue surface crack propagation and intersecting cracks in connection with welding residual stresses," *Fatigue & Fracture of Engineering Materials & Structures,* 2018.

[57] ASTM A743/A743M, "Standard Specification for Castings, Iron-Chromium, Iron-Chromium-Nickel, Corrosion Resistant, for General Application," ed: American Society for Testing and Materials, 2013.

[58] ASTM A240/A240M, "Standard Specification for Chromium and Chromium-Nickel Stainless Steel Plate, Sheet, and Strip for Pressure Vessels and for General Applications," ed: American Society for Testing and Materials, 2016.

[59] AWS A5.22/A5.22M, "Specification for Stainless Steel Flux Cored and Metal Cored Welding Electrodes and Rods," ed: An American National Standard, 2010.

[60] M. Sabourin, B. Papillon, and L. Mathieu, "Francis runner fabrication process: the corner stone of power plant reliability," presented at the Hydrovision, Montreal, Canada, 2004.

[61] J. Lanteigne, M. Sabourin, T. Bui-Quoc, and D. Julien, "A comprehensive research programme on crack propagation characteristics of the base material used in hydraulic turbine runners," presented at the Waterpower XV, Chattanooga, USA, 2007.

[62] J. Chaix, "Influence de la température de revenu sur la résistance du CA6NM à la propagation des fissures de fatigue," MSc thesis, École Polytechnique de Montréal, 2014 (in French).

[63] A. Akhiate, "Effet de la teneur en carbone sur la résistance du CA6NM à la propagation des fissures de fatigue," MSc thesis, École Polytechnique de Montréal, 2015 (in French).

[64] A. Trudel, "Étude expérimentale de la propagation de fissures de fatigue dans la zone affectée thermiquement de joints soudés de roues de turbines hydrauliques," MSc thesis, École Polytechnique de Montréal, 2013 (in French).

[65] P.-A. Deschênes, "Comportement des fissures de fatigue dans un champ de contraintes résiduelles de tension," MSc thesis, École Polytechnique de Montréal, 2016 (in French).

[66] S. Roychowdhury and R. Dodds, "Effect of T-stress on fatigue crack closure in 3-D small-scale yielding," *International Journal of Solids and Structures,* vol. 41, pp. 2581-2606, 2004.

[67] K. Solanki, S. Daniewicz, and J. C. Newman, "Finite element analysis of plasticity-induced fatigue crack closure: an overview," *Engineering Fracture Mechanics,* vol. 71, pp. 149-171, 2004.

[68] J. T. Al-Haidary, A. A. Wahab, and E. H. Abdul Salam, "Fatigue crack propagation in austenitic stainless steel weldments," *Metallurgical and Materials Transactions A,* vol. 37, pp. 3205-3214, 2006.

[69] Y. Murakami, *Stress intensity factors handbook*: Pergamon Press, 1987.

[70] H. Tada, P. C. Paris, and G. R. Irwin, *The stress analysis of cracks handbook*, Third ed.: ASME Press, 2000.

[71] BS 7910, "Guide to methods for assessing the acceptability of flaws in metallic structures," ed: British Standard Institution, 2005.

[72] M. Isida, "Effect of width and length on stress intensity factors of internally cracked plates under various boundary conditions," *International Journal of Fracture Mechanics,* vol. 7, pp. 301-316, 1971.

[73] M. Aliha, H. Gharehbaghi, and R. Ghafoori Ahangar, "Fracture Study of a Welded Aluminum Cylinder Containing Longitudinal Crack and Subjected to Combined Residual Stress and Internal Pressure," presented at the 12th International Aluminum Conference, Paper No. 62, Montreal, Canada, 2013.

[74] S. Chan, I. Tuba, and W. Wilson, "On the finite element method in linear fracture mechanics," *Engineering Fracture Mechanics,* vol. 2, pp. 1-17, 1970.

[75] I. Raju and J. Newman Jr, "Three dimensional finite-element analysis of finite-thickness fracture specimens," 1977.

[76] R. S. Barsoum, "Application of quadratic isoparametric finite elements in linear fracture mechanics," *International Journal of Fracture,* vol. 10, pp. 603-605, 1974.

[77] C. Shih, H. De Lorenzi, and M. German, "Crack extension modeling with singular quadratic isoparametric elements," *International Journal of Fracture,* vol. 12, pp. 647-651, 1976.

[78] G. V. Guinea, J. Planas, and M. Elices, "KI evaluation by the displacement extrapolation technique," *Engineering Fracture Mechanics,* vol. 66, pp. 243-255, 2000.

[79] Q. Han, Y. Wang, Y. Yin, and D. Wang, "Determination of stress intensity factor for mode I fatigue crack based on finite element analysis," *Engineering Fracture Mechanics,* vol. 138, pp. 118-126, 2015.

[80] E. Byskov, "The calculation of stress intensity factors using the finite element method with cracked elements," *International Journal of Fracture Mechanics,* vol. 6, pp. 159-167, 1970.

[81] D. R. J. Owen and A. J. Fawkes, *Engineering fracture mechanics: numerical methods and applications*. Swansea, UK: Pineridge Press, 1983.

[82] R. S. Barsoum, "On the use of isoparametric finite elements in linear fracture mechanics," *International journal for numerical methods in engineering,* vol. 10, pp. 25-37, 1976.

[83] P. C. Paris and G. C. Sih, "Stress analysis of cracks," *Fracture toughness testing and its applications, ASTM STP381,* pp. 30-83, 1965.

[84] H. G. DeLorenzi, "Energy release rate calculations by the finite element method," *Engineering Fracture Mechanics,* vol. 21, pp. 129-143, 1985.

[85] V. B. Watwood Jr, "The finite element method for prediction of crack behavior," *Nuclear Engineering and Design,* vol. 11, pp. 323-332, 1969.

[86] T. K. Hellen, "On the method of virtual crack extensions," *International journal for numerical methods in engineering,* vol. 9, pp. 187-207, 1975.

[87] D. M. Parks, "The virtual crack extension method for nonlinear material behavior," *Computer Methods in Applied Mechanics and Engineering,* vol. 12, pp. 353-364, 1977.

[88] J. R. Rice, "A path independent integral and the approximate analysis of strain concentration by notches and cracks," *Transactions of the ASME, Journal of Applied Mechanics,* pp. 379-386, 1968.

[89] C. Shih, B. Moran, and T. Nakamura, "Energy release rate along a three-dimensional crack front in a thermally stressed body," *International Journal of Fracture,* vol. 30, pp. 79-102, 1986.

[90] J. F. Yau, S. S. Wang, and H. T. Corten, "A mixed-mode crack analysis of isotropic solids using conservation laws of elasticity," *Transactions of the ASME, Journal of Applied Mechanics,* vol. 47, pp. 335-341, 1980.

[91] S. Courtin, C. Gardin, G. Bezine, and H. B. H. Hamouda, "Advantages of the J-integral approach for calculating stress intensity factors when using the commercial finite element software ABAQUS," *Engineering Fracture Mechanics,* vol. 72, pp. 2174-2185, 2005.

[92] G. Qian, V. González-Albuixech, M. Niffenegger, and E. Giner, "Comparison of KI calculation methods," *Engineering Fracture Mechanics,* vol. 156, pp. 52-67, 2016.

[93] B. Zafošnik and G. Fajdiga, "Determining stress intensity factor KI with extrapolation method," *Technical Gazette,* vol. 23, pp. 1673-1678, 2016.

[94] I. Lim, I. Johnston, and S. Choi, "Comparison between various displacement-based stress intensity factor computation techniques," *International Journal of Fracture,* vol. 58, pp. 193-210, 1992.

[95] X.-K. Zhu and B. N. Leis, "Effective Methods to Determine Stress Intensity Factors for 2D and 3D Cracks," in *Proceedings of the ASME2014 10th International Pipeline Conference, IPC2014*, Calgary, Alberta, Canada, 2014.

[96] ANSYS. (2013). *Academic–Structural analysis Guide, Chapter 12: Fracture Mechanics, Release 14.5*.

[97] ABAQUS. (2012). *Analysis user's manual, Dassault Systémes Simulia Corporation, Version 6.12*.

[98] L. Banks-Sills and D. Sherman, "Comparison of methods for calculating stress intensity factors with quarter-point elements," *International Journal of Fracture,* vol. 32, pp. 127-140, 1986.

[99] P. Fu, S. M. Johnson, R. R. Settgast, and C. R. Carrigan, "Generalized displacement correlation method for estimating stress intensity factors," *Engineering Fracture Mechanics,* vol. 88, pp. 90-107, 2012.

[100] D. Radaj, "Review of fatigue strength assessment of nonwelded and welded structures based on local parameters," *International Journal of Fatigue,* vol. 18, pp. 153-170, 1996.

[101] W. Fricke, "Fatigue analysis of welded joints: state of development," *Marine structures,* vol. 16, pp. 185-200, 2003.

[102] S. Maddox, "Review of fatigue assessment procedures for welded aluminium structures," *International Journal of Fatigue,* vol. 25, pp. 1359-1378, 2003.

[103] M. Chryssanthopoulos and T. Righiniotis, "Fatigue reliability of welded steel structures," *Journal of Constructional Steel Research,* vol. 62, pp. 1199-1209, 2006.

[104] K. Nielsen, "Crack Propagation in Cruciform Welded Joints: Study of Modern Analysis," ed, 2011.

[105] W. Fricke and O. Doerk, "Simplified approach to fatigue strength assessment of fillet-welded attachment ends," *International journal of fatigue,* vol. 28, pp. 141-150, 2006.

[106] W. Fricke, A. Kahl, and H. Paetzold, "Fatigue assessment of root cracking of fillet welds subject to throat bending using the structural stress approach," *Welding in the World,* vol. 50, pp. 64-74, 2006.

[107] S. J. Maddox, "Assessing the significance of flaws in welds subject to fatigue," *Welding Journal,* vol. 53, pp. 401-409, 1974.

[108] S. Xing, P. Dong, and A. Threstha, "Analysis of fatigue failure mode transition in load-carrying fillet-welded connections," *Marine Structures,* vol. 46, pp. 102-126, 2016.

[109] W. Song, X. Liu, F. Berto, P. Wang, J. Xu, and H. Fang, "Strain energy density based fatigue cracking assessment of load-carrying cruciform welded joints," *Theoretical and Applied Fracture Mechanics,* vol. 90, pp. 142-153, 2017.

[110] S. Xing, P. Dong, and P. Wang, "A quantitative weld sizing criterion for fatigue design of load-carrying fillet-welded connections," *International journal of fatigue,* vol. 101, pp. 448-458, 2017.

[111] S. Kainuma and T. Mori, "A study on fatigue crack initiation point of load-carrying fillet welded cruciform joints," *International journal of fatigue,* vol. 30, pp. 1669-1677, 2008.

[112] Y. Dong and C. Guedes Soares, "On the fatigue crack initiation point of load-carrying fillet welded joints," *Towards Green Marine Technology and Transport,* pp. 407-416, 2015.

[113] V. Balasubramanian and B. Guha, "Establishing criteria for root and toe cracking of load carrying cruciform joints of pressure vessel grade steel," *Engineering Failure Analysis,* vol. 11, pp. 967-974, 2004.

[114] T. R. Gurney and K. MacDonald, *Literature Survey on Fatigue Strengths of Load-Carrying Fillet Welded Joints Failing in the Weld*: Citeseer, 1995.

[115] Z. Barsoum and A. Lundbäck, "Simplified FE welding simulation of fillet welds–3D effects on the formation residual stresses," *Engineering Failure Analysis,* vol. 16, pp. 2281-2289, 2009.

[116] Z. Barsoum, "Residual stress analysis and fatigue of multi-pass welded tubular structures," *Engineering Failure Analysis,* vol. 15, pp. 863-874, 2008.

[117] G. Meneghetti, "The use of peak stresses for fatigue strength assessments of welded lap joints and cover plates with toe and root failures," *Engineering Fracture Mechanics,* vol. 89, pp. 40-51, 2012.

[118] R. E. Peterson, *Stress concentration factors*: John Willey & Sons, 1974.

[119] N. E. Dowling, *Mechanical behavior of materials*, 4th ed.: Pearson Education, 2013.

[120] J. T. P. d. Castro, M. A. Meggiolaro, A. C. d. O. Miranda, H. Wu, A. Imad, and N. Benseddiq, "Prediction of fatigue crack initiation lives at elongated notch roots using short crack concepts," *International journal of fatigue,* vol. 42, pp. 172-182, 2012.

[121] J. E. Noblett and R. M. Andrews, "A stress intensity factor solution for root defects in fillet and partial penetration welds," in *Fatigue: Core Research from TWI*, G. Cho, Ed., ed: Abington Publishing, 2000, pp. 120-144.

[122] A. K. Motarjemi, A. Kokabi, A. Ziaie, S. Manteghi, and F. Burdekin, "Comparison of the stress intensity factor of T and cruciform welded joints with different main and attachment plate thickness," *Engineering Fracture Mechanics,* vol. 65, pp. 55-66, 2000.

[123] J. M. Djoković and R. R. Nikolić, "Influence of the Joint Geometry on the Stress Intensity Factor of the Fillet Welded Cruciform Joint Subjected to Tension and Bending," *Materials Today: Proceedings,* vol. 3, pp. 959-964, 2016.

[124] S. J. Maddox, "Status review on fatigue performance of fillet welds," *Journal of Offshore Mechanics and Arctic Engineering,* vol. 130, pp. 1-10, 2008.

[125] M. M. Amrei, H. Monajati, D. Thibault, Y. Verreman, L. Germain, and P. Bocher, "Microstructure characterization and hardness distribution of 13Cr4Ni multipass weld metal," *Materials Characterization,* vol. 111, pp. 128-136, 2016.

[126] F. Foroozmehr, "Ductile Fracture of 13% Cr-4% Ni Martensitic Stainless Steels Used in Hydraulic Turbine Welded Runners," MSc thesis, École Polytechnique de Montréal, 2017.

[127] Y. Verreman, "Comportement en fatigue des joints soudés automatiques," PhD thesis, École Polytechnique de Montréal, Montreal, Canada, 1985 (in French).

[128] E. Moisan, M. Sabourin, M. Bernard, and T. Bui-Quoc, "Residual Stress Measurements in Hydraulic Turbine Welded Joints," presented at the 23rd IAHR Symposium on Hydraulic Machinery and Systems, Yokohama, Japan, 2006.

[129] D. Wang, H. Zhang, B. Gong, and C. Deng, "Residual stress effects on fatigue behaviour of welded T-joint: a finite fracture mechanics approach," *Materials & Design,* vol. 91, pp. 211-217, 2016.

[130] Hydro-Québec, "Scompi Robot: Robotic system for generating station work <http://www.hydroquebec.com/innovation/en/pdf/2010G080-18A-SCOMPI.pdf>," 4959 523 B1 US Patent, 2011.

[131] BS EN ISO 13916, "Welding–Measurement of preheating temperature, interpass temperature and preheat maintenance temperature," ed: British Standard Institution, 2017.

[132] CSA W59-13, "Welded Steel Construction (Metal Arc Welding)," ed: Canadian Standards Association, 2015.

[133] ASME Boiler and Pressure Vessel Code, "Section VIII-Rules for Construction of Pressure Vessels Division 1," ed: American Society of Mechanical Engineers, 2013.

[134] D. Thibault, P. Bocher, M. Thomas, M. Gharghouri, and M. Côté, "Residual stress characterization in low transformation temperature 13%Cr–4%Ni stainless steel weld by neutron diffraction and the contour method," *Materials Science and Engineering: A,* vol. 527, pp. 6205-6210, 2010.

[135] W. Shen, R. Yan, N. Barltrop, M. Song, and E. Liu, "Fatigue crack growth analysis of T junction under biaxial compressive–compressive loads," *Engineering Fracture Mechanics,* vol. 154, pp. 207-224, 2016.

[136] R. Ghafoori Ahangar and Y. Verreman, "Assessment of mode I and mode II stress intensity factors obtained by displacement extrapolation and interaction integral methods," *Journal of Failure Analysis and Prevention,* vol. 19, 2019.

[137] M. R. Ayatollahi, M. J. Pavier, and D. J. Smith, "Determination of T-stress from finite element analysis for mode I and mixed mode I/II loading," *International Journal of Fracture,* vol. 91, pp. 283-298, 1998.

[138] B. Yang and K. Ravi-Chandar, "Evaluation of elastic T-stress by the stress difference method," *Engineering Fracture Mechanics,* vol. 64, pp. 589-605, 1999.

[139] M. L. Roessle and A. Fatemi, "Strain-controlled fatigue properties of steels and some simple approximations," *International journal of fatigue,* vol. 22, pp. 495-511, 2000.

[140] B. L. da Silva, J. de Almeida Ferreira, F. Oliveira, and J. Araújo, "Influence of mean stress on the fatigue strength of ASTM A743 CA6NM alloy steel," *Frattura ed Integrità Strutturale,* p. 17, 2010.

[141] D. Thibault, P. Bocher, M. Thomas, J. Lanteigne, P. Hovington, and P. Robichaud, "Reformed austenite transformation during fatigue crack propagation of 13% Cr–4% Ni stainless steel," *Materials Science and Engineering: A,* vol. 528, pp. 6519-6526, 2011.

[142] C. S. Kusko, J. N. Dupont, and A. R. Marder, "The influence of microstructure on fatigue crack propagation behavior of stainless steel welds," *Welding Journal,* vol. 83, pp. 6-14, 2004.

[143] B. Kim, J. Lee, J. Im, J. Kim, M. Kim, H. Kim*, et al.*, "Effect of sigma phase on near-threshold fatigue crack growth behavior and ultrasonic evaluation in AISI 316L stainless steel," *Journal of Mechanical Science and Technology,* vol. 26, pp. 3091-3096, 2012.

[144] N. Noraphaiphipaksa, T. Putta, A. Manonukul, and C. Kanchanomai, "Interaction of plastic zone, pores, and stress ratio with fatigue crack growth of sintered stainless steel," *International Journal of Fracture,* vol. 176, pp. 25-38, 2012.

[145] M. H. Meliani, Z. Azari, G. Pluvinage, and Y. G. Matvienko, "Two Parameter Engineering Fracture Mechanics: calculation of the relevant parameters and investigation of their influence on the surface notch," in *Integrity of Pipelines Transporting Hydrocarbons*, ed: Springer, 2011, pp. 245-274.

APPENDIX A – NUMERICAL METHODS FOR SIF CALCULATION

A.1 Displacement extrapolation method

The SIF is calculated from the direct relationship between the K value and the near-crack tip displacements. For linear elastic materials, the analytical expressions for the displacement (u, v) of nodes parallel and perpendicular to the crack growth direction (Figure 2.5) were given by Paris and Sih (1965) [83] as follows:

$$u = \frac{K_I}{4G}\sqrt{\frac{r}{2\pi}}\left[(2\kappa-1)\cos\frac{\theta}{2}-\cos\frac{3\theta}{2}\right]+\frac{K_{II}}{4G}\sqrt{\frac{r}{2\pi}}\left[(2\kappa+3)\sin\frac{\theta}{2}+\sin\frac{3\theta}{2}\right]+O(r)$$
$$v = \frac{K_I}{4G}\sqrt{\frac{r}{2\pi}}\left[(2\kappa+1)\sin\frac{\theta}{2}-\sin\frac{3\theta}{2}\right]-\frac{K_{II}}{4G}\sqrt{\frac{r}{2\pi}}\left[(2\kappa-3)\cos\frac{\theta}{2}+\cos\frac{3\theta}{2}\right]+O(r) \quad \text{(A.1)}$$

where K_I and K_{II} are the mode I and mode II SIFs, respectively; G is the shear modulus; r and θ are the local polar coordinates with the origin at the crack tip; κ is an elastic parameter equal to $(3-\nu)/(1+\nu)$ and $(3-4\nu)$ for plane stress and plane strain conditions, respectively; ν is the Poisson's ratio; and $O(r)$ represents terms of order r or higher which can be neglected when $r \to 0$. The expression can be simplified along the free crack faces $(\theta = \pi)$ by defining the following:

$$K_{II} = \lim_{r\to 0}\left[\sqrt{2\pi}\,\frac{2G}{\kappa+1}\,\frac{u}{\sqrt{r}}\right]$$
$$K_I = \lim_{r\to 0}\left[\sqrt{2\pi}\,\frac{2G}{\kappa+1}\,\frac{v}{\sqrt{r}}\right] \quad \text{(A.2)}$$

The SIF at the crack tip is thus extrapolated from the numerically calculated displacements in the vicinity from the crack tip to $r = 0$. This method requires a good numerical representation of the crack tip field with finer meshes. To represent the singular strain field at the crack tip, the quarter-point isoparametric elements suggested by Barsoum [76] can be used. DEM is widely used because the nodal displacements are a primary output of the finite element program, and the SIF can be

easily computed without the need for further post-processing. Furthermore, the fine mesh does not have a significant effect on the computing time owing to the continuous upgrading of computer technology.

A.2 Interaction integral method

In linear elastic materials, the path-independent *J*-integral for a cracked body [88] is equal to the energy release rate. For general mixed-mode problems, the relationship between the *J*-integral and the SIF exists as follows:

$$J = \frac{K_I^2}{E'} + \frac{K_{II}^2}{E'} \tag{A.3}$$

where E' is the effective elastic modulus, which is equal to E and $E/(1-\nu^2)$ for plane stress and plane strain conditions, respectively. To avoid a potential source of inaccuracy in the numerical calculation, the contour integral is converted into an equivalent domain integral [89]. Therefore, the equivalent domain integral using the weight function q can be expressed as follows:

$$J = \int_A \left(\sigma_{ij} \frac{\partial u_i}{\partial x_1} - W\delta_{1j} \right) \frac{\partial q}{\partial x_j} \, \mathrm{d}A + \int_A \frac{\partial}{\partial x_j} \left(\sigma_{ij} \frac{\partial u_i}{\partial x_1} - W\delta_{1j} \right) q \, \mathrm{d}A \tag{A.4}$$

where $W = \int \sigma_{ij} \, \mathrm{d}\varepsilon_{ij}$ is the strain energy density and A is the area inside the contour. The domain, A, is considered from the elements surrounding the crack tip for numerical assessment of the integral.

To deal with the mixed-mode problem, Yau et al. (1980) [90] proposed the IIM. Two independent equilibrium states (actual$^{(1)}$ and auxiliary$^{(2)}$) of the cracked component are considered. The equivalent domain integral of the superimposed states is conveniently decomposed into the following:

$$J^{(1+2)} = J^{(1)} + J^{(2)} + I^{(1,2)} \tag{A.5}$$

where $I^{(1,2)}$ is the interaction integral between both states and is given by the following expression:

$$I^{(1,2)} = \int_A \left(\sigma_{ij}^{(1)} \frac{\partial u_i^{(2)}}{\partial x_1} + \sigma_{ij}^{(2)} \frac{\partial u_i^{(1)}}{\partial x_1} - W^{(1,2)} \delta_{1j} \right) \frac{\partial q}{\partial x_j} \, \mathrm{d}A \tag{A.6}$$

Using Equation (A.3) for the combined states and equating it with Equation (A.5) leads to the following relationship for $I^{(1,2)}$:

$$I^{(1,2)} = \frac{2}{E'} (K_I^{(1)} K_I^{(2)} + K_{II}^{(1)} K_{II}^{(2)}) \tag{A.7}$$

For the judicious choice of state 2 as the pure mode I asymptotic field with $K_I^{(2)} = 1 \;\; (K_{II}^{(2)} = 0),$ the mode I SIF for state 1 can be expressed in terms of the interaction integral as follows:

$$K_I^{(1)} = \frac{E'}{2} I^{(1,\text{ mode I})} \tag{A.8}$$

The mode II SIF can be determined in a similar manner. The main advantage of the integral method is that coarse meshes can provide accurate estimations of the SIF [79, 95].